7-24-2023

Disentangling Groundwater Dynamics at Oregon's McKenzie River Headwaters

Taylor Nicole Salazar
Portland State University

Disentangling Groundwater Dynamics at Oregon's McKenzie River Headwaters

by

Taylor Nicole Salazar

A thesis submitted in partial fulfillment of the
requirements for the degree of

Master of Science
in
Geography

Thesis Committee:
Andrés Holz, Chair
Kelly Gleason
Martin Lafrenz

Portland State University
2023

Abstract

Widespread mountain snowpack declines have been occurring across the western United States over the last century, and are increasing in duration and severity, with several record-breaking low-snowpack years in the last decade. In the Pacific Northwest, summer streamflow is largely a result of melting snow and groundwater discharge, as summers are typically dry and warm in this Mediterranean bioclimate, thus making spring-fed rivers critical for regional water resources. However, current trends and predictions in hydroclimate modeling indicate spring-fed rivers will experience reduced summer discharge driven by the increasingly larger impact of anthropogenic climate change (warming) on (decreased) mountain snowpack. A prominent spring-fed tributary of the Willamette River (25% of its late summer baseflow), the McKenzie River, serves as an important water source for Oregon's most densely populated and water-use intensive areas. Considering the recent record-breaking snow drought (i.e., 2015) and several low-snow years (2014, 2016, 2018, 2020, 2021) in the last decade, water managers have identified the need for estimates of groundwater transit time for this prominent spring-fed river.

Presented here is a novel approach using newly sampled and developed annual (total) and sub-annual (early- and late-wood) Douglas-fir (*Pseudotsuga menziesii)* tree-ring chronologies to disentangle multi-century groundwater dynamics, including statistical estimates of transit times (i.e., referred here as the time from when water enters an aquifer to when it exits at springs) at the headwaters of the McKenzie River at Clear Lake, Oregon. In addition, climate-growth relationships were assessed by pairing

six Douglas-fir tree-ring chronologies with hydroclimate data in order to examine the influence of a changing climate on forest ecosystems. Model results suggest a groundwater transit time of 5- to 15-years for the McKenzie River, Oregon. Moreover, the Douglas-fir stand's growth patterns are governed by summer temperatures, with negative correlations found with summer temperatures prior to and during the growing season, suggesting low soil moisture hinders growth. Summer radial (latewood) growth is also influenced by Clear Lake's levels throughout the year, with the highest correlations found from February to July, which coincide with warmer spring temperatures and accessibility to snowmelt water. The newly discovered groundwater transit times can aid in improving resource managers' understanding of groundwater dynamics at the headwaters of the McKenzie River and how spring-fed systems can sustain periods of low-flow under a warming climate.

Acknowledgements

Funding for this research was provided through a United States Geologic Survey (USGS) Oregon Water Science Center (ORWSC) and Portland State University Partnership seed grant. Access to conduct fieldwork at our study site was provided by the United States Forest Service (USFS).

The successful completion of this work was aided by the help of my dedicated field and lab assistants: Jeff Smith, Kraig Magnussen, Tessa Harden, Tiago Holz, and Paola Arroyo-Vargas. Thank you to my collaborators Daniel Taylor-Rodriguez, Dan Gavin, and Tessa Harden for their continued guidance throughout this entire process. Thank you to my thesis committee members, Kelly Gleason, and Martin Lafrenz, for setting time out of their busy schedules to provide feedback. Thank you to my cousin, Emma Magnussen, for applying her artistic talent to create a figure (Figure 1.3) that is both clear and visually appealing for my study. I would also like to express my gratitude to my advisor, Andres Holz, for his support and guidance throughout my thesis research. His expertise and insights were invaluable in shaping my ideas and approaches, and his constructive feedback helped me refine my work and strive for excellence. I am grateful for his patience, encouragement, and mentorship, which has been instrumental in shaping me as a researcher and scholar.

A final thank you to my family, friend Ruby Hurtado, and husband Anthony Salazar. I owe a great deal of gratitude towards to you all, as you have played a significant role throughout my academic journey. Mom and dad, none of this would be possible without your unwavering love and support; your selflessness will always be

remembered as key components that led up to achieving this milestone moment in my life. Lastly, Anthony, I am incredibly grateful for your continuous dedication towards our goals. Throughout this entire journey have been my rock and sounding board. Thank you for being my partner, best friend, and greatest supporter.

TAYLOR N. SALAZAR

Portland State University, April 2023

Table of Contents

List of Tables

List of Figures

Chapter 1 Introduction

The western United States mountain snowpack is significantly threatened by anthropogenic climate change (ACC; Mote et al., 2018; Catalano et al., 2019). An unequivocal consequence of anthropogenic forcing is a warmer climate, which will likely affect the timing, location, and amount of snowfall in the western United States (Livneh & Badger, 2020). Widespread reductions in mountain snowpack have been occurring over the last century in the western United States, but since the 1980's, natural variability in the climate systems has appeared to counterbalance snowpack reductions (Mote, 2006). However, climate model simulations indicate accelerated snowpack reductions will occur over the twenty-first century as anthropogenically driven warming amplifies, having severe impacts on hydrological processes and substantial socio-economic and ecological consequences (Siler et al., 2019; Coulthard et al., 2021). Increased snow droughts and declining snowpack will likely lead to increased reliance on groundwater, but these phenomena are also projected to decrease summer baseflows in the Pacific Northwest (PNW; Mote et al., 2018; Segura et al., 2019).

In the western Oregon's Cascades, runoff-dominated river systems have highly variable discharge rates throughout the year, making the reliability of streamflow baseflows of spring-fed river systems a key source of water for hydrological ecosystems as well as for drinking water for most of western Oregon, especially in the summer months when precipitation is considered scarce (Jefferson et al., 2006; Segura

et al., 2019). A prominent spring-fed river in this region, the McKenzie River, has a high unit baseflow discharge, which highlights the importance of better understanding the groundwater dynamics at its headwaters at Clear Lake, Oregon. Clear lake is located in the Higher Cascade Mountains, which are younger and more permeable formations than its older counterpart further west (see Section 1.3), allowing for a large and deeper groundwater storage (Jefferson et al., 2006; Tague et al., 2006). From a water supply standpoint, there is broad concern about the response that this deeper groundwater storage will have to a warming climate, as rivers that are primarily sustained by groundwater are more vulnerable to fluctuations in snowmelt levels and their timing than those that are predominantly fueled by runoff, owing to their slower recession rates (Jefferson et al., 2006; Tague et al., 2008). But a first step towards disentangling this larger question is to estimate the transit time, or the time it takes from when water enters an aquifer to when it exits at springs at Clear Lake. Previous transit time estimates range substantially; between 13 to 26 years (Jefferson et al., 2006) and 30 to 31 years (Deligne, *unpublished*). This disagreement in transit time hampers the development of a more comprehensive understanding of the effects of a reduced snowpack on ecosystem processes and water usage downstream.

Clear Lake receives approximately 10% of its water from the Great Spring at the northeastern margin of the lake, with the bulk of the remaining water coming from springs along the lake bottom, and in August, groundwater is the only source of water coming out of Clear Lake (Fig. 1.1; Stearns, 1929; Jefferson et al., 2006). In 2009, Deligne (*unpublished*) pioneered a research design comparing tree-ring radial growth of trees growing on a small peninsula in Clear Lake (i.e., by its outlet) with trees

situated on the graben wall above and west of Clear Lake (control group; Figure 1.2). Deligne's study design adopted the reasonable premise that both sets of trees (outlet and control) grew under similar climatic conditions, but trees at the lake outlet had additional access to groundwater during the rain-free portion of the growing season (mid/late spring through late summer/early fall; Jefferson et al., 2006; Deligne, *unpublished*). Thus, by comparing radial growth in trees at the outlet to that of the adjacent more water-limited trees, groundwater-dependent differences could be quantified from their respective tree-ring growth patterns. More specific, growth patterns found in isolated trees growing at the control site (away from streams, lakes, and other trees that compete for resources), should only respond to the current year's climatic conditions. However, growth patterns from isolated trees at the lake outlet should reflect a response to both the current year's climatic conditions and variation in lake water levels. In turn, lake water levels vary from surface runoff resulting from snowmelt during the current year's climate and groundwater discharge. While surface runoff in these young lava fields in the High Cascades is close to zero (Tague et al. 2008), groundwater discharge is a function of the hydroclimatic conditions (both snowfall and snowmelt timing and amounts) that occurred during an unknown past period (i.e., transit time). Hence, the radial growth of the trees at the outlet in a given year should be autocorrelated with the growth of trees at the control site during the past (ca. 30-31 years; Deligne, *unpublished*). Although pioneering in its research design and use of paired analysis of tree-ring radial-growth patterns to reconstruct groundwater transit time, Deligne's (*unpublished*) study included only 15 paired increment tree cores, a short-time span of dendrochronological analysis (1805–2008), conducted sub-

optimal processing of the tree-ring samples (cross-dating), and did not evaluate the possible impact of tree ages or differences in geology (i.e., her control site was located in the Western Cascades).

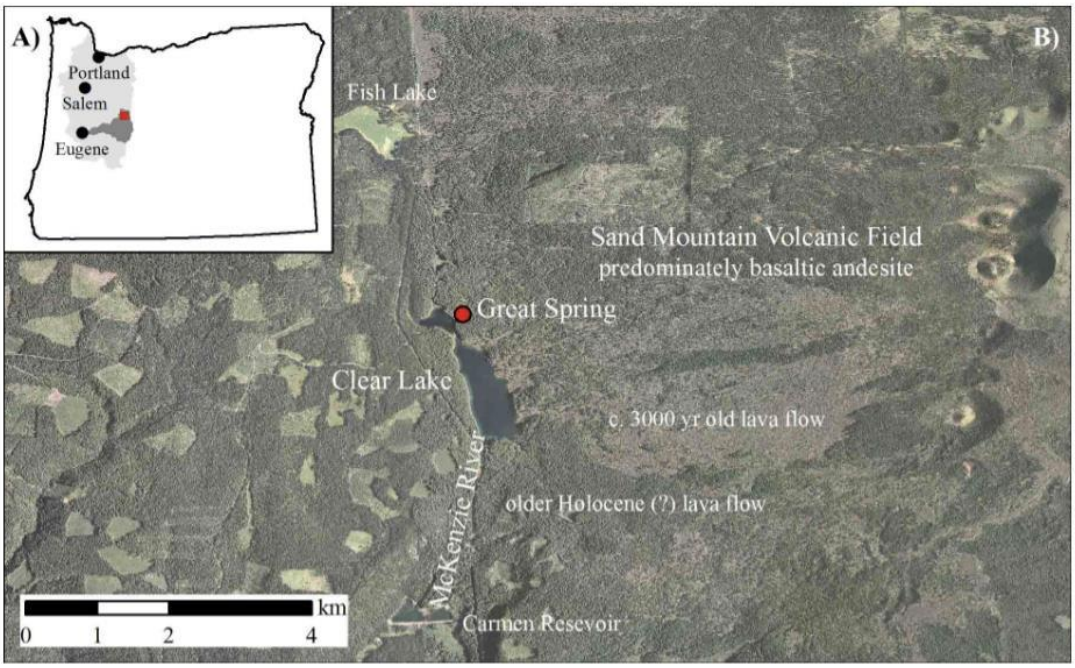

Figure 1.1 Clear Lake overview study area extracted from the Deligne (*unpublished*) study. (A) Map displaying the Willamette River Basin in light grey and the McKenzie River Basin in dark grey and (B) Clear Lake with the Great Spring (marked with a red dot) and adjacent young lava fields in the High Cascade Mountains.

Lastly, Deligne's pilot study also did not include the 2010 to 2020 decade, a period with several recorded dry/low-snowpack years, such as 2014 to 2016, 2018, and 2020, nor did she explore differences in the groundwater transit time using early- (spring) vs. late- (summer) wood, which are known to experience different climatic sensitivities (e.g., Meko and Baisan, 2001; Torbenson et al., 2006; Stahle et al., 2009; Dannenberg and Wise, 2016). Furthermore, Deligne's (*unpublished*) analysis did not evaluate the climatic parameters that in turn might affect and explain the patterns in

radial growth, which is essential for understanding and confirming the relationship between radial growth and hydroclimatic conditions at both study sites. To meaningfully assess groundwater dynamics of the McKenzie River, this thesis research will expand and modify Deligne's (*unpublished*) novel approach to develop a dendrohydrological reconstruction of groundwater transit time and quantification of climate-radial growth relationships that will inform water resource managers' understanding of long-term trends in streamflow for an iconic river that possesses such significant socio-economic relevance.

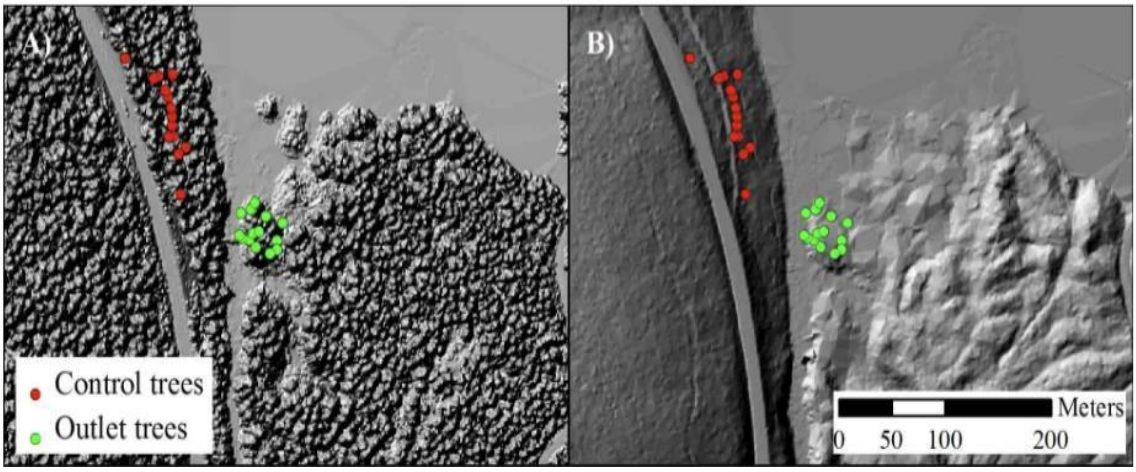

Figure 1.2 Clear Lake study site LiDAR-derived DEM extracted from the Deligne (unpublished) study. (A) The highest hit LiDAR map displays the old-growth forest surrounding the Clear Lake outlet area. (B) The bare Earth LiDAR map shows the N-S fault that divides the older Miocene Western Cascades to the west (left) and the younger Holocene lava flow to the east (right). Deligne's sampling points at the outlet site (in green) and their control site (in red) on older Western Cascade geology.

1.2 Study Area

The greater Willamette watershed is one of Oregon's largest river systems, draining 28,672 km^2 annually into the Columbia River (Sproles et al., 2017). The McKenzie River

basin is approximately 3,463 km^2 and is a main tributary of the Willamette watershed (Sproles et al., 2017). The groundwater-dominated McKenzie River drains from the Cascade crest and runs west until it meets the run-off-dominated Willamette River in its northward flow (Sproles et al., 2017). Although the McKenzie River covers less than 12% of the Willamette basin, it accounts for 25% of the Willamette River's late summer baseflow and 12% of its total drainage (PNWERC, 2002; Tague et al., 2013). This makes the McKenzie River a key water source for municipal, agriculture, power generation, aquatic ecosystems, and recreation use (Tague et al., 2013).

The western Cascades' temperate Mediterranean hydroclimate is characterized by cool, wet winters and moderate, dry summers with average annual temperatures ranging from -1˚ C to 11˚ C (Clackamas SWCD, 2013). Exceptionally high winter precipitation occurs throughout the Cascades due to orographic lifting of Pacific Ocean air masses that leads to annual precipitation ranging from 1150 mm to 3600 mm, partitioning between rain and snow by elevation (Clackamas SWCD, 2013; Fayad et al., 2017). The Cascades' maritime snow cover is characterized by relatively deep, wet, and warm snowpack, with higher elevations being snow-dominated and mid-to-low elevations receiving mixed precipitation regimes (i.e., rain < ca. 400 m and snow > ca. 1200 m above sea level [asl]; Sturm et al., 1995; Tague et al. 2008; Clackamas SWCD, 2013; Fayad et al., 2017).

1.3 Geology of the McKenzie River Basin

The McKenzie basin has two distinct and adjacent geologic provinces: the predominantly Miocene Western Cascades to the west and the Plio-Pleistocene High Cascades to the east (Figure 1.2; Tague et al., 2013). The Western Cascades are dominated by old volcaniclastic rocks, and the High Cascades are dominated by young

basaltic lava outflows (Tague et al., 2013). Hydrologic flow path differences and transit times, when accounting for aquifer size, are driven by these distinctions (Jefferson et al., 2006), with relatively minor differences due to climate or land use (Tague et al., 2008). The High Cascades' young lava flows are extremely permeable with high vertical hydraulic conductivity which generate the bulk of deep groundwater flow and spring discharges (Jefferson et al., 2006). The high vertical conductivity allows for recharge to rapidly drain through the undeveloped shallow soils and into large deep aquifers, where Jefferson et al. (2006) reported that transit times can be on the timescale of years or decades. In contrast, the Western Cascade drainage system is made up of steep lateral hydraulic gradients, shallow bedrock, and clay aquitards that keep recharge constrained to the subsurface (Tague et al., 2013).

The flow paths created by the differences in geology produce distinct hydrologic regimes in High Cascade watersheds that are characterized by high baseflows, slow recessions, and muted flood peaks (Tague & Grant, 2004). Snowmelt peaks during the winter and spring generate recharge that quickly enters streams in the Western Cascades, creating a greater contribution to flow than the High Cascades. This process reverses in the summer months when precipitation is scarce and the Western Cascades groundwater system is primarily depleted, and flow in the McKenzie River largely originates from the High Cascade aquifers which range from 40 m to 100 m deep (Manga, 1996) Tague and Grant, 2004; Jefferson et al., 2006). This study is focused on the groundwater-originated headwaters of the McKenzie River at Clear Lake (Figure 1.1), located on the western edge of a graben with Holocene lava flows to the north,

east, and south and the Western Cascades to the west (Figure 1.2; Jefferson et al., 2006).

1.4 Climate Change and the McKenzie River Basin

Mountain hydrology is projected to be highly vulnerable to warmer air temperatures as a result of anthropogenic forcing due to the lack of infrastructure to store rainwater (Barnett, 2005). Although scientists face limitations with observational snow records (e.g., Coulthard et al., 2021), there has still been extensive research documenting significant declines in western United States mountain snowpacks as well as a series of estimates of future changes to snowpack dynamics. Several studies have shown a decrease in both 1 April Snow Water Equivalent (SWE) and peak SWE, giving evidence to snowpack declines (Nolin & Daly, 2006; Abatzoglou, 2011; Fyfe et al., 2017; Harley et al., 2020; Marshall et al., 2019; Mote, 2006; Mote et al., 2005, 2018; Pederson et al., 2011). Additionally, Mote et al. (2018) found that 21% of the western United States mountain snowpacks have declined since 1915, equivalent to 36 km^3 or in other words, more than the amount of water stored in Lake Mead, the western United States largest reservoir. In addition to the studies cited above, other research also found that ACC has resulted in an earlier peak SWE and timing of spring snowmelt, which has shifted the timing of snowmelt-derived streamflow to earlier in the water year in the western United States (Fritze et al., 2011; Gergel et al., 2017; Knowles et al., 2006.; Mote et al., 2018; Stewart et al., 2005).

Maritime snowpacks at low elevations in the PNW, where the bulk of precipitation occurs at 0˚C, are most susceptible to warmer air temperatures that are

expected to reduce the amount of precipitation that falls as snow and stimulate earlier snowmelt, as warmer snowpacks are riper and require little additional energy input to melt (Nolin & Daly, 2006; Linveh & Badger, 2020). Changes in snow dynamics from anthropogenically-driven warming can lead to timing shifts in seasonal hydrographs, generating increased winter flow and reduced spring and summer flow (Barnett, 2005). Mountain region climate models for the PNW estimate future temperature increases ranging from 2.0˚C to 4.0˚C west of the Cascades, with temperature extremes occurring more rapidly over the second half of the twentieth century (Mass et al., 2022). These projections have been linked to reductions in summer water availability (Tague et al., 2008). However, according to a recent analysis, a reestablished dedication to attaining the Paris Agreement's long-term goal of restricting warming below 2.0˚C and striving to limit it to 1.5˚C above pre-Industrial levels is achievable by fully and promptly fulfilling all objectives (Heeter et al., 2023). Although this requires significant effort from countries and individuals, this finding suggests that if all objectives are met in full, it could help mitigate the effects of ACC, including the projected water availability declines in the summer months west of Oregon's Cascades.

Due to its low elevation, in comparison to the Rocky Mountains for instance, the High Cascades, and thus the Willamette River basin has been identified as climatologically "at-risk", as a majority of snow in the basin accumulates at close to 0˚C, meaning even slightly warmer temperatures can shift snow to rain (Nolin & Daly, 2006). Similarly, the McKenzie River basin, in particular, makes up a large portion of the Willamette River's "at-risk" snow zone (Nolin & Daly, 2006). The McKenzie River basin generates significant flow for the Willamette River basin.

Thus, better contextualizing groundwater dynamics at the McKenzie River's headwaters is crucial at a regional scale to help establish climate change adaptation strategies that can be applied in conjunction with global efforts to reduce emissions.

The objectives of this research were to develop and quantify variations in radial growth of annual and sub-annual tree-ring chronologies to: (1) quantify the transit time of the groundwater supplying the McKenzie River's headwaters at Clear Lake, from a newly created dendrohydrological groundwater reconstruction; (2) examine climate-growth relationships and compare the geo-hydroecological mechanisms that drive differences in tree-growth responses between our two sites; and (3) assess the impacts on water resources and ecosystems downstream.

1.5 Hypotheses

The tree-growth at two sites, namely the waterfront and the control site, are hypothesized to be controlled by similar climatic factors due to the close proximity of the two sites, but given differences in distance to water access from Clear Lake, it is hypothesized that the following factors influence radial growth of trees growing at the waterfront site: (1) local climate conditions, that should also be present at the control site; (2) residual (climate) effects of temporal autocorrelation from previous growth at the waterfront site; and (3) residual effects from the transit time between snowmelt and groundwater outflow into Clear Lake. For the control site, the hypothesized factors affecting growth are: (1) local climate conditions that should also be present at the waterfront site; and (2) residual (climate) effects of temporal autocorrelation from

previous growth at the control site. These predictors will be examined in further detail to determine their impact on tree-growth at both sites (Figure 1.3).

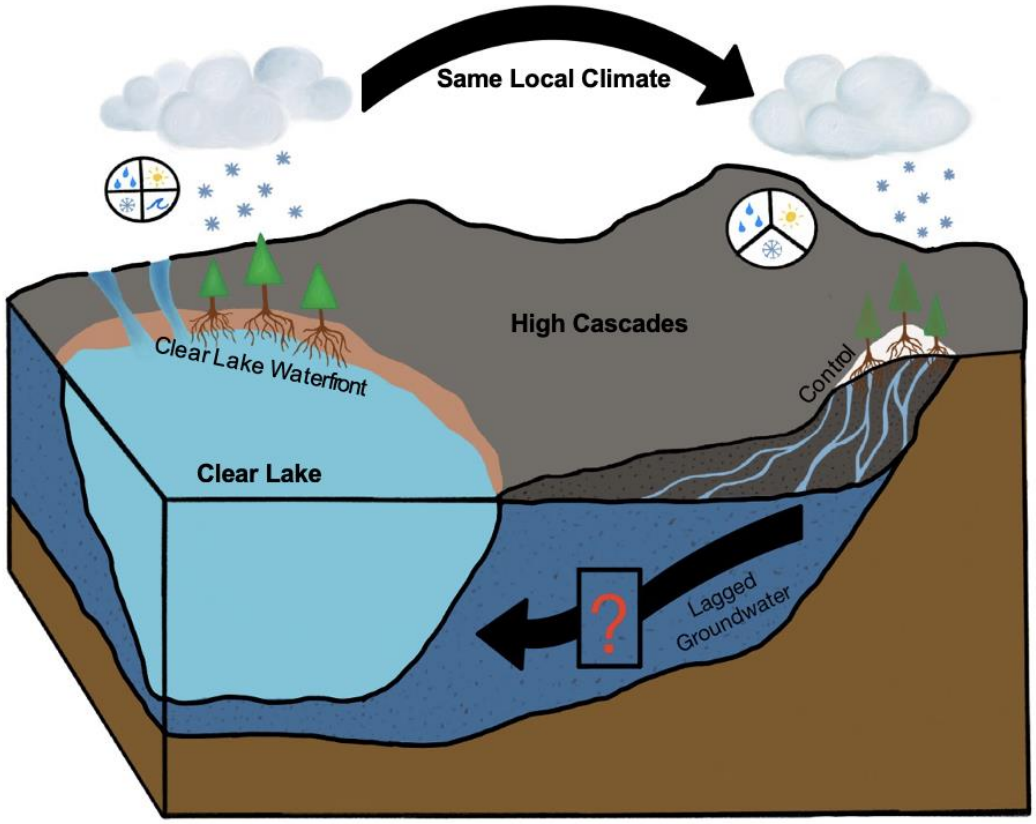

Figure 1.3. Conceptual model of factors influencing radial growth of the trees growing at my two study sites, waterfront and control, hypothesizing that growth at both sites is influenced by: (1) shared local climate that affects the current season growth, which includes temperature, precipitation, and snow; (2) residual or memory effects of temporal autocorrelation, which can influence growth of the current season due to factors such as lagged climate effects, climate variability (from inter-annual to inter-decadal scale), and other time-dependent processes. Moreover, it is hypothesized that (3) growth of trees at the waterfront site is further influenced by residual effects from groundwater outflow into Clear Lake, as indicated by the black arrow, to which only the roots of waterfront trees have direct access.

Chapter 2 Methods

2.1 Tree-ring Data and Chronology Formation

Douglas-fir (*Pseudotsuga menziesii*) tree-ring samples were collected in the summer of 2021 from two new sites at Clear Lake (ca. 900 m asl; Figure 2.1). Site selection was based on sample site characteristics (i.e., direct root access to the lake for the waterfront chronology and lack thereof for the control chronology) and the availability of climatically sensitive tree-growth (i.e., interannual radial growth patterns observed in the field from cores obtained from isolated individuals with low to no influence from neighboring trees; i.e., competition). Additionally, and in contrast to Deligne (2009)'s design, sampling was only conducted on trees growing on the young High Cascades.

Figure 2.1 Map of this thesis' study sites showing the waterfront site (groundwater-climate-dependent tree-growth) located around the lake perimeter, and the control site (climate-dependent tree-growth) east of and removed from Clear Lake. The Great Spring is also denoted in the northeastern margin of the lake (light blue dot), as well as the USGS Clear Lake Outlet Gauge (orange dot) that was used to obtain streamflow data this study.

While trees at both sites were growing on dry, rocky lava bed outcrops and were influenced by the same local climate, trees growing at the climate- and groundwater-dependent sample site, located along the perimeter of the lake (waterfront hereafter),

had direct root access to the water throughout the year (i.e., including in late spring and summer when moisture-water stress is highest for trees). Instead, the control sample site, located approximately 500 m east of Clear Lake, had no direct access to the lake (i.e., no access to groundwater; Figure 1.3; Tague et al., 2008; Jefferson et al., 2006). At the control site (climate-dependent site), sampled trees were located on mostly west-facing slopes, at ca. 950 m asl, with the average recharge elevation (at Sand Mountain) at ca. 1,372 m asl (Jefferson et al., 2006).

In addition, targeted Douglas-fir trees were selected by age (i.e., characteristics such as large diameter, branch-free lower trunk, gnarly crown with flattened top, thick bark with deep grooves), as well as minimal presence of outward disturbance (i.e., burn scars, and visible damage from wind and /or insect and pathogens). The sampling procedure used followed standard dendroclimatological methods: thirty trees were sampled at each site, with two cores extracted from each tree at standard breast height (1.37 m) using a Haglof 5.15-mm three-threaded 24-inch increment borer (Table 2.1; Speer, 2010). Individuals were also selected based on the presence of high-sensitivity growth, e.g., ring boundaries in the first core were examined for interannual variation prior to committing to a second core, and if growth complacency (lack of inter-annual growth variation) was identified, we moved to the next tree. Samples were taken at approximately 180˚ from each other to increase the chance of sampling locally absent rings, and parallel to slopes to decrease the occurrence of compression or tension wood (Fritts, 1976; Stokes and Smiley, 1968; Cook and Kairiukstis, 1990). Samples were stored in plastic straws and transported back to the Global Environmental Change (GEC) Laboratory at Portland State University for processing.

Table 2.1 Full description and location of individual trees sampled at each site at Clear Lake, Oregon.

Sample Name	Site	Site Descriptor	Lat/Long	Length (yr)
CLW_01_PSME	Waterfront	Climate-groundwater-dependent	44°21'53" N, 121°59'25" W	1656-2021
CLW_02_PSME	Waterfront	Climate-groundwater-dependent	44°21'42"N, 121°59'32"W	1752-2021
CLW_03_PSME	Waterfront	Climate-groundwater-dependent	44°21'40" N, 121°59'23"W	1668-2021
CLW_04_PSME	Waterfront	Climate-groundwater-dependent	44°21'42" N, 121°59'25' W	1705-2021
CLW_05_PSME	Waterfront	Climate-groundwater-dependent	44°21'47" N, 121°59'22" W	1644-2021
CLW_06_PSME	Waterfront	Climate-groundwater-dependent	44°21'53" N, 121°59'24" W	1802-2021
CLW_07_PSME	Waterfront	Climate-groundwater-dependent	44°22'10" N, 121°59'30" W	1623-2021
CLW_08_PSME	Waterfront	Climate-groundwater-dependent	44°22'14" N, 121°59'34" W	1813-2021
CLW_09_PSME	Waterfront	Climate-groundwater-dependent	44°22'2" N, 121°59'26" W	1857-2021
CLW_10_PSME	Waterfront	Climate-groundwater-dependent	44°22'10 N, 121°59'29" W	1573-2021
CLW_11_PSME	Waterfront	Climate-groundwater-dependent	44°22'19 N, 121°59'36" W	1583-2021
CLW_12_PSME	Waterfront	Climate-groundwater-dependent	44°22'19 N, 121°59'36 W	1570-2021
CLW_13_PSME	Waterfront	Climate-groundwater-dependent	44°22'22" N, 121°59'37 W	1758-2021
CLW_14_PSME	Waterfront	Climate-groundwater-dependent	44°22'23" N, 121°59'38" W	1804-2021
CLW_15_PSME	Waterfront	Climate-groundwater-dependent	44°22'29" N, 121°59'50" W	1586-2021
CLW_16_PSME	Waterfront	Climate-groundwater-dependent	44°22'9" N, 121°59'30" W	1643-2021

Sample Name	Site	Site Descriptor	Lat/Long	Length (yr)
CLW_17_PSME	Waterfront	Climate-groundwater-dependent	44°22'9" N, 121°59'29" W	1796-2021
CLW_18_PSME	Waterfront	Climate-groundwater-dependent	44°22'12" N, 121°59'29" W	1810-2021
CLW_19_PSME	Waterfront	Climate-groundwater-dependent	44°22'14" N, 121°59'34" W	1664-2021
CLW_20_PSME	Waterfront	Climate-groundwater-dependent	44°22'16" N, 121°59'35" W	1626-2021
CLW_21_PSME	Waterfront	Climate-groundwater-dependent	44°22'18" N, 121°59'37" W	1676-2021
CLW_22_PSME	Waterfront	Climate-groundwater-dependent	44°22'18" N, 121°59'36" W	1637-2021
CLW_23_PSME	Waterfront	Climate-groundwater-dependent	44°22'22" N, 121°59'37" W	1826-2021
CLW_24_PSME	Waterfront	Climate-groundwater-dependent	44°22'29" N, 121°59'49” W	1428-2021
CLW_25_PSME	Waterfront	Climate-groundwater-dependent	44°22'34" N, 121°59'49" W	1416-2021
CLW_26_PSME	Waterfront	Climate-groundwater-dependent	44°22'29" N, 121°59'49" W	1407-2021
CLW_27_PSME	Waterfront	Climate-groundwater-dependent	44°22'36" N, 121°59'49" W	1576-2021
CLW_28_PSME	Waterfront	Climate-groundwater-dependent	44°22'36"N, 121°59'49"W	1673-2021
CLW_29_PSME	Waterfront	Climate-groundwater-dependent	44°22'38" N, 121°59'50" W	1447-2021
CLW_30_PSME	Waterfront	Climate-groundwater-dependent	44°22'31" N, 121°59'51" W	1566-2021
CLL_01_PSME	Control	Climate-dependent	44°12'12" N, 121°59'29" W	1729-2021
CLL_02_PSME	Control	Climate-dependent	44°12'8" N, 121°59'12" W	1679-2021
CLL_03_PSME	Control	Climate-dependent	44°12'1” N, 121°59'6" W	1730-2021

Sample Name	Site	Site Descriptor	Lat/Long	Length (yr)
CLL_04_PSME	Control	Climate-dependent	44°12'2" N, 121°59'5" W	1724-2021
CLL_05_PSME	Control	Climate-dependent	44°12'57" N, 121°35'27" W	1625-2021
CLL_06_PSME	Control	Climate-dependent	44°21'59" N, 121°59'0" W	1695-2021
CLL_07_PSME	Control	Climate-dependent	44°21'55" N, 121°59'0" W	1616-2021
CLL_08_PSME	Control	Climate-dependent	44°21'55" N, 121°58'6" W	1666-2021
CLL_09_PSME	Control	Climate-dependent	44°21'56" N, 121°58'58" W	1677-2021
CLL_10_PSME	Control	Climate-dependent	44°21'55" N, 121°58'58" W	1518-2021
CLL_11_PSME	Control	Climate-dependent	44°21'59" N, 121°59'11" W	1720-2021
CLL_12_PSME	Control	Climate-dependent	44°21'59" N, 121°59'11 W	1637-2021
CLL_13_PSME	Control	Climate-dependent	44°21'57" N, 121°59'09" W	1694-2021
CLL_14_PSME	Control	Climate-dependent	44°21'57" N, 121°59'06" W	1419-2021
CLL_15_PSME	Control	Climate-dependent	44°21'57" N, 121°59'05" W	1543-2021
CLL_16_PSME	Control	Climate-dependent	44°21'57" N, 121°59'04" W	1462-2021
CLL_17_PSME	Control	Climate-dependent	44°21'57" N, 121°59'03" W	1424-2021
CLL_18_PSME	Control	Climate-dependent	44°21'55" N, 121°59'04" W	1485-2021
CLL_19_PSME	Control	Climate-dependent	44°21'54" N, 121°59'02" W	1687-2021
CLL_20_PSME	Control	Climate-dependent	44°21'53" N, 121°59'08" W	1333-2021
CLL_21_PSME	Control	Climate-dependent	44°21'60" N, 121°59'13" W	1662-2021
CLL_22_PSME	Control	Climate-dependent	44°22'1" N, 121°59'10" W	1796-2021
CLL_23_PSME	Control	Climate-dependent	44°22'3" N, 121°59'4" W	1562-2021

Sample Name	Site	Site Descriptor	Lat/Long	Length (yr)
CLL_24_PSME	Control	Climate-dependent	44°22'3" N, 121°59'4" W	1750-2021
CLL_25_PSME	Control	Climate-dependent	44°22'3" N, 121°59'2" W	1698-2021
CLL_26_PSME	Control	Climate-dependent	44°22'1" N, 121°59'2" W	1500-2021
CLL_27_PSME	Control	Climate-dependent	44°22'0" N, 121°59'0" W	1714-2021
CLL_28_PSME	Control	Climate-dependent	44°21'60" N, 121°59'0" W	1624-2021
CLL_29_PSME	Control	Climate-dependent	44°21'59" N, 121°59'1" W	1702-2021
CLL_30_PSME	Control	Climate-dependent	44°21'59" N, 121°58'60" W	1700-2021

**Clear Lake Waterfront (CLW), Clear Lake Lava (CLL)*

Following standard processing procedures (Stokes and Smiley, 1968), tree-ring cores were mounted to slotted wooden mounting boards and sanded using increasingly finer grits of sandpaper, starting at 60 p, and increasing to 1000 p until prominent ring boundaries and unicellular anatomy were visible under a microscope (Speer, 2010). Each sample was scanned in 1700 to 2400 dpi with an Epson Expression 11000XL scanner. Using a combination of cellular anatomy and marker years as a guide, samples were delineated, measured, and assigned annual calendar years using CooRecorder software, which automatically pre-defines ring-width boundaries and measurements to the precision of the nearest 0.001 mm (Cybis Elektronik, 2010; Larsson, 2014). Samples were visually (Yamaguchi, 1991) and statistically cross-dated (using combined approaches found in CDendro [Cybis Elektronik, 2010], COFECHA [Version 6.02; Holmes, 1983], and the dplR package in R [Bunn, 2008]).

Standard dendroclimatological methods were used to measure and develop total-ring width, early-, and late-wood chronologies for each sample site, representing the mean tree-growth (i.e., Cook, 1985). Chronologies were developed using the Dendrochronology Program Library R package, dplR (Bunn, 2008). Raw measurements were detrended to statistically remove long-term age- and size-related, biological growth trends while enhancing climate-related trends in the tree-ring measurements (Fritts, 1976; Speer, 2010). The measurements were sensitivity-tested with varying detrending methods (i.e., smoothing spline vs. statistical model). A negative exponential curve was selected as the primary detrending method, followed by an alternative of a fitted linear model or a straight line through the mean in circumstances of a linear model with a negative slope (Fritts, 1976; Cook, 1985; Cook and Kairukstis, 1990; Stokes, 1996; Bunn, 2008).

Next, detrended series were pre-whitened using Autoregressive Moving Average (ARMA) modeling to further decouple the persistent biological noise from climate signals in the tree-ring measurements (Holmes, 1983; Cook and Briffa, 1990; Cook and Peters, 1997). Autocorrelation occurs when a single year of growth influences multiple following years of growth (LaMarche, 1974; Speer, 2010). For example, a backward lagged tree-ring from 2021 (t-1) for trees growing near the lakefront, can inform lake levels in 2020 (t) based on autocorrelation in the tree metabolism and biology (i.e., storage of sugar, starches, and other non-structural carbon and chemical compounds), such that lake level conditions in 2020 can pre-condition and influence growth in the following year (Cook and Kairiukstis, 1990).

After detrending, the tree-ring measurement series were statistically standardized and aggregated into dimensionless growth indices to enhance the signal of interest (i.e., hydroclimate) while reducing noise (i.e., disturbance, stand-dynamics; Cook and Briffa, 1990; Speer, 2010). For both sites, the biweight robust mean of both cores per ring was used to compute average annual growth measurements (early-, late-wood, and total ring width), leading to the development of the final standard (contains autocorrelation) and residual or pre-whitened (autocorrelation removed) Douglas-fir (*Pseudotsuga menziesii*) chronology (Stokes and Smiley, 1996). Since this study capitalizes on autocorrelation, the residual chronology was excluded from further analysis.

A final step was conducted to determine the adequacy of the sample size at capturing the population growth signal. For this, I used the Sub-Sample Strength (SSS) using a threshold of 0.85 to ensure the most robust timespan of the chronology was used for the analysis (Cook and Kairiukstis, 1990; Buras, 2017). Total ring width-, early-, and late-wood- chronologies were truncated where the SSS dropped below the standard value of 0.85 (Figures A.1., A.2.). The SSS is a measure of decreasing predictive power due to reductions in sample size of tree-ring series back in time (Buras, 2017). Chronology quality was also verified using standard tree-ring series statistics, such as mean sensitivity, R-BAR, and series intercorrelation (Wigley et al., 1984; Cook et al., 1990; Speer, 2010). Finally, a cross-correlation function analysis was performed with lags at an annual scale and a correlation significance at $p < 0.05$ to verify that the chronologies could serve as predictors of groundwater transit time.

2.2 Hydrologic and Climate Data

All Snow Telemetry (SNOTEL) and snow course datasets north of 44˚9', south of 44˚27', west of 121˚42', and east of 122˚3' and located between 900 m to 1500 m asl in elevation were extracted from the United States Department of Agriculture (USDA), Natural Resource Conservation Service's National Water and Climate Center (NRCS, 2021). The criteria for elevation were determined to accurately depict snowfall at the two sites. Selection criteria for the data records in this study was as follows, the dataset: (1) could not have had more than one missing data-entry in a 30-year period, (2) could not contain missing consecutive entries, and (3) was required to be at least 60 years in length. Various climate datasets were run through a suite of statistical analyses to determine dataset quality as part of the selection criteria. Based on this criteria, local snow course (manual snow measurements) and SNOTEL (system of automated snow and climate sensors) station records were omitted as they did not meet the criteria of a record at least 60 years in length or had several missing consecutive entries. Instead, gridded high-spatial-resolution monthly mean air temperature, monthly total precipitation, and monthly total SWE datasets were used for this research as it provided an extensive and continuous record without missing values.

Monthly mean air temperature and monthly total precipitation records were extracted using Parameter-elevation Regressions on Independent Slopes Model (PRISM) Explorer for a 4 km^2 grid at 44˚ 22' 08" N and 121˚59' 40" W for the overlapping period with the developed tree-ring chronologies of 1895 to 2021 (PRISM Climate Group, 2014). Climate Engine Research Application was also used

to download TerraClimate monthly total SWE datasets for a 4 km^2 grid based on Clear Lake's coordinates for the overlapping period of 1959 to 2021 (Abatzoglou et al., 2018). Lastly, non-gridded gauged streamflow time series of monthly mean flow at the outlet at Clear Lake, which extends for the 1959-2021 period was accessed from the United States Geological Survey (USGS) database (https://waterdata.usgs.gov/or/nwis/uv).

To verify the selected gridded high-spatial climate data represented robust records for this region, separate spearman correlations were individually performed between the SNOTEL stations with the longest and most complete record (Santiam Junction (1978-2021), McKenzie (1979-2021), and Hogg Pass (1978-2020) SNOTEL stations) with PRISM (mean monthly air temperature and total monthly precipitation; 1895-2021) and TerraClimate (total SWE; 1959-2021) gridded datasets. Records were excluded from further analysis if correlations with other stations were not significant ($p < 0.05$) and if the spearman's rho value was less than 0.40.

2.3 Climate-Growth Relationships

To determine the effect of climate on radial growth responses for the standard chronologies, correlations and partial correlation functions were conducted with monthly mean air temperature, monthly total precipitation, and monthly mean streamflow. Radial growth responses to SWE were indirectly explored using monthly mean air temperature and monthly total precipitation. Meko et al. (2011) seasonal correlation (SEASCORR) procedure in R package TreeClim (Zang, 2015) was utilized for this step. This package allows for quantifying r values between tree-

growth and a 14-month window of integrated 1-, 2-, and 6- month, monthly and seasonal hydro-climate data, starting in August of the previous growing season through the end of the concurrent growing season (September). In addition, the temporal stability (stationarity) of the climate-growth relationship throughout time was also tested over subperiods (Figures A.19., A.20.). Significance was estimated using exact bootstrapping (Percival & Constantine, 2006). This analysis was then replicated on earlywood and latewood standard chronologies.

2.4 Development and analysis of the reconstruction model

Following Deligne (*unpublished*)'s analytical approach, several lagged multiple linear regression models were developed to identify the groundwater transit time in R. As the earlywood, latewood, and total-ring width chronologies for each site were significantly correlated with the hydroclimate parameters (air temperature, precipitation, SWE, and streamflow), and provide different information, these three tree-ring chronologies at each site (6 total) were used independently as model predictors for assessing groundwater transit time at Clear Lake. For example, earlywood develops from spring to summer, aligning with the timing of peak SWE and then peak annual discharge at Clear Lake, Oregon (Jefferson et al., 2008). After selecting hypothesized predictors of the response variable (groundwater transit time), the reconstructions were built.

To determine the presence of autocorrelation in the tree-ring chronologies at each site, Partial Autocorrelation Functions (PACF) in R were used, where significant lags (i.e., *t, t-1, t-2,* etc.) were identified based on the 95% confidence level. The PACF is a

function that displays the occurrence of partial correlation between a series and a lagged version of itself, or the remaining correlation at each lag that is not accounted for by previous lags (i.e., not cumulative lags). Partial autocorrelation was considered present in scenarios where it exhibits a significant correlation of at least 5% between year *t* and successive lags (Figure 3.4). The use of lagged predictors allowed for information from the tree-growth and hydro-climate relationship in the previous years to inform the groundwater transit time (Cook and Kairiukstis, 1990). Based on these PACF results, I included three predictors for the waterfront growth response (Table 2.2). The third predictor is hypothesized to represent the lagged response of trees at the control site to hydroclimate conditions, including snowpack, snowmelt, and groundwater discharge into the lake.

Table 2.2 Predictor variables used in the set of multiple lagged regression analyses to predict tree-growth in year *t* at the waterfront site.

1) tree-growth at the control site for year *t*,
2) tree-growth at the waterfront site for years with significant partial autocorrelation with the same waterfront trees in year *t* (i.e., *t-1*, *t*-2, *t-3, …*),
3) tree-growth at the control site for years without significant partial autocorrelation with the same control trees in year *t* (i.e., *t-4* through *t-40*, taken one at a time and performed separately).

A second set of multiple lagged regression models were performed, but this time exclusively on the control group. This analysis was implemented to validate that the results in the first set of multiple lagged regression models were displaying actual differences between the trees at the control and waterfront sites (Table 2.3) and to verify that the significant results from the first set of regressions are not due to

climatic patterns that are also present in the control cohort since we hypothesize both sites experience the same local climate (i.e., a cyclic response patterns due to El Niño-Southern Oscillation [ENSO] or Pacific Decadal Oscillation [PDO]). In a significant model, any resulting lag that passes the model selection criteria (see below) for the set of regressions at the waterfront site (lagged models predicting tree-growth at the waterfront site) will give evidence to a groundwater transit signal.

Table 2.3 Predictor variables used in the set of multiple lagged regression analyses to predict tree growth in year t at the control site.

1) tree-growth at the control site for years with significant partial autocorrelation with the same control trees in year *t* (i.e., *t-1*, *t*-2, *t-3,* …),
2) tree-growth at the control for years *t-4* through *t-40*, taken one at a time and performed individually.

After fitting the full models, a thorough diagnostic check was performed on the residuals both visually and statistically (Serber & Lee, 2003). Visually, the residuals were checked for non-linearity, normality, equal variance, and for influential outliers, whereas the residuals were statistically checked for normality using a Shapiro-Wilk's test (Serber & Lee, 2003). The residuals were then split into two groups using the model's median as a cutting point, and a F-test was performed to compare the variances. A suite of statistical measures (Cook's Distance and leave-one-out) were used to check for influential outliers. The models were then reduced using the Akaike Information Criterion (AIC) in a hybrid stepwise approach in the stats package in R (Yamashita et al., 2007; R Core Team, 2022). After, the models checked for multicollinearity using a Variance Inflation Factor (VIF < 4; Serber & Lee, 2003). A simple model comparison using the function 'anova' was

performed in the car R package to test if each full model was statistically different from its reduced version (Fox & Weisberg, 2019). The residuals of each reduced model were subsequently checked for significant autocorrelation using a PACF and a Durbin-Watson statistic (Inder, 1984). A final step included the selection of the best model based on a series of statistical diagnostics such as the AIC, Bayesian Information Criterion (BIC), and model explanatory power (adjusted R^2). Models with a selection criteria of an AIC more than two units lower than the others were selected as best models of groundwater transit time (Burnham and Anderson, 2002).

Chapter 3 Results

3.1 A New Network of Tree-Ring Data

For this research, six newly developed hydroclimate-sensitive Douglas-fir (*Pseudotsuga menziesii)* chronologies (waterfront and control) have been created (sampled, mounted, surfaced, delineated, cross-dated) for the 1614 to 2021 AD period (i.e., the final SSS-truncated chronologies; Table 3.1; Figure A.1., A.2.). The average age of the trees that make up the control chronologies was 371 years, but individuals ranged from 291 to 688 years old. The mean age of trees that make up the waterfront chronologies was younger, at 341 years old, but individuals ranged from 164 to 614 years old. The series intercorrelation value, which characterizes the 'tightness' of the chronology among trees, for the waterfront chronologies range from 0.445 to 0.565, while the control chronologies range from 0.453 to 0.590. The mean sensitivity, which reflect year-to-year variation in ring width, was as low as 0.178 and as high as 0.314, and the total RBAR, which is the mean correlation coefficient between all tree-series, ranged from 0.311 to 0.481 (Table 3.1).

Table 3.1 Description of chronologies included in this study.

Chronology	Length (yrs)	SSS Length (yrs)*	Series (tree cores)	Series intercorrelation	Average mean sensitivity	RBAR
CLW TRW	1407 - 2021	1626 - 2021	56	0.565	0.185	0.323
CLW EW	1407 - 2021	1626 - 2021	56	0.550	0.194	0.311
CLW LW	1407 - 2021	1637 - 2021	56	0.445	0.306	0.481
Control TRW	1333 - 2021	1614 - 2021	57	0.590	0.178	0.351
Control EW	1333 - 2021	1614 - 2021	57	0.569	0.191	0.322
Control LW	1333 - 2021	1624 - 2021	57	0.453	0.314	0.392

**Sub-Sample Strength (SSS) represents the most robust timespan of the chronology.*
**Total ring width (TRW), earlywood (EW), latewood (LW), Clear Lake Waterfront (CLW)*

3.2 Climate-Growth Relationships

This study examined the influence of monthly variations in air temperature and total precipitation from 1895 to 2021 and SWE and gauge height from 1959 to 2021 on radial tree-growth at Clear Lake's headwaters. The monthly average air temperature during this period was 7.2 ℃, although monthly minimum and maximum temperature ranged from as low as -7.7 ℃ and as high as 19.6 ℃ (Table A.1.). On average, this region received 111.6 mm of SWE per month, but values have been recorded as high as 1097.8 mm during abnormally wet months and as little as 0.071 mm during exceptionally dry months. During winter months (i.e., December to February), monthly SWE totals averaged 332.7 mm. Monthly precipitation totals averaged 176.9 mm, with the highest recorded value of 885.4 mm and the lowest at 0.001 mm. Monthly gauge height on average raised 2.3 inches, but streamflow has been recorded to raise a maximum of 4.6 inches and a minimum of 0.001 inches in a month. The mid to late spring months, from April to June, saw an average monthly air temperature of around 9 ℃ and a mean monthly gauge height of 2.9 inches, which corresponds with the timing of peak snowmelt. In contrast, the late summer months, from July to September, a period most stressful for tree-growth, displayed monthly gauge height averages of 1.7 inches and monthly air temperature averages of 15.1 ℃.

Individual climate-growth correlations were performed to evaluate which variables are most influential on tree-growth at the two sites and to explore the geo-hydro-ecological mechanisms behind differences in tree-growth response between the control and waterfront standard chronologies. At the monthly resolution, the results for the precipitation-growth analysis for the total ring width waterfront chronology indicate a

significant positive correlation between current year growth and monthly total precipitation during previous year's August and current year's March and June. In contrast, monthly total precipitation in August of the current growth year has a significant negative relationship (Figure 3.1). There is also a significant positive relationship between total ring width and monthly mean air temperatures during previous year's November and current year's March.

At the bi-monthly resolution (2-month aggregation, reflecting the last month of the aggregation), and somewhat similar to the monthly results, the precipitation-growth relationship results display significant positive relationships between total ring width at the waterfront and previous July, August, and September and current year March, April, May, June, and July monthly total precipitation. However, significant negative correlations were found between current year August and September precipitation and total ring width growth. Additionally, a significant positive relationship between total ring width growth and mean air temperatures for previous year's November, December, and current year's January, March and April were found (Figure 3.1).

Additionally, at a six-month seasonalized scale (i.e., aggregated 6 months prior to the month noted in the figure) there is a significant positive correlation between radial growth at the waterfront site and previous year spring to early fall precipitation and spring precipitation in the current year, but during winter this relationship is more muted. Lastly, there is a significant positive relationship with current year's winter and spring monthly air temperatures (Figure 3.1). The growth of trees at this site have a weak relationship with winter precipitation, which is often in the form of snow, but the significant positive relationship with air temperatures as it begins to warm up in the

spring might indicate a period when (1) snowmelt waters become available for tree-growth or (2) when trees exhibit an earlier onset of growth, leading to a longer growing season.

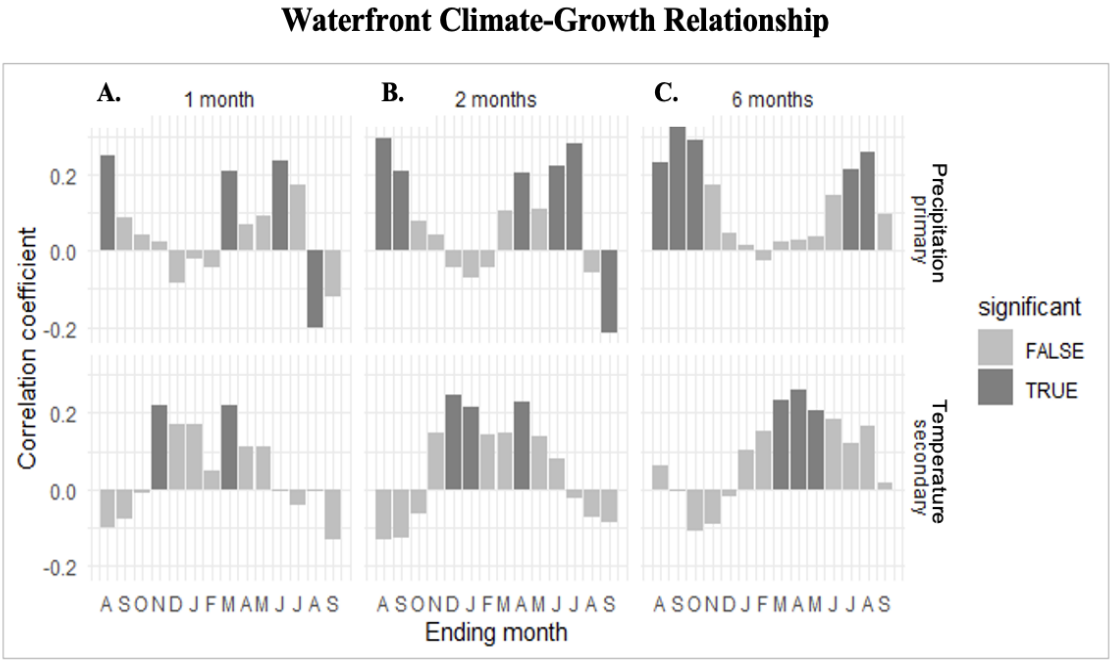

Figure 3.1 Monthly and seasonalized correlation function coefficients between the Douglas-fir (*Pseudotsuga menziesii*) total ring width chronology at the waterfront and total monthly precipitation (top panels) and mean air temperature (bottom panels). On the x-axis (Ending months), the first letter to the left of each panel (A) refers to August of the previous growth year, and the last letter to each panel's right (S) refers to September of the concurrent growth year. Dark bars represent significant correlations ($p < 0.05$) for 1-month (A), 2- month (B), and 6- months (C) with total precipitation (primary correlation) and mean air temperature (secondary/partial-correlation). The 2- and 6-months aggregated values reflect the last month of the aggregation, e.g., F in the 2-month top panel equals the growth response to total precipitation during January and February of the growing year. Monthly climate parameters, gridded at the 4 km^2 spatial resolution, were obtained from PRISM (PRISM Climate Group, 2014.) and correlation coefficients are for the 1895-2021 period.

The total ring width of the control chronology displays a relatively similar relationship with precipitation as the waterfront site at all three tested temporal resolutions (monthly, bimonthly, and seasonal); e.g., a significant positive correlation was found with previous year August (monthly), August and September (bimonthly), and August through November (6-months). Instead, temperature conditions at the control had little to no effect on total ring width (Figure 3.2).

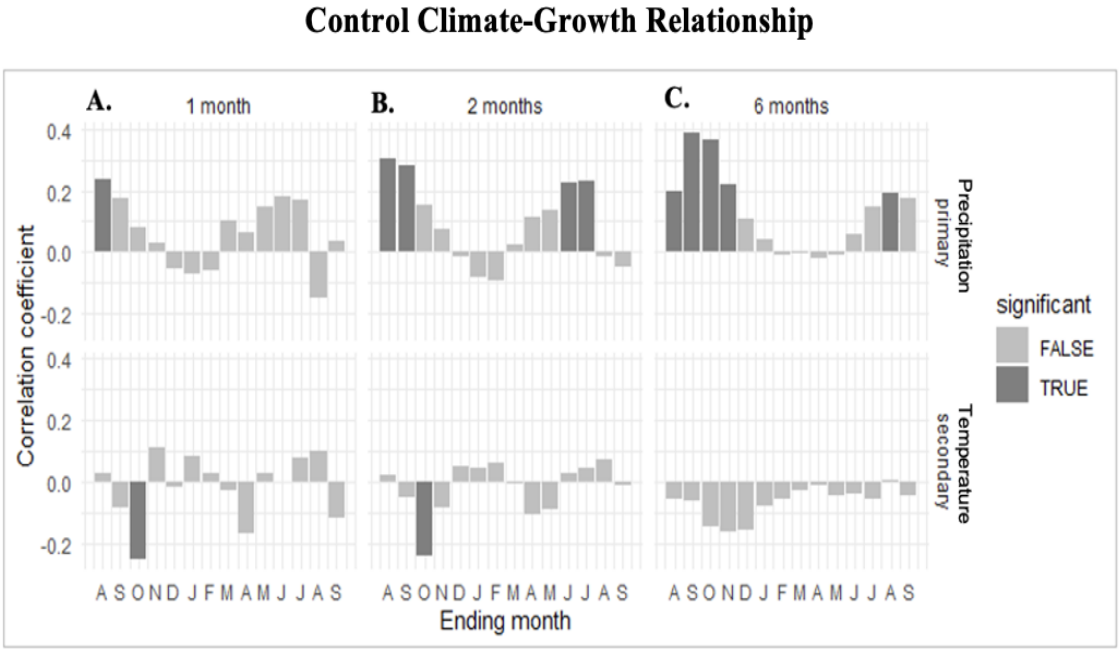

Figure 3.2 Monthly and seasonalized correlation function coefficients between the Douglas-fir (*Pseudotsuga menziesii*) total ring width control chronology and total monthly precipitation (top panels) and mean air temperature (bottom panels). On the x-axis (Ending months), the first letter to the left of each panel (A) refers to August of the previous growth year, and the last letter to each panel's right (S) refers to September of the concurrent growth year. Dark bars represent significant correlations ($p < 0.05$) for 1-month (A), 2- month (B), and 6- months (C) with total precipitation (primary) and mean air temperature (secondary). The 2- and 6-months aggregated values reflect the last month of the aggregation. Monthly climate parameters, gridded at the 4 km^2 spatial resolution, were obtained from PRISM (PRISM Climate Group, 2014.) and correlation coefficients are for the 1895-2021 period.

From the dozens climate-growth analyses performed for this study (Figures A.3. to A.18.), one that stood out is the relationship between the latewood (summer growth) waterfront chronology with the lake outlet stream gauge and precipitation records (Figure 3.3). Results suggest significant positive correlations between latewood growth and streamflow at all temporal scales, particularly during the spring and drier summer months. Specifically, a significant positive correlation with previous year's December and current year's April and August (monthly), previous February to current year's May (bimonthly), and previous November through current year's August (6-months) was found. These results also indicate that latewood growth responds positively to late spring-early summer precipitation.

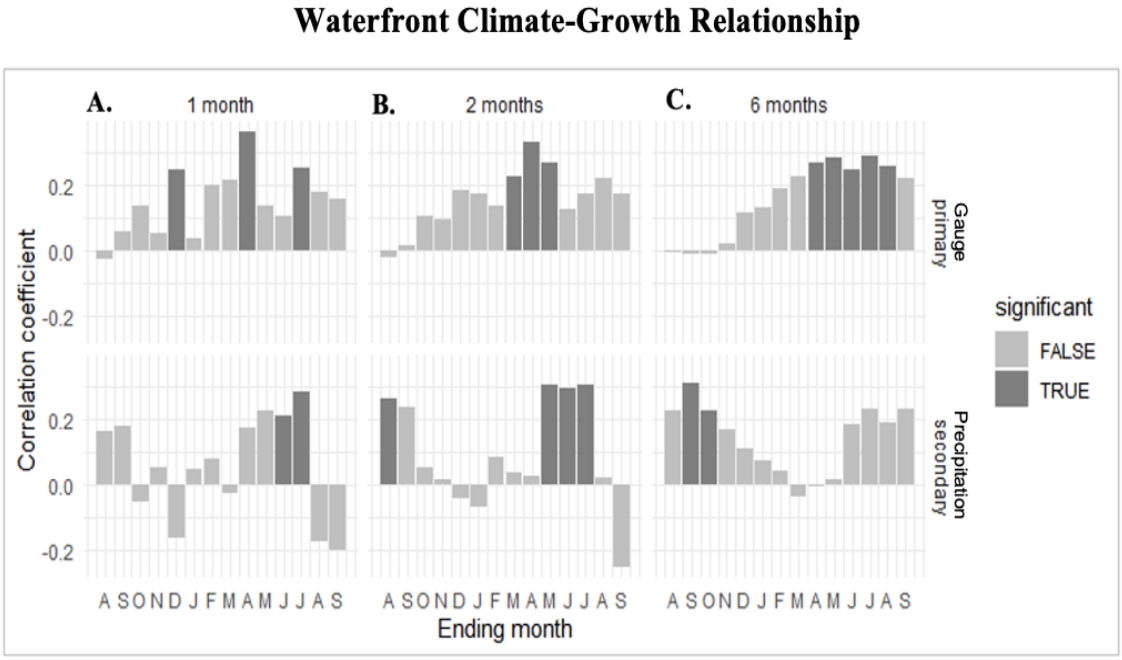

Figure 3.3 Monthly and seasonalized correlation function coefficients between the Douglas-fir (*Pseudotsuga menziesii*) latewood chronology at the waterfront and total monthly gauge height (top panels) and total monthly precipitation (bottom panels). On the x-axis (Ending months), the first letter to the left of each panel (A) refers to August of the previous growth year, and the last letter to each panel's right (S) refers to September

of the concurrent growth year. Dark bars represent significant correlations ($p < 0.05$) for 1- month (A), 2- month (B), and 6- months (C) with mean gauge height (primary) and total precipitation (secondary). The 2- and 6-months aggregated values reflect the last month of the aggregation. Monthly total precipitation, gridded at the 4 km^2 spatial resolution, was obtained from PRISM (PRISM Climate Group, 2014.), and monthly average gauge height of the McKenzie River at the outlet of Clear Lake was extracted from USGS (USGS, 2021). Correlation coefficients are for the 1959-2021 period.

3.3 Groundwater Transit Time Models

Significant partial autocorrelation was found between tree-growth in year *t* and growth up to lag *t-3* for the waterfront and control standard chronologies (Figure 3.4; i.e., for all three chronologies: total ring width, earlywood, latewood).

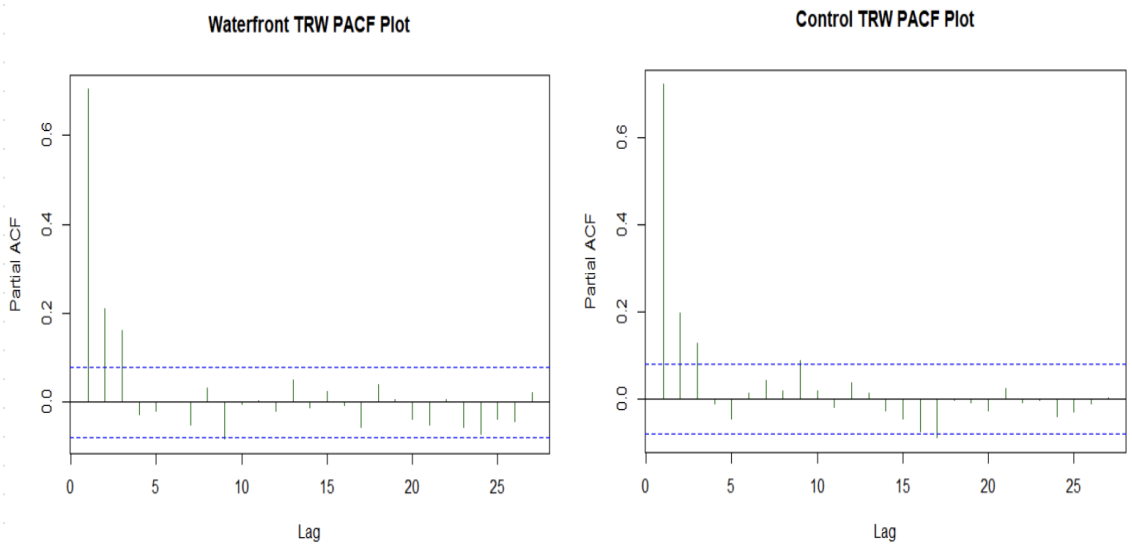

Figure 3.4 Partial Autocorrelation Function (PACF) of the waterfront and control total ring width chronologies. The x-axis represents lagged values ranging from 0-30 and the y-axis displays correlation coefficient values. The direction of each line represents the direction of the relationship, with significant relationships extending beyond the dashed blue 95% confidence interval line.

The chronology lag position in the model is indicated within the model equation below (3.1). The first set of regression analyses used the total ring width chronologies

(predicting tree-growth during year *t* at waterfront site). At this analysis, lags 5 and 6 resulted in the models that had greater than two AIC units from the rest, with a 6-year lag having the lowest AIC values, highest r^2_{adj} values, and lower RSMEv values (Tables 3.2, A.3.). The model with a 5-year lag explains 24% of the variance of tree-growth of the waterfront cohort, with an equation of:

$$Y = 0.5348 + (0.3813 \times CLW; t-1) + (0.1038 \times CLW; t-2) + (0.0881 \times CLW; t-3) - (0.1159\, CLL; t-5) \qquad (3.1)$$

The model with a 6-year lag also explains 24% of the variance of tree-growth of the waterfront cohort, with an equation of:

$$Y = 0.5446 + (0.3656 \times CLW; t-1) + (0.0991 \times CLW;\ t-2) + (0.1022\, x\, CLW; t-3) - (0.1196 \times CLL; t-6) \qquad (3.2)$$

The residual diagnostic analysis confirmed the above models met the assumptions of linear regression modeling as well as have significant F-statistics indicating the models are not overfit (Tables 3.3, 3.4; Figures A.21., A.22., A.23., A.24.).

Table 3.2 Model summary statistics from the best linear regression models produced in the first set of analyses that were performed to predict the tree-growth at the waterfront site.

# of years lagged backward	R^2	Adj.R^2	AIC	BIC	F	SE	RSMEv

6	0.252	0.241	-1025.2	-998.3	28.67	0.123	0.122
5	0.249	0.238	-1023.9	-997.0	37.00	0.123	0.123

Table 3.3 Descriptive statistics on model predictors that were included in best model output for the first set of regression analyses that were performed to predict the tree-growth at the waterfront site (*t*-5).

Name	**Value**	**SE**	**t-value**	**p-value**
Intercept	0.5347	0.0754	7.091	**7.76e-12**
Waterfront *(t-1)*	0.3812	0.0535	7.121	**6.43e-12**
Waterfront *(t-2)*	0.1038	0.0572	1.812	0.07086
Waterfront *(t-3)*	0.0880	0.0536	1.642	0.10141
Control *(t-5)*	-0.1159	0.0437	-2.648	**0.00847**

Table 3.4 Descriptive statistics on model predictors included in the top best model output for the first set of regression analyses that were performed to predict the tree-growth at the waterfront site (*t*-6).

Name	**Value**	**SE**	**t-value**	**p-value**
Intercept	0.5446	0.0769	7.077	**8.47e-12**
Waterfront *(t-1)*	0.3655	0.0540	6.765	**5.84e-11**
Waterfront *(t-2)*	0.0990	0.0572	1.731	0.0843
Waterfront *(t-3)*	0.1021	0.0535	1.908	0.0572
Control *(t-6)*	-0.1196	0.0440	-2.713	**0.0070**

Similarly, the first set of regression analyses for the earlywood chronologies led to comparable results, with a 5-year lag and 6-year lag yielding the models with greater than two AIC units from the rest (Table A.4.). The best models for the latewood chronologies for this part of the analysis were found to be a 15-year lag and 6-year lag (i.e., less than 2 AIC units apart; Table A.5.). All three chronology types (total ring width,

early-, and late-wood) displayed a 6-year lag as a top candidate model in the first set of regression analyses.

The second set of regression analyses using the total ring width control chronology displayed no significant results for a 6-year lag. Instead, the best model resulted at a lag of 19 (Table 3.5). The model with a 19-year lag in the second regression analysis explains 40% of the variance in tree-growth at the control site, with a regression equation of:

$$Y = 0.4893 + (0.5295 \times CLL; t-1) + (0.0601 \times CLL; t-2) + (0.0574 \times CLL; t-3) - (0.1438 \times CLL; t-19) \qquad (3.3)$$

Table 3.5 Descriptive statistics for the model predictors included in best model output for the second set of regression analyses that were performed to predict the tree-growth at the control site.

Name	Value	SE	t-value	p-value
Intercept	0.5020	0.0649	7.726	**1.17e-13**
Control lag 1	0. 5357	0.0526	10.181	< **2e-16**
Control lag 2	0.0920	0.0521	1.767	0.078087
Control lag 19	-0.1375	0.0410	-3.347	**0.000904**

Table 3.6 Model summary statistics for the second set of regression analyses that were performed to predict the tree-growth at the control site (*t*-19).

# of years lagged backward	R^2	Adj.R^2	AIC	BIC	F	SE	RMSEv
19	0.403	0.396	-510.2	-486.9	78.8	0.117	0.117

After meeting the residual assumptions and presenting a significant F-statistics, it was determined the model did not overfit (Table 3.6). Lastly, the RMSEv for the 19-year

lagged model is 0.117. There were no commonalities found between the total ring width, earlywood, and latewood chronologies for the second set of regression analyses when comparing the models with an AIC at least two units lower than the others (Tables A.6., A.7., A.8.). Therefore, it is determined the signal appearing in the first set of regression analyses at lags 5 to 15 is a groundwater signal and that there is likely no cyclical climate pattern significantly affecting both sites, at least equally since: (1) latewood radial growth of trees at the waterfront site significantly respond to lake levels when groundwater is the primary source of water entering Clear Lake (Figure 3.3), (2) factors influencing radial growth (other than groundwater) at both sites were meticulously controlled for, and (3) the same significant lagged models did not appear in each of the two regression analyses (i.e., top 6 lags of each).

Chapter 4 Discussion and Conclusion

4.1 Groundwater Transit Time

By implementing a novel dendrohydrological approach, groundwater transit time discharged into Clear Lake from underground springs in the High Cascade mountains was estimated at 5- to 15-years. Radial growth of trees located at the lake's waterfront and upslope (control) from Clear Lake is generally favored by above average precipitation the prior (summer) and concurrent (spring) years, whereas temperature- and stream gauge-growth relationships differed between both sampled populations and between total-, early-, and late-wood standard chronologies, respectively.

In Oregon's western Cascades, there is a prominent age class of old-growth stands dominated by Douglas-fir of ca. 450-500 years old that regenerated as a cohort following widespread fires in the late 1400s and 1500s (Weisberg and Swanson, 2003; Poage et al. 2009; Tepley et al. 2013). Very few stands that escaped these and other older widespread fires have Douglas-fir that are ca. 800 years old and older (Giglia 2004). The large majority of Douglas-fir old growth stands across Oregon's Cascades and coastal range, however, are ca. 200-300 years old, which is consistent with the chronologies used for this study after being truncated (Beedlow et al., 2013; Restaino et al., 2016).

Prior to selecting a chronology type for analysis, climate-growth relationships with the standard- and residual- chronologies were examined. At both sites, the total ring width standard- and residual- chronology displayed relatively similar relationships with total monthly precipitation and monthly mean air temperature at all three tested temporal scales (monthly, bimonthly, and 6-months seasonalized; Figures 3.1, 3.2, A.2.-A.5., A.11.-A.13.). Thus, the standard type of tree-ring chronologies (contains autocorrelation;

in contrast to pre-whitened residual chronologies) were selected for further analysis, which is a common practice in dendroclimatic and dendrohydrological studies (Coulthard et al., 2020; Coulthard et al., 2021). Utilizing the standard chronologies enabled this research to account for: (1) the potential influence of hydroclimate processes on radial growth prior to the year of ring formation, as identified by Cook (1985) and Cook and Kairiukstis (1990); and (2) the presence of autocorrelation in the hydroclimate processes themselves. Therefore, our groundwater transit time reconstruction model and climate-growth relationships capitalized on the statistically persistent tree ecophysiology and hydroclimatic processes at play.

The best individual models of total ring width developed for this study explain 24% and 40% of variance in tree-growth at each site, respectively in the High Cascades. To the best of my knowledge, this is the first study of its kind and thus there is no existing literature to compare the variance of the models to. It is sensible to assume that non-exclusive site characteristics that influence tree-growth, but that were intentionally left out of the models (climate, nutrients, environmental disturbances, competition, and topographic location) would account for their unexplained variance. Alternatively, the influence of top-down parameters (i.e., climate) were directly examined through separate analyses at both sites, while other bottom-up variables were controlled for, e.g., site selection to account for variation in nutrients and water holding capacity, individual tree selection to account for disturbance, reduced competition, growth sensitivity, and detrending to account for age and size-related changes in radial growth. However, given the unique geology of the McKenzie River Basin and the torturous path of interstitial water, it is hypothesized that the groundwater transit process could be a continuous

phenomenon that spans over a period of 5- to 15-years (i.e., rather than operating at an annual scale), which can account for the remaining unexplained variance in the models. For example, individual significant lags, which could be viewed as a pulse signal from a previous input, may be less robust in describing a complex process (e.g., variance in tree growth at the waterfront site). However, combining these significant lags into a range of 5- to 15- years, might collectively better describe groundwater transit time for this basin, with a 6-year lag displaying the most frequent significant lag (Tables A.4.-A.8.). Including the significant 15-year lag in this range from the model performed using latewood growth is further strengthened by the significant positive correlation found between latewood growth at the waterfront site when paired with spring and summer lake levels (i.e., when groundwater is the primary source entering into Clear Lake; Figure 3.3). This interpretation of a range of groundwater transit times aligns with previous literature, such as Grant et al. (2004)'s work which found a range of 5 to 10 years and Jefferson et al. (2006)'s research that found a range of 13 to 26 years.

Based on model performance metrics, the lag *t-6* appeared as the best groundwater transit time when predicting radial growth at the waterfront in all three chronologies (total ring width, early-, late-wood). The gauge-growth relationship revealed late-wood growth significantly increases when lake levels are elevated during the spring and summer during the growing season (i.e., bimonthly and 6-months seasonalized; Figure 3.3; Table A.2.). These results also correspond with the positive growth response to warm conditions in spring at the waterfront site. My findings align with Restanio et al. (2016)'s findings that radial growth of Douglas-fir growing in the western United States, including trees in the Oregon Central Cascades (HJA

Experimental Forest) and the Northern Cascade National Park in the PNW, is highly sensitive to soil moisture deficits. Therefore, the positive moisture-growth relationship at the waterfront site may be explained by higher lake levels preconditioning the soil with moisture for a time when latewood is actively growing (i.e., summer, when precipitation is scarce). These findings support the previously reported influence of summer maximum temperature and summer Vapor Pressure Deficit (VPD) on radial growth (latewood carbon isotope discrimination) of Douglas-fir trees growing higher up at Santiam Junction Pass in Oregon (Ratcliff et al., 2018). Overall, my results also complement well with the proportionally colder summer water, which is when the primary source water for Clear Lake is groundwater (Jefferson et al., 2006; Tague et al. 2008), making the latewood chronology a sound groundwater proxy.

At the control site, the weak negative temperature influence on growth suggests the notion that these trees do not benefit from earlier snowmelt, as they cannot access that water. These differences in temperature-growth findings between the waterfront and control site further highlight the waterfront site benefits from access to groundwater that likely does not exist at the control site. Previous studies have shown that Douglas-fir radial growth (total ring width, early-, and late-wood) at higher elevation (at Santiam Junction pass; 1,139 m) had no statistically significant response to climate (i.e. temperature, precipitation or SWE; Ratcliff et al. 2018), suggesting that at the elevation of, and/or in response to dry lava-rich substrate conditions at Clear Lake, growth of Douglas-fir trees is moisture-limited, rather than energy-limited.

In contrast to the moisture-limitation during summer (latewood growth) findings, earlier than average radial growth (earlywood) of trees at the waterfront is favored by

warmer than average conditions that likely lead to earlier than normal snowmelt timing (Figure A.6.). At the control site, cooler conditions earlier in the fall of the previous season is associated with increased latewood and total ring width growth, implying a memory effect from stressed trees (Esper et al., 2015).

Utilizing a PACF, significant partial autocorrelation was found up to lag *t-3* in tree-growth at the waterfront site with the growth of the same waterfront trees in year *t* as well as with tree growth at the control site with the same control trees in year *t*. Since tree-growth at both sites is governed by the same local climate, it is likely that the difference in autocorrelation in radial growth is due to the growth response to hydroclimatic processes at both sites prior to the ring formation, and the natural existence of autocorrelation in hydroclimatic processes. Of the predictors included in the best total ring width model for the first set of regression analyses, waterfront tree-growth at *t-1* exhibits the strongest positive linear relationship with tree-growth at the waterfront site in year *t* (Tables 3.3, 3.4). This high 1-yr autocorrelation is a common signature in tree-ring time series, associated with non-structural carbon reserves (Schweingruber, 1996; Esper et al., 2015). Although not as strong as waterfront tree growth at *t-1*, tree growth at the control site at *t-6* displays a significant negative linear relationship with tree-growth at the waterfront site in year *t*. In this circumstance, it is sensible to infer that the negative relationship found between the control site at *t-6* and the waterfront site at year *t* could be explained by the differences in spring temperature- and winter SWE-growth relationships at each site. More specifically, at the waterfront site, warm spring air temperatures seem to trigger an early onset of growth. However, warm spring conditions appear to be less favorable for tree growth at the drier, lava-rich control site (Table A.2.). These findings

are consistent with previous literature which has repeatedly found that Douglas-fir growth is limited by warm spring and summer air temperatures in the western United States (Restiano et al., 2016; Beedlow et al., 2012; Littel et al., 2008).

Furthermore, variability in tree-growth at the waterfront site for year *t* might also be minorly dictated by tree-growth at the waterfront site in years *t-3* followed closely by *t-2*. Although the model results did not indicate lags *t-3* and *t-2* were significant predictors of waterfront tree-growth in year *t*, they were retained in the final regression analyses due to: (1) hypotheses formed based on the significant partial autocorrelation values in the PACF analysis; and (2) having higher-quality model metrics (i.e., lower AIC, higher Adj.R^2, etc.). The function 'anova' was used to compare the full model (i.e., included all predictors) with a reduced version that excluded insignificant predictors (lags *t-3* and *t-2*), which showed that the full model was a statistically better fit than the reduced version. Therefore, of the four predictors included in the first set of total ring width regression analyses, two displayed statistically significant relationships with tree-growth at the waterfront site at Clear Lake, Oregon. Similar results were found in the first set of regression analyses using the early- and late-wood chronologies.

Lag *t-19* emerged as a best model for the second set of total ring width regression analyses, explaining 40% of variance in tree-growth at the control site in year *t*. Of the predictors included in the final total ring width model, control tree-growth at *t-1* exhibits the strongest positive linear relationship with tree-growth at the control site in year *t* (Table 3.5). Drawing from the climate-growth analysis, pre-conditioning soil moisture which in turn stimulates an increase in tree-growth in year *t* can be inferred from the observed growth response associated with increased precipitation (Figure 3.2) and cooler

fall conditions (presumably lessen evapotranspiration, Figures A.8., A.9., A.10.) prior to the growing season (*t-1*).

Though not as strong as the slope for the control tree-growth at *t-1*, tree-growth at the control site at *t-19* displayed a significant negative linear relationship with tree-growth in year *t*. These results could indicate a frequency associated with longer-term climate modes, such as the PDO, which mediates the climate and atmospheric circulation patterns in the PNW at 20- to 30-year timescales (Praskievicz & Chang, 2009; Hamlet & Lettenmaier 1999). However, Mantua and Hare (2002) reported it has exhibited two warm (positive) periods in the 20th century, one ranging from 50 to 70 years and the other from 15 to 25 years. Furthermore, Case and Peterson (2005) show that high elevation Douglas-fir are negatively associated to winter PDO index prior to the growing season, and Pohl et al. (2013) reported ponderosa pine (*Pinus ponderosa*) recording weak PDO signals in central Oregon (east Cascades), explaining only 12% of variance in tree-growth. Thus, the 19-year lag may be indicative of such signal, emphasizing the importance of further exploring the mechanisms governing it.

In addition, variability in tree-growth at the control site for year *t* might also be minorly dictated by tree-growth at the control site in year *t-2*. Despite not being found as a significant predictor, *t-2* was kept in the second regression analyses due to hypotheses formed based on the significant lags found in the PACF analysis and improved model metrics (i.e., lower AIC, higher Adj.R^2, etc.). A reduced model containing only significant predictors (i.e., without lag *t-2*) was compared to the full model (i.e., containing lag *t-2*) using the function 'anova', and the results indicated the full model was a statistically better fit than the reduced version.

In contrast to the first set of regression analyses, the resulting *t-19* lag was not found as a best model in the set of regression analyses using the earlywood chronology. However, Peterson and Peterson (2001) discovered mountain hemlock (*Tsuga mertensiana*) growing at low-elevation sites (i.e., elevations ranging from 1100 m to 1585 m asl) in central Oregon exhibited negative correlations with current growth year summer air temperatures that were associated with decadal variability in the PDO. Ratcliff et al. (2018)'s work on mountain hemlock and Douglas-fir tree-ring carbon isotope (^{13}C) responses to climate showed that latewood exhibited stronger responses to climate than its earlywood and total ring width counterparts; while mountain hemlock, as most shade tolerant species that gradually, transitions from early- to late-wood (rather than abruptly as Douglas-fir; Ratcliff et al., 2018). Peterson and Peterson (2001)'s work suggest that the likelihood of detecting a PDO signal may be higher in latewood growth compared to earlywood, as latewood develops during the late summer months coinciding with the period in which these associations were identified, in trees at a nearby location and elevation range. My stationarity analysis suggests the influence of PDO, as climate-growth relationships change in strength in the ca. 1940s and in the ca. 1970s, decades when PDO changed signs across the Pacific Ocean basin (Figures 3.4, 4.1, A.20.).

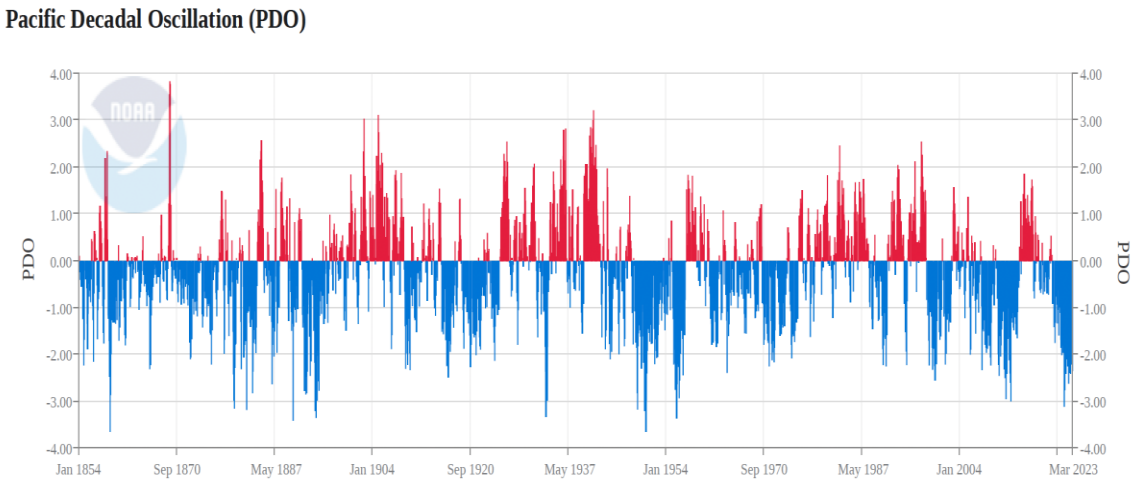

Source: https://www.ncei.noaa.gov/pub/data/cmb/ersst/v5/index/ersst.v5.pdo.dat

Figure 4.1. A time series plot extracted from National Oceanic and Atmospheric Association (NOAA, 2023) representing the natural variability in North Pacific SST over the past century through Pacific Decadal Oscillation (PDO) index values. The PDO index value is measured in standard deviation units from the long-term mean of sea surface temperature (SST) in the North Pacific Ocean. The x-axis represents the years, starting from January 1854 and extending to present day, while the y-axis represents the PDO index value. The plotted time series illustrates a fluctuating pattern of positive and negative PDO phases over time, with some periods lasting for several decades. The positive (red) PDO phases are characterized by warmer-than-average SST in the North Pacific, while the negative (blue) PDO phases are characterized by cooler-than-average SST, e.g., the most recent PDO phase from approximately April 2018 to present day is highlighted in blue indicating the PDO index value was mostly negative, and SSTs were cooler-than-average in the North Pacific.

4.2 Comparison with Existing Literature

Results from this study indicate a time lag between groundwater recharge and discharge at Clear Lake ranging from 5- to 15-years, consistent with Grant et al. (2004)'s findings of young groundwater transit times ranging from 5- to 10-years for the Great Spring and Jefferson et al. (2006) findings of 12.9- to 26- ($\pm$1) years, depending on the method used. Contrarily, these results conflict with transit times found in 2009 by Deligne (*unpublished*) of 30 to 31 years. Nonetheless, the *t-6* lag was found to be

statistically significant in Deligne's model. The discrepancy between resulting ranges for groundwater transit times could be explained by Jefferson et al. (2006) use of gamma and simple exponential distributions to track groundwater transit times in a study area that has complex hydrogeology. These methods are meant to estimate transit times through porous medium, such as the High Cascades, but may yield unreliable results if there are zones within the aquifer of interconnected fractures with considerable flow or with stagnant water, characteristics that were unknown at the time of the study (Mazor and Nativ, 1992; Maloszewski et al., 2004 Jefferson et al., 2006). Additionally, Grant et al. (2004) and Jefferson et al. (2006) studies lacked replication (i.e., they only collected water in 1-2 years), which can be problematic as regional snowpack varies naturally internally from influences of climate variability. In contrast, this novel dendrohydrological approach, which captures multi-century variability in growth responses to climate, may be a more robust method in fine tuning a groundwater transit time range.

Furthermore, the study performed by Deligne (*unpublished*) suggested transit times of 30 to 31 years, yet had a relatively small sample size (i.e., only 15 paired increment tree cores per site), only evaluated ~200 years, and did not control for key geological differences between the High and Western Cascades (Ratcliff et al., 2018), all of which this thesis corrected for. For example, for this study, the period of analysis was doubled from 200 to 400 years using reliable and robust total ring width, early-, and late-wood chronologies that were produced from 30 paired increment cores per site (i.e., increased sample size). Additionally, previous studies have determined that recharge for

the Great Spring likely originates in the Sand Mountain's young lava outcrops, east of Clear Lake in the High Cascades, where the control site was located for this study (Jefferson et al., 2006; Grant et al., 2004). This accounted for previous findings which emphasized that the young mafic outcrops west of the High Cascades play a foundational role in dictating groundwater flow patterns (Jefferson et al., 2006).

4.3 Water Management and Future Trends

According to projections made by Leung et al. (2004), Oregon's Cascade snowpacks are expected to decrease to less than half of present-day size by 2050. This could result in significant water shortages during the summer's low-flow period as indicated by Jefferson et al. (2008). Over the last six decades, winters have become warmer, and snow has melted earlier, causing alterations in the hydrograph (Tague and Grant, 2009). As a result, summer recessions are persisting 17 days longer, August discharges have decreased by 15%, and autumn minimum discharges have decreased by 11% (Jefferson et al., 2008, Tague et al., 2009). Future climate projections suggest this trend will remain for the next 50 to 100 years. Rivers that are dominated by groundwater are more susceptible to changes in the amount of snowmelt and the timing compared to those dominated by runoff due to their slow recession (Jefferson et al., 2008).

When compared to quicker draining watersheds with identical timing of peak snowmelt, the McKenzie basin demonstrates a 4-fold reduction in summer streamflow. According to Tague and Grant (2009), the McKenzie River is particularly sensitive to alterations in the amount and timing of snowmelt due to its low drainage efficiency. A 1.5°C warming is expected to result in snowmelt occurring earlier and reduced peaks of

snow accumulation, with the McKenzie basin having the highest changes in volume of melt compared to other rivers in the region (Tague and Grant, 2009). According to Jefferson et al. (2008), a previous study found that the McKenzie River's August discharge would decrease from current mean value by 23% if air temperatures increased by 2.8 °C. For perspective, the August flow at the McKenzie River at Clear Lake makes up 10% of the uncontrolled flow at the water intake, serving a population of more than 175,000 people in Eugene, Oregon (U.S. Census Bureau, 2021; Tague and Grant, 2009). As Milly et al. (2008) suggest, this challenges the idea of stationarity that has been the cornerstone of water management for many years (i.e., water policies in the west were written during the wettest decades on record in the 1910-1920s; Pisani, 2022). However, according to Heeter et al. (2023), if all obligations are fulfilled in a timely manner, there is a chance to achieve the long-term goal of the Paris Agreement and limit global warming to below 2.0°C and to pursue efforts to cap warming at 1.5°C above pre-Industrial levels.

It is widely acknowledged that climate change has global impacts. However, Leibowitz et al. (2014) suggest that the adaptation measures taken to manage natural resources in response to climate change should be primarily carried out at the local level. This study provides key results that are regionally relevant as disentangling groundwater dynamics at Clear Lake allows us to better understand a water supply that is critical for municipal drinking water, agriculture, and sustaining aquatic and wildlife habitats particularly in the warm season when water scarcity and demand are coincidently high. Because climate change is expected to have significant impacts on the McKenzie basin, it is essential to implement effective water management practices that guarantee sustainable

water usage. Grant et al. (2004) explains that to preserve the high-water quality and quantity of the McKenzie River, it is necessary to consider three different environments: 1) the extensive area upstream from the river, which remains poorly understood but contributes to the water flow in the springs; 2) the springs; and 3) the channel and riparian zones adjacent to the river.

Critical water management practices should be to implement water conservation measures, improve water quality, and protect riparian areas. A transit time ranging from 5- to 15-years indicates the system is consistently being recharged, and likely in balance with the annual amount that is discharged at the springs. Grant et al. (2004) proposed that spring water may be vulnerable to contaminants from atmospheric deposition or chemical spills in the upper recharge zones that could impact the water and persist for years after. Furthermore, projected changes in the quantity and form of precipitation in Oregon's western Cascades may be buffered by groundwater influx in spring-fed river systems compared to neighboring run-off dominated rivers. Nevertheless, implementing water conservation measures can help reduce water demand despite a growing population, while ensuring sustainable use of the McKenzie River's water resources by promoting water-efficient practices. By implementing this study's findings of a 5- to 15-year groundwater transit time, we can proactively devise strategies to mitigate the impact of low flow periods by increasing water storage during high flow periods. Utilizing such a forward-thinking approach can advance the overall resilience of water resource management practices in the face of a changing climate. An example of how this can be achieved is through the construction of new reservoirs or enhancing existing ones (e.g., Barnett et al. 2005). The 2022 and 2023 winters have resulted in deep snowpack, and as

this study suggests, should result in increased discharge in spring and summer 2027 to 2037, with the average pulse occurring in 2028 for managers to store.

Moreover, Leibowitz et al. (2014) reported that the coupling of summer low flows and maximum air temperatures in the western United States under projected anthropogenic warming may increase stress in aquatic life such as the salmonoid and bull trout population. This stress can be compounded with various low flow impacts such as reduced space, increased competition, a decrease of macroinvertebrate prey and other food sources, and a higher likelihood of parasite and disease; all of which can have adverse effects on growth and survival of river salmonoids and bull trout (Leibowitz et al., 2014). Grant et al. (2004) also noted that river temperature is a vital characteristic for the habitat of bull trout. However, it has been found that spring-fed rivers, specifically those with high-permeability aquifers, tend to buffer climate change impacts to river temperatures (Grant et al., 2004; Leibowitz et al., 2014). Nonetheless, this study's findings of groundwater transit times of 5- to 15-years can provide water managers the tools for proactive and strategic practices that allow for preservation of the ecological niches of these species by being able to anticipate periods of reduced flow. Jefferson and colleagues (2008) also reported a relationship between low flow and riparian vegetation mortality caused by drought stress. According to regional climate projections, these stressors will likely be exacerbated over the next 100 years by hotter and drier summers in the PNW (Jefferson et al., 2008). Riparian areas are critical for maintaining river ecosystem health and protecting water quality. Thus, conserving and restoring riparian areas can help reduce erosion and improve water quality while providing a vital habitat for fish and wildlife, e.g., restoration projects planned ahead of time of increased

discharge (2028-2029), so that planting mortality due to drought is reduced. Overall, applying effective water management practices for the McKenzie basin will necessitate the cooperation of both federal and local agencies, an assessment of the impact of human activity at the upstream recharge areas that influence the quantity and quality of water, and an analysis of how the McKenzie River behaves in the context of climate variability and change (Grant et al., 2004).

4.4 Future Work and Implications

This thesis research used a novel tree-ring-based approach to better define the groundwater transit time of the waters emanating into Clear Lake from the Great Spring. This approach can be utilized in alike basins with predominantly spring-fed rivers, such as the headwaters of the Clackamas River, a tributary of the Willamette River, under the assumption that watersheds which share similar climate and physical characteristics are likely to have similar hydrologic characteristics and responses. Additionally, this work explored the relationships between climate and tree-growth at Clear Lake to inform on groundwater transit time. Taking this information in tandem, findings suggest the latewood chronology is likely the best predictor of changes in lake levels and/or streamflow. Thus, utilization of latewood may prove to be crucial to advance knowledge on Douglas-fir species-specific sensitivity to changes in soil moisture in forests west of the Oregon's Cascades in response to drought-induced decline and mortality events (e.g., Eilmann et al., 2012; Keen et al., 2022). Lastly, groundwater transit time results used in tandem with climate interactions with the McKenzie River can inform climate forecasts used to predict water quality and availability for the McKenzie River, which serves as Eugene, Oregon's potable drinking water supply (McCarthy and Alvarez, 2014).

4.5 Conclusion

The McKenzie River is a critical water source for Oregon's most densely populated and water-intensive regions, providing water for agriculture, aquatic ecosystems, and recreation. This spring-fed river also serves as a dependable source of municipal drinking water for over 175,000 people residing in the Eugene area, effectively meeting their high water demands even throughout the dry summer months. Compared to runoff-dominated watersheds where subsurface storage is depleted every summer, groundwater-dominated watersheds discharge is sustained by aquifer storage and slow summer recessions even when the seasonal or annual water balance is negative (Jefferson et al., 2008).

Considerate interest should be given to our spring-fed rivers given that temperatures are projected to continue to increase in the PNW over the next century and will be coupled with decreased snowpack, earlier snowmelt timing, longer recessions, and decreased discharge. These phenomena challenge the idea of stationarity which has been foundational for water management practices for several years.

Using a novel dendrohydrological approach I was able to quantify groundwater transit times ranging from 5- to 15-years for the McKenzie River at its headwaters, Clear Lake, Oregon. These lag times are found to be consistent with other reports (Grant et al., 2004; Jefferson et al., 2006). This approach can be utilized in alike basins with predominantly spring-fed rivers, such as the headwaters of the Clackamas River. In addition to groundwater transit time, this research examined climate-growth relationships at two sites in the High Cascades. Results indicate the Douglas-fir stand growing east of Clear Lake in the lava fields (control) prefer cool, wet summers and mild winters. The

Douglas-fir stand growing around the lake's perimeter (waterfront) displayed a similar relationship with precipitation and summer temperature, except warm spring air temperatures seems to trigger early onset of the growing season in these trees while the control tree-growth appeared to be limited by this. Additionally, the latewood chronology appeared to be a promising groundwater proxy. Taken together, this thesis research improves our understanding of how groundwater can help sustain periods of low flow under a warming climate for the McKenzie River, Oregon, while also emphasizing the importance of future research in spring-fed rivers.

References

Abatzoglou, J. T. (2011). Influence of the PNA on declining mountain snowpack in the Western United States. International Journal of Climatology, 31(8). https://doi.org/10.1002/joc.2137

Abatzoglou, J.T., S.Z. Dobrowski, S.A. Parks, K.C. Hegewisch. (2018). Terraclimate, a high- resolution global dataset of monthly climate and climatic water balance from 1958-2015, Scientific Data 5:170191, doi: 10.1038/sdata.2017.191.

Anderson, D., & Burnham, K. (2004). Model selection and multi-model inference. *Second. NY: Springer-Verlag*, *63*(2020), 10.

Barnett, T. P. (2005). Potential impacts of a warming climate on water availability in snow-dominated regions. *Nature*, *438*(7066), 303–309. https://doi.org/10.1038/nature04141

Beedlow, P. A., Lee, E. H., Tingey, D. T., Waschmann, R. S., & Burdick, C. A. (2013). The importance of seasonal temperature and moisture patterns on growth of Douglas-fir in western Oregon, USA. *Agricultural and Forest Meteorology*, *169*, 174-185.

Berg, N., & Hall, A. (2017). Anthropogenic warming impacts on California snowpack during drought. *Geophysical Research Letters*, *44*(5), 2511-2518.

Bunn, A.G., 2008, A dendrochronology program library in r (dplr): Dendrochronologia, v. 26, no. 2, p. 115-124.

Buras, A. (2017). A comment on the expressed population signal. *Dendrochronologia*, *44*, 130-132.

Catalano, A. J., Loikith, P. C., & Aragon, C. M. (2019). Spatiotemporal variability of twenty-first- century changes in site-specific snowfall frequency over the Northwest United States. *Geophysical Research Letters*, *46*(16), 10122-10131.

Case, M. J., & Peterson, D. L. (2005). Fine-scale variability in growth climate relationships of Douglas-fir, North Cascade Range, Washington. *Canadian Journal of Forest Research*, *35*(11), 2743-2755.

Clackamas SWCD, (2013). *Cascades ecoregion*. https://conservationdistrict.org/discover/discover- ecoregions/cascades-ecoregion#:%7E:text=Average%20temperatures%20range%20from%2030,to%20142%20inches%20a%20year.&text=Extensive%20and%20highly%20productive%20coniferous%20forests.

Cook, E.R., and Kairiukstis, L.A., 1990,Methods of dendrochronology: applications in the environmentalmsciences: Springer Science & BusinessMedia.

Cook, E., 1985, A time series analysis approach to tree ring standardization [Ph.D. thesis]: University of Arizona.

Cook, E.R., and Briffa, K.R., 1990, A comparison of some tree-ring standardization methods, in Cook, E.R. and Kairiukstis, L.A. eds., Methods of Dendrochronology, Kluwer Dordrecht, p. 104–123.

Cook, E.R., and Kairiukstis, L.A., 1990, Methods of dendrochronology: applications in the environmental sciences: Springer Science & Business Media.

Cook, E.R., and Peters, K., 1997, Calculating unbiased tree-ring indices for the study of climatic and environmental change: {H}olocene, v. 7, p. 361–370.

Coulthard, B., St. George, S., and Meko, D., 2020, The limits of freely-available tree-ring chronologies:Quaternary Science Reviews, v. 234, p. 106,264, doi: 10.1016/j.quascirev.2020.106264.

Coulthard, B. L., Anchukaitis, K. J., Pederson, G. T., Cook, E., Littell, J., & Smith, D. J. (2021). Snowpack signals in North American tree rings. *Environmental Research Letters*, *16*(3), 034037. https://doi.org/10.1088/1748-9326/abd5de

Cybis Elektronik. 2010. CDendro and CooRecorder. http://www.cybis.se/forfun/dendro/index.htm.

Dannenberg, M. P., & Wise, E. K. (2016). Seasonal climate signals from multiple tree ring metrics: A case study of Pinus ponderosa in the upper Columbia River Basin. *Journal of Geophysical Research: Biogeosciences*, *121*(4), 1178-1189.

Deligne, N. 2009. Tracing Groundwater Through Volcanic Landscapes: Case study in the upper McKenzie River basin. Term paper for Advanced Biogeography (Landscape Ecology) Seminar. Department of Geography, University of Oregon. Instructor: Dr. Dan Gavin.

Eilmann, B., and A. Rigling. 2012. Tree-growth analyses to estimate tree species' drought tolerance. Tree Physiology 32:178–187.

Esper, J., L. Schneider, J. E. Smerdon, B. R. Schöne, and U. Büntgen. 2015. Signals and memory in tree-ring width and density data. Dendrochronologia 35:62–70.

Fayad, A., Gascoin, S., Faour, G., López-Moreno, J. I., Drapeau, L., Le Page, M., & Escadafal, R. (2017). Snow hydrology in Mediterranean mountain regions: A review. *Journal of Hydrology*, *551*, 374-396.

Fox, John and Weisberg, Sanford (2019). An {R} Companion to Applied Regression, Third Edition. Thousand Oaks CA: Sage. URL: https://socialsciences.mcmaster.ca/jfox/Books/Companion/

Fritts, H.C., 1976, Tree Rings and Climate: New York, Academic Press

Fritze, H., Stewart, I. T., & Pebesma, E. (2011). Shifts in Western North American Snowmelt Runoff Regimes for the Recent Warm Decades. Journal of Hydrometeorology, 12(5), 989–1006. https://doi.org/10.1175/2011JHM1360.1

Fyfe, J. C., Derksen, C., Mudryk, L., Flato, G. M., Santer, B. D., Swart, N. C., ... & Jiao, Y. (2017). Large near-term projected snowpack loss over the western United States. *Nature communications*, *8*(1), 14996.

Gergel, D. R., Nijssen, B., Abatzoglou, J. T., Lettenmaier, D. P., & Stumbaugh, M. R. (2017). Effects of climate change on snowpack and fire potential in the western USA. Climatic Change, 141(2). https://doi.org/10.1007/s10584-017-1899-y

Giglia, S. K. 2004. Spatial and Temporal Patterns of “Super-old” Douglas-fir Trees of the Central Western Cascades, Oregon. Oregon State University, Corvallis, Oregon.

Grant, Gordon, Anne Jefferson, and Sarah Lewis. *Discharge, source areas, and water ages of spring-fed streams and implications for water management in the McKenzie River Basin*. USDA, 2004.

Hamlet, A. F., & Lettenmaier, D. P. (1999). Columbia River streamflow forecasting based on ENSO and PDO climate signals. *Journal of water resources planning and management*, *125*(6), 333-341.

Harley, G. L., Maxwell, R. S., Black, B. A., & Bekker, M. F. (2020). A multi-century, tree-ring-derived perspective of the North Cascades (USA) 2014–2016 snow drought. *Climatic Change*, *162*, 127-143.

Harpold, A. A., Dettinger, M., & Rajagopal, S. (2017). Defining snow drought and why it matters. In Eos (United States) (Vol. 98, Issue 5, pp. 15–17). American Geophysical Union. https://doi.org/10.1029/2017eo068775

Heeter, K. J., Harley, G. L., Abatzoglou, J. T., Anchukaitis, K. J., Cook, E. R., Coulthard, B. L., ... & Homfeld, I. K. (2023). Unprecedented 21st century heat across the Pacific Northwest of North America. *npj Climate and Atmospheric Science*, *6*(1), 5.

Holmes, R. L. (1983). *COMPUTER -ASSISTED QUALITY CONTROL IN TREE -RING DATING AND MEASUREMENT*. 11. https://repository.arizona.edu/bitstream/handle/10150/261223/trb-43-069-_078.pdf

Inder, B. A. (1984). Finite-sample power of tests for autocorrelation in models containing lagged dependent variables. *Economics Letters*, *14*(2-3), 179-185.

IPCC, 2021: *Climate Change 2021: The Physical Science Basis. Contribution of Working Group I to the Sixth Assessment Report of the Intergovernmental Panel on Climate Change* [Masson-Delmotte, V., P. Zhai, A. Pirani, S.L. Connors, C. Péan, S. Berger, N. Caud, Y. Chen, L. Goldfarb, M.I. Gomis, M. Huang, K. Leitzell, E. Lonnoy, J.B.R. Matthews, T.K. Maycock, T. Waterfield, O. Yelekçi, R. Yu, and B. Zhou (eds.)]. Cambridge University Press, Cambridge, United Kingdom and New York, NY, USA, In press, doi:10.1017/9781009157896.

Jefferson, A., Grant, G., & Rose, T. (2006). Influence of volcanic history on groundwater patterns on the west slope of the Oregon High Cascades. *Water Resources Research*, *42*(12). https://doi.org/10.1029/2005WR004812

Jefferson, A., Nolin, A., Lewis, S., & Tague, C. (2008). Hydrogeologic controls on streamflow sensitivity to climate variation. *Hydrological Processes: An International Journal*, *22*(22), 4371-4385.

Keen, R. M., S. L. Voelker, S. -Y. S. Wang, B. J. Bentz, M. L. Goulden, C. R. Dangerfield, C. C. Reed, S. M. Hood, A. Z. Csank, T. E. Dawson, A. G. Merschel, and C. J. Still. 2022. Changes in tree drought sensitivity provided early warning signals to the California drought and forest mortality event. Global Change Biology 28:1119–1132.

Knowles, N., Dettinger, M. D., & Cayan, D. R. (2006). *Trends in Snowfall versus Rainfall in the Western United States*.

LaMarche, V.C., 1974, Paleoclimatic inferences from long tree-ring records: Intersite comparison shows climatic anomalies that may be linked to features of the general circulation: Science, v. 183, no. 4129, p. 1043{1048.

Larsson, LA., 2014, Coorecorder and cdendro programs of the coorecorder/cdendro package version 7.7: www.cybis/se/furfun/dendro.

Lavender, D. P., & Hermann, R. K. (2014). Douglas-fir: the genus Pseudotsuga.

Leibowitz, S. G., Comeleo, R. L., Wigington Jr, P. J., Weaver, C. P., Morefield, P. E., Sproles, E. A., & Ebersole, J. L. (2014). Hydrologic landscape classification evaluates streamflow vulnerability to climate change in Oregon, USA. *Hydrology and Earth System Sciences*, *18*(9), 3367-3392.

Littell, J. S., Peterson, D. L., & Tjoelker, M. (2008). Douglas-fir growth in mountain ecosystems: water limits tree growth from stand to region. *Ecological Monographs*, *78*(3), 349-368.

Livneh, B., & Badger, A. M. (2020). Drought less predictable under declining future snowpack. *Nature Climate Change*, *10*(5), 452-458.

Maloszewski, P., W. Stichler, and A. Zuber (2004), Interpretation of envir- onmental tracers in groundwater systems with stagnant water zones, Isotopes Environ. Health Stud., 40, 21–33.

Manga, M. (1996). Hydrology of spring-dominated streams in the Oregon Cascades. *Water Resources Research*, *32*(8), 2435-2439.

Mantua, N. J., & Hare, S. R. (2002). The Pacific Decadal Oscillation. *Journal of Oceanography*, *58*(1), 35–44. https://doi.org/10.1023/A:1015820616384

Marshall, A. M., Abatzoglou, J. T., Link, T. E., & Tennant, C. J. (2019). Projected changes in interannual variability of peak snowpack amount and timing in the Western United States. *Geophysical Research Letters*, *46*(15), 8882-8892.

Mass, C. F., Salathé Jr, E. P., Steed, R., & Baars, J. (2022). The Mesoscale Response to Global Warming over the Pacific Northwest Evaluated Using a Regional Climate Model Ensemble. *Journal of Climate*, *35*(6), 2035-2053.

Mazor, E., and R. Nativ (1992), Hydraulic calculation of groundwater flow velocity and age: Examination of the basic premises, Hydrol, J., 138, 211 – 222.

Milly, P.C., Betancourt, J., Falkenmark,M., Hirsch, R.M., Kundzewicz, Z.W., Lettenmaier, D.P., and Stouffer, R.J., 2008, Stationarity is dead: Whither water management?: Science, v. 319, no. 5863, p. 573–574.

Meko, D.M., and Woodhouse, C.A., 2011, Dendroclimatology: progress and prospects, chap. Application of streamflow reconstruction to water resources management, Springer Netherlands, p. 231–261.

McCarthy, K.A., and Alvarez, D.A., 2014, Time-integrated passive sampling as a complement to conventional point in-time sampling for investigating drinking-

water quality, McKenzie River Basin, Oregon, 2007 and 2010–11: U.S. Geological Survey Scientific Investigations Report 2013–5215, 14 p., http://dx.doi.org/10.3133/sir20135215.

Meko, D. M., & Baisan, C. H. (2001). Pilot study of latewood-width of conifers as an indicator of variability of summer rainfall in the North American monsoon region. *International Journal of Climatology: A Journal of the Royal Meteorological Society*, *21*(6), 697-708.

Meko, D.M., Touchan, R., and Anchukaitis, K.J., 2011, Seascorr: A MATLAB program for identifying the seasonal climate signal in an annual tree-ring time series: Computers & Geosciences, v. 37, no. 9, p. 1234{1241.

Mote, P., Hamlet, A., & Salathé, E. (2008). Has spring snowpack declined in the Washington Cascades? *Hydrology and Earth System Sciences*, *12*(1), 193–206. https://doi.org/10.5194/hess- 12-193-2008

Mote, P. W. (2006). Climate-Driven Variability and Trends in Mountain Snowpack in Western North America. *Journal of Climate*, *19*(23), 6209–6220. https://doi.org/10.1175/JCLI3971.1

Mote, P. W., Hamlet, A. F., Clark, M. P., & Lettenmaier, D. P. (2005). DECLINING MOUNTAIN SNOWPACK IN WESTERN NORTH AMERICA*. *Bulletin of the American Meteorological Society*, *86*(1), 39–50. https://doi.org/10.1175/BAMS-86-1-39

Mote, P. W., Li, S., Lettenmaier, D. P., Xiao, M., & Engel, R. (2018). Dramatic declines in snowpack in the western US. *Npj Climate and Atmospheric Science*, *1*(1), 1–6. https://doi.org/10.1038/s41612-018-0012-1

NOAA (2023). Pacific Decadal Oscillation (PDO) | National Centers for Environmental Information (NCEI). Pacific Decadal Oscillation (PDO) | National Centers for Environmental Information (NCEI). https://www.ncei.noaa.gov/access/monitoring/pdo/

Nolin, A. W., & Daly, C. (2006). Mapping "at risk" snow in the Pacific Northwest. *Journal of Hydrometeorology*, *7*(5). https://doi.org/10.1175/JHM543.1

Natural Resources Conservation Service, 2021, National water and climate center: https://www.wcc.nrcs.usda.gov/snow

Leung, L. R., Qian, Y., Bian, X., Washington, W. M., Han, J., & Roads, J. O. (2004). Mid-century ensemble regional climate change scenarios for the western United States. *Climatic Change*, *62*, 75-113.

Pacific Northwest Ecosystem Research Consortium [PNWERC]. 2002. Willamette River Basin planning atlas: trajectories of environmental and ecological change. Corvallis, OR: Oregon State University Press, 178 p.

Pederson, G. T., Gray, S. T., Woodhouse, C. A., Betancourt, J. L., Fagre, D. B., Littell, J. S., ... & Graumlich, L. J. (2011). The unusual nature of recent snowpack declines in the North American Cordillera. *science*, *333*(6040), 332-335.

Percival, D. B., & Constantine, W. L. (2006). Exact simulation of Gaussian time series from nonparametric spectral estimates with application to bootstrapping. *Statistics and Computing*, *16*, 25-35.

Peterson, D. W., & Peterson, D. L. (2001). Mountain hemlock growth responds to climatic variability at annual and decadal time scales. *Ecology*, *82*(12), 3330-3345.

Peterson, D. W., Peterson, D. L., & Ettl, G. J. (2002). Growth responses of subalpine fir to climatic variability in the Pacific Northwest. *Canadian Journal of Forest Research*, *32*(9), 1503-1517.

Pisani, D. J. (2002). *Water and American government: The Reclamation Bureau, national water policy, and the West, 1902-1935*. Univ of California Press.

Poage, N., P. Weisberg, and P. Impara. 2009. Influences of climate, fire, and topography on contemporary age structure patterns of Douglas- …. Canadian Journal of Forest Research 39:1518–1530.

Pohl, K. A., Hadley, K. S., & Arabas, K. B. (2002). A 545-year drought reconstruction for central Oregon. *Physical Geography*, *23*(4), 302-320.

Praskievicz, S., & Chang, H. (2009). Winter precipitation intensity and ENSO/PDO variability in the Willamette Valley of Oregon. *International Journal of Climatology: A Journal of the Royal Meteorological Society*, *29*(13), 2033-2039.

PRISM Climate Group, Oregon State University, https://prism.oregonstate.edu, data created 4 Feb 2014, accessed 16 Dec 2020.

R Core Team (2022). R: A language and environment for statistical computing. R Foundation for Statistical Computing, Vienna, Austria. URL https://www.R-project.org/.

Ratcliff, C. J., Voelker, S. L., & Nolin, A. W. (2018). Tree-ring carbon isotope records from the western Oregon Cascade Mountains primarily record summer maximum temperatures. *Tree-ring research*, *74*(2), 185-195.

Restaino, C. M., Peterson, D. L., & Littell, J. (2016). Increased water deficit decreases Douglas fir growth throughout western US forests. *Proceedings of the National academy of Sciences*, *113*(34), 9557-9562.

Segura, C., Noone, D., Warren, D., Jones, J. A., Tenny, J., & Ganio, L. M. (2019). Climate, Landforms, and Geology Affect Baseflow Sources in a Mountain Catchment. *Water Resources Research*, *55*(7). https://doi.org/10.1029/2018WR023551

Seber, G. A., & Lee, A. J. (2003). *Linear regression analysis* (Vol. 330). John Wiley & Sons.

Siler, Nicholas, Cristian Proistosescu, and Stephen Po-Chedley. "Natural variability has slowed the decline in western US snowpack since the 1980s." *Geophysical Research Letters* 46.1 (2019): 346-355.

Speer, J.H., 2010, Fundamentals of tree-ring research: University of Arizona Press.

Sproles, E. A., Roth, T. R., & Nolin, A. W. (2017). Future snow? A spatial-probabilistic assessment of the extraordinarily low snowpacks of 2014 and 2015 in the Oregon Cascades. *Cryosphere*, *11*(1). https://doi.org/10.5194/tc-11-331-2017

Stahle, D. W., Cleaveland, M. K., Grissino-Mayer, H. D., Griffin, R. D., Fye, F. K., Therrell, M. D., & Villanueva Diaz, J. (2009). Cool-and warm-season precipitation reconstructions over western New Mexico. *Journal of Climate*, *22*(13), 3729-3750.

Stearns, H. T. (1929). *Geology and water resources of the Upper McKenzie Valley, Oregon*. US Government Printing Office.

Stewart, I. T., Cayan, D. R., & Dettinger, M. D. (2005). *Changes toward Earlier Streamflow Timing across Western North America*. http://tao.

Stokes, M., and Smiley, T., 1968, An introduction to tree-ring dating: Chicago, IL, University of Chicago Press.

Stokes, M.A., 1996, An introduction to tree-ring dating: University of Arizona Press.

Sturm, M., Holmgren, J., & Liston, G. E. (1995). A Seasonal Snow Cover Classification System for Local to Global Applications, Journal of Climate, 8(5), 1261-1283. Retrieved May 10, 2022, from https://journals.ametsoc.org/view/journals/clim/8/5/1520-0442_1995_008_1261_asscs_2_0_co_2.xml

Schweingruber, F. H. 1996. Tree rings and environment: dendroecology. Paul Haupt Verlag, Bern, Switzerland.

Tague, C., & Grant, G. E. (2004). A geological framework for interpreting the low-flow regimes of Cascade streams, Willamette River Basin, Oregon. *Water Resources Research*, *40*(4). https://doi.org/10.1029/2003WR002629

Tague, C. L., Choate, J. S., & Grant, G. (2013). Parameterizing sub-surface drainage with geology to improve modeling streamflow responses to climate in data limited environments. *Hydrology and Earth System Sciences*, *17*(1). https://doi.org/10.5194/hess-17-341-2013

Tague, C., Valentine, S., & Kotchen, M. (2008). Effect of geomorphic channel restoration on streamflow and groundwater in a snowmelt-dominated watershed. *Water Resources Research*, *44*(10). https://doi.org/10.1029/2007WR006418

Tepley, A. J., F. J. Swanson, and T. A. Spies. 2013. Fire-mediated pathways of stand development in Douglas-fir/ western hemlock forests of the Pacific Northwest, USA. Ecology 94:1729–43.

Torbenson, Stahle, D. W., Villanueva Díaz, J., Cook, E. R., & Griffin, D. (2016). The Relationship Between Earlywood and Latewood Ring-Growth Across North America. *Tree-Ring Research*, *72*(2), 53–66. https://doi.org/10.3959/1536-1098-72.02.53

U.S. Census Bureau. (2021). *Eugene Population Estimates*, 2017 – 2021 American Community Survey 5-year estimates. Retrieved from https://www.census.gov/quickfacts/eugenecityoregon

Weisberg, P. J., and F. J. Swanson. 2003. Regional synchroneity in fire regimes of western Oregon and Washington, USA. Forest Ecology and Management 172:17–28.

Wigley, T.M., Briffa, K.R., and Jones, P.D., 1984, On the average value of correlated time series, with applications in dendroclimatology and hydrometeorology: Journal of climate and AppliedMeteorology, v. 23, no. 2, p. 201–213.

Yamashita, T., Yamashita, K., & Kamimura, R. (2007). A stepwise AIC method for variable selection in linear regression. Communications in Statistics—Theory and Methods, 36(13), 2395-2403.

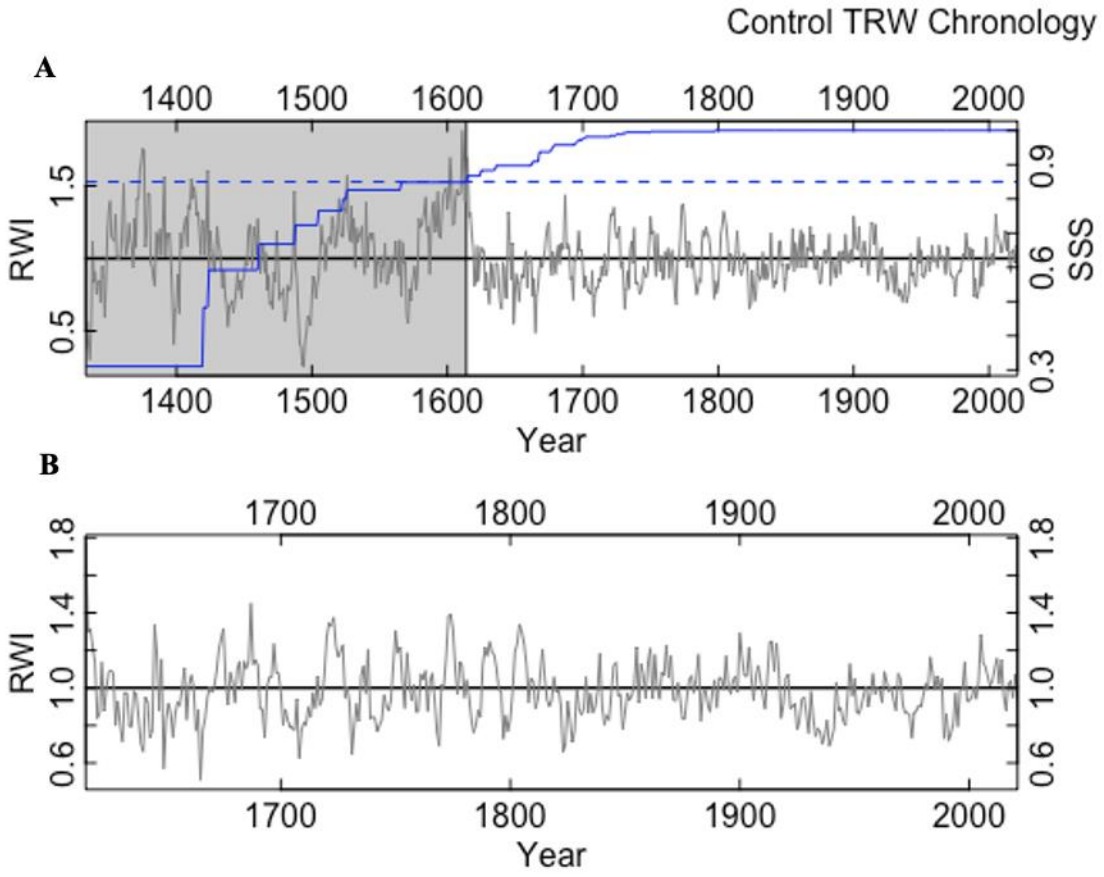

Figure A.1. The top panel (A) displays the detrended control total ring width (TRW) standard chronology with years along the x-axis and unitless ring width indices (RWI) along the y-axis. The grey shaded box illustrates the sub-sample strength (SSS) cut-off point where the blue line falls below the dashed blue line 0.85 SSS threshold. The bottom panel (B) displays the detrended SSS-truncated chronology.

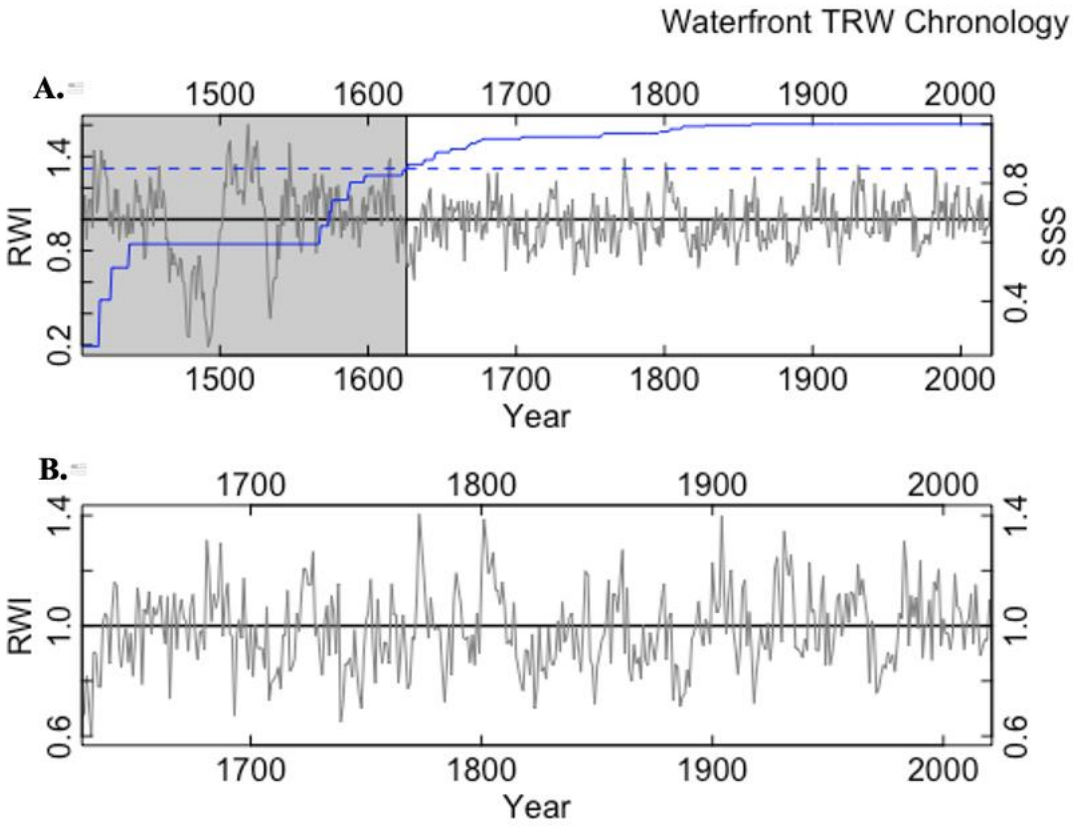

Figure A.2. The top panel (A) displays the detrended waterfront total ring width (TRW) standard chronology with years along the x-axis and unitless ring width indices (RWI) along the y-axis. The grey shaded box illustrates the sub-sample strength (SSS) cut-off point where the blue line falls below the dashed blue line 0.85 SSS threshold. The bottom panel (B) displays the detrended SSS-truncated chronology.

Table A.1. Descriptive statistics for monthly hydroclimate parameters including mean air temperature and total precipitation from PRISM, gridded at the $4k^2$ spatial resolution (PRISM Climate Group, 2014), total SWE from TerraClimate (Abatzoglou, 2018), and mean gauge height from USGS (USGS, 2014).

Variables	**Min.**	**1st Qu.**	**Median**	**Mean**	**3rd Qu.**	**Max.**
SWE (mm)	0.00	0.00	0.716	111.55	163.72	1097.76
Air Temperature (°C)	-7.70	1.80	6.90	7.23	12.70	19.60
Precipitation (mm)	0.01	58.47	140.87	176.97	259.97	885.40
Gauge (in)	0.01	1.750	2.25	2.30	2.86	4.58

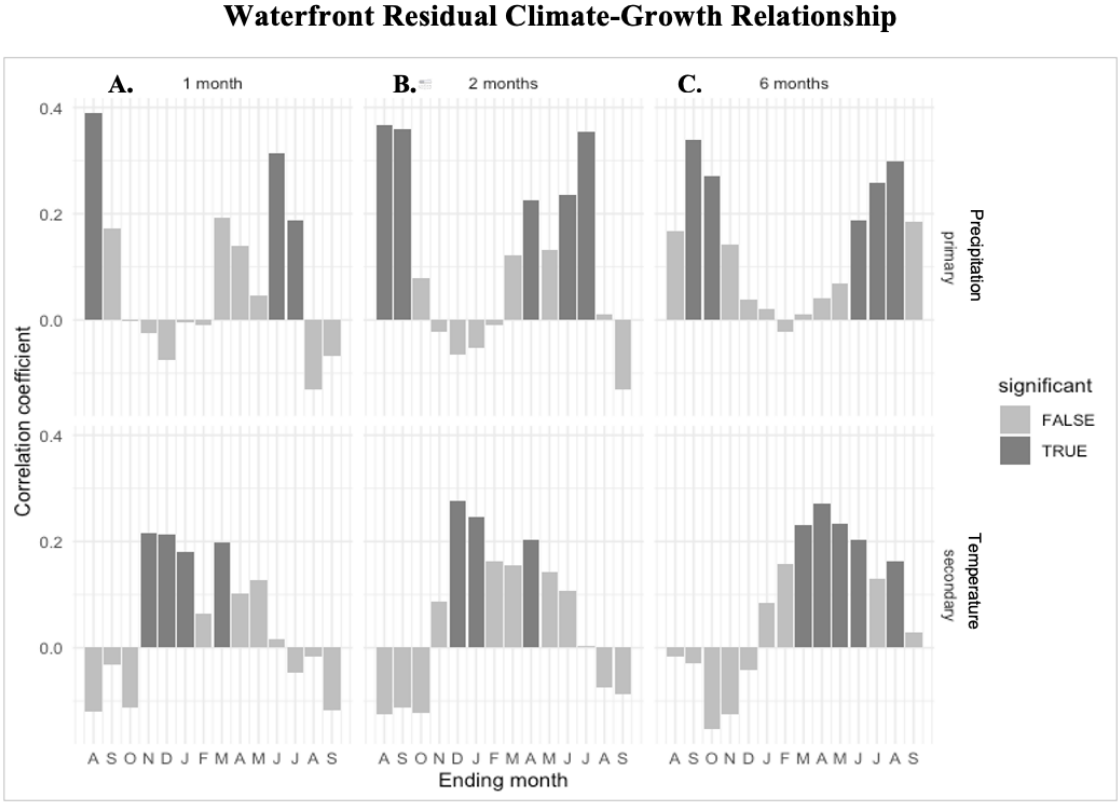

Figure A.3. Monthly and seasonalized correlation function coefficients between the Douglas-fir (*Pseudotsuga menziesii*) total ring width waterfront residual chronology and monthly total precipitation (top panels) and monthly average air temperature (bottom panels). On the x-axis (Ending months), the first letter to the left of each panel (A) refers to August of the previous growth year, and the last letter to each panel's right (S) refers to September of the concurrent growth year. Dark bars represent significant correlations ($p < 0.05$) for 1- month (A), 2- month (B), and 6- months (C) with total precipitation (primary correlation) and mean air temperature (secondary/partial-correlation). The 2- and 6-months aggregated values reflect the last month of the aggregation; e.g., F in the 2-month top panel equals the growth response to the total precipitation during January and February of the growing year. Monthly climate parameters, gridded at the $4k^2$ spatial resolution, were obtained from PRISM (PRISM Climate Group, 2014) and correlation coefficients are for the 1895-2021 period.

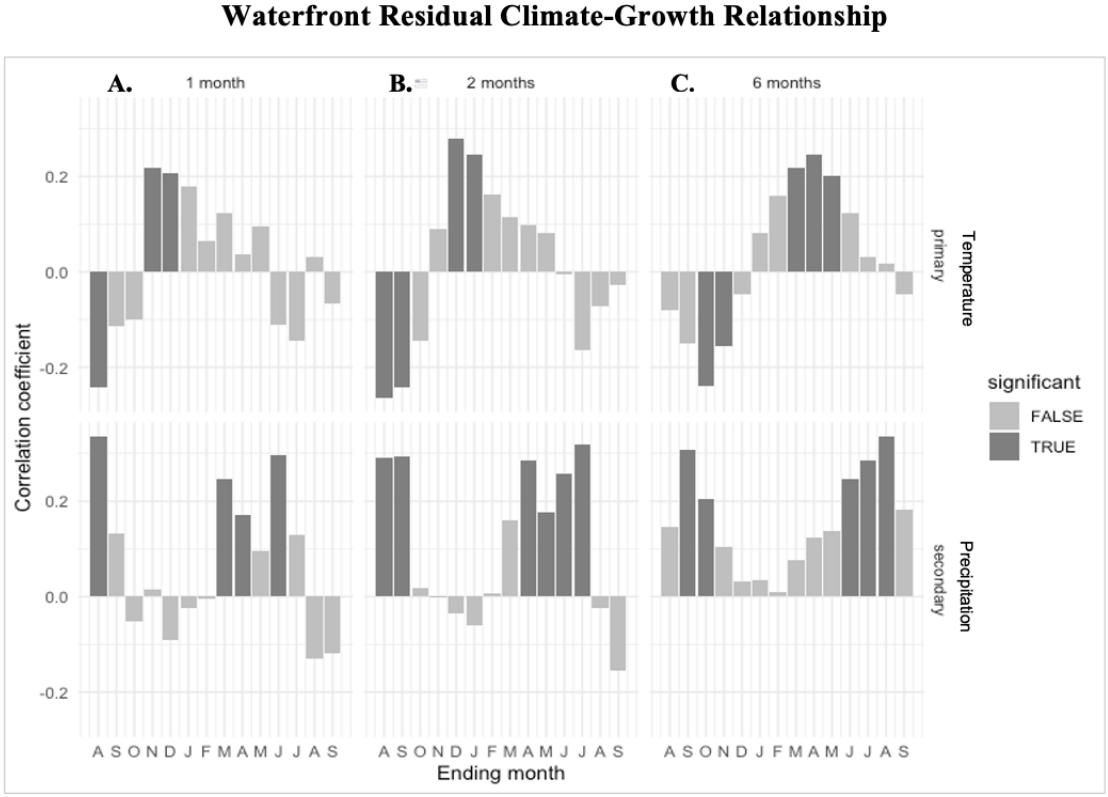

Figure A.4. Monthly and seasonalized correlation function coefficients between the Douglas-fir (*Pseudotsuga menziesii*) total ring width waterfront residual chronology and mean monthly air temperature (top panels) and monthly total precipitation (bottom panels). On the x-axis (Ending months), the first letter to the left of each panel (A) refers to August of the previous growth year, and the last letter to each panel's right (S) refers to September of the concurrent growth year. Dark bars represent significant correlations ($p < 0.05$) for 1- month (A), 2- month (B), and 6- months (C) with mean air temperature (primary correlation) and total precipitation (secondary/partial-correlation). The 2- and 6-months aggregated values reflect the last month of the aggregation. Monthly climate parameters, gridded at the $4k^2$ spatial resolution, were obtained from PRISM (PRISM Climate Group, 2014) and correlation coefficients are for the 1895-2021 period.

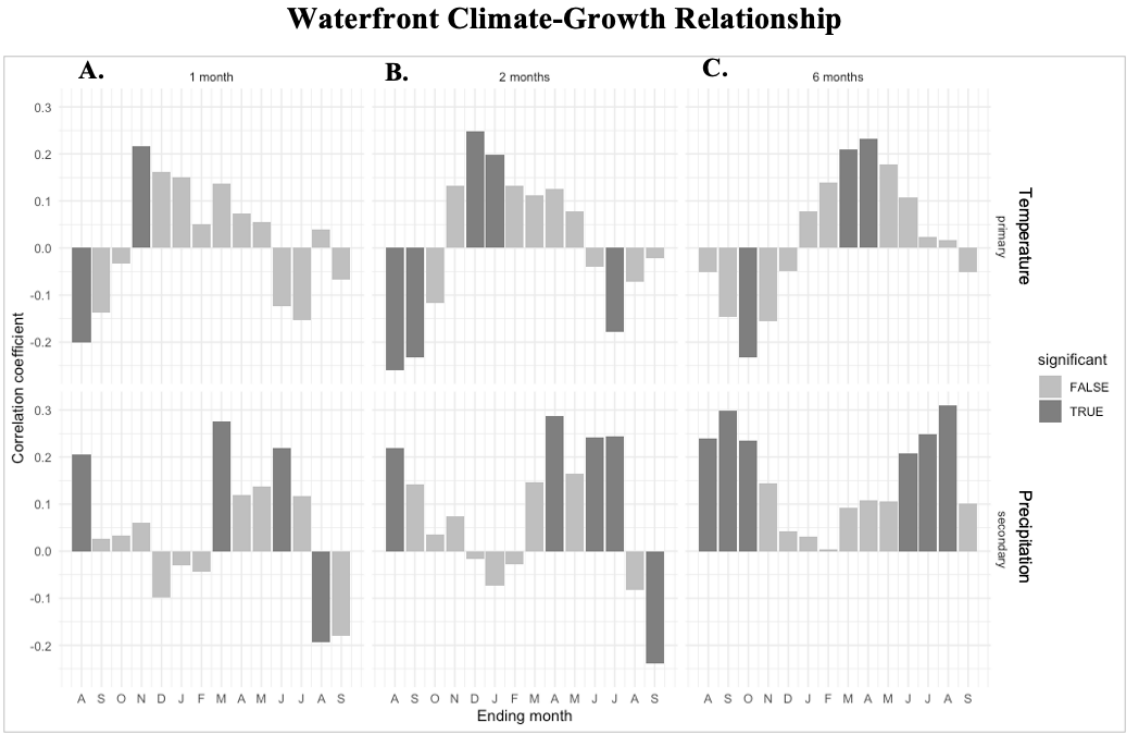

Figure A.5. Monthly and seasonalized correlation function coefficients between the Douglas-fir (*Pseudotsuga menziesii*) total ring width chronology at the waterfront and mean air temperature (top panels) and total monthly precipitation (bottom panels). On the x-axis (Ending months), the first letter to the left of each panel (A) refers to August of the previous growth year, and the last letter to each panel's right (S) refers to September of the concurrent growth year. Dark bars represent significant correlations ($p < 0.05$) for 1-month (A), 2- month (B), and 6- months (C) with monthly mean air temperature (primary correlation) and monthly total precipitation (secondary/partial-correlation). The 2- and 6-months aggregated values reflect the last month of the aggregation. Monthly climate parameters, gridded at the $4k^2$ spatial resolution, were obtained from PRISM (PRISM Climate Group, 2014) and correlation coefficients are for the 1895-2021 period.

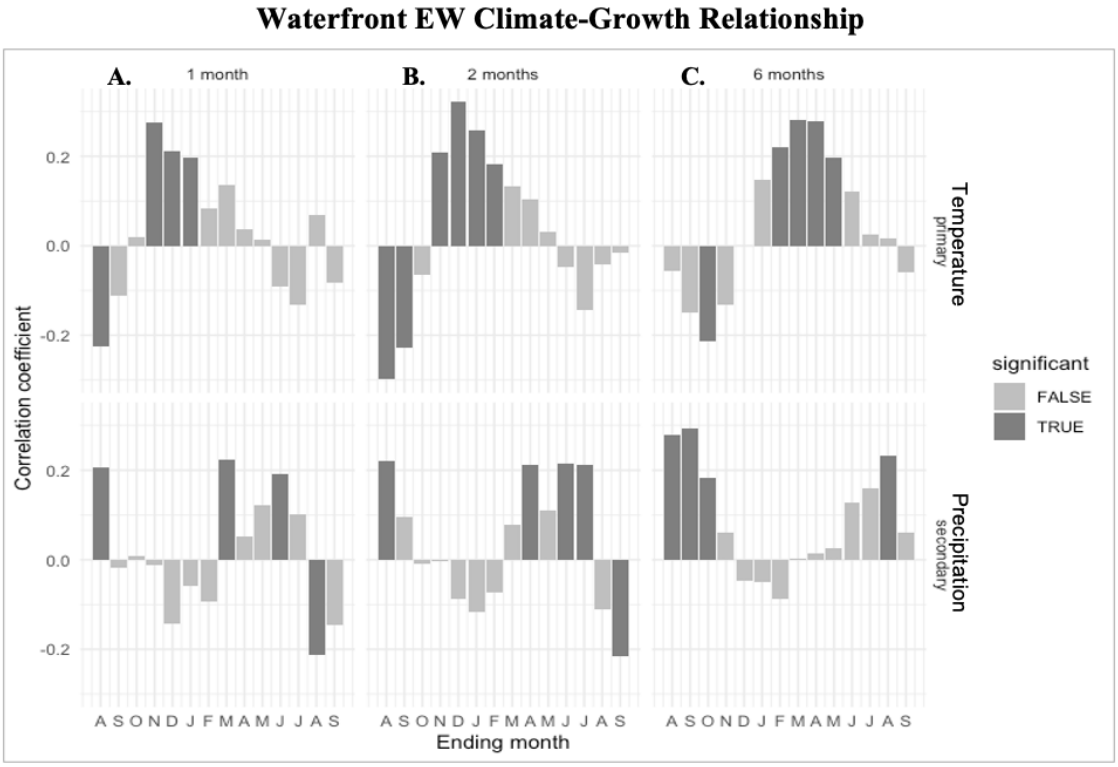

Figure A.6. Monthly and seasonalized correlation function coefficients between the Douglas-fir (*Pseudotsuga menziesii*) earlywood (EW) waterfront chronology and mean monthly air temperature (top panels) and monthly total precipitation (bottom panels). On the x-axis (Ending months), the first letter to the left of each panel (A) refers to August of the previous growth year, and the last letter to each panel's right (S) refers to September of the concurrent growth year. Dark bars represent significant correlations ($p < 0.05$) for 1- month (A), 2- month (B), and 6- months (C) with mean air temperature (primary correlation) and total precipitation (secondary/partial-correlation). The 2- and 6-months aggregated values reflect the last month of the aggregation. Monthly climate parameters, gridded at the $4k^2$ spatial resolution, were obtained from PRISM (PRISM Climate Group, 2014) and correlation coefficients are for the 1895-2021 period.

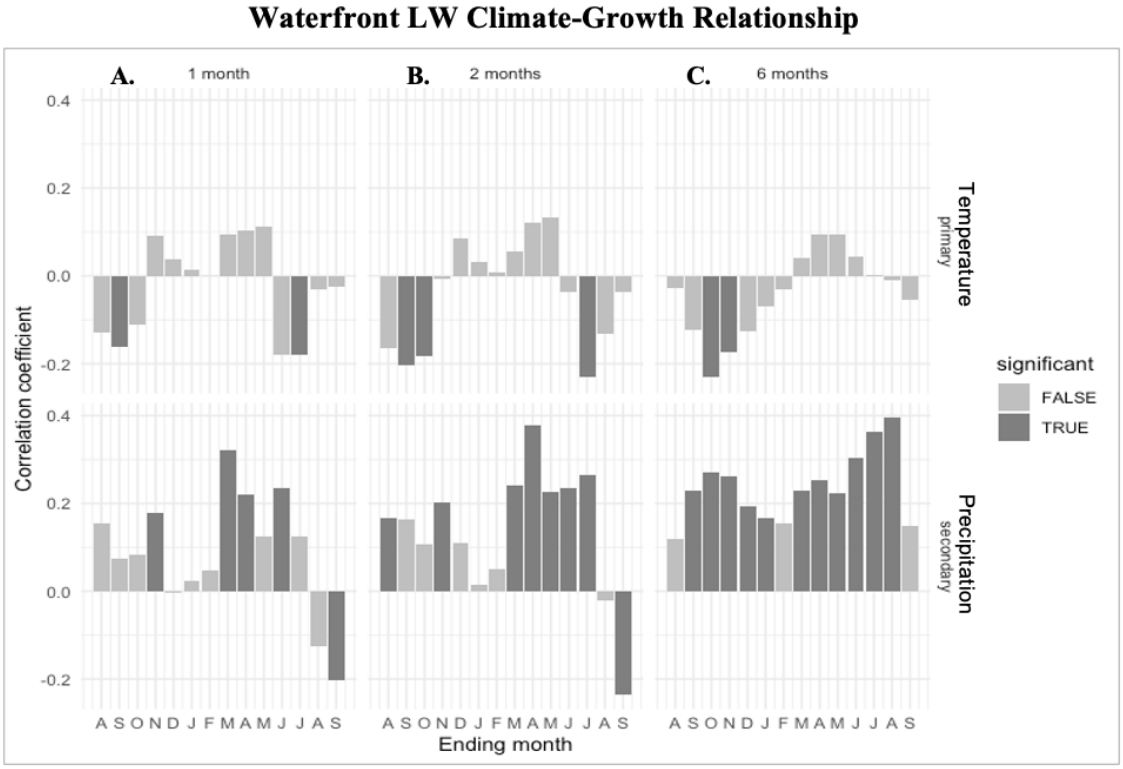

Figure A.7. Monthly and seasonalized correlation function coefficients between the Douglas-fir (*Pseudotsuga menziesii*) latewood (LW) chronology at the waterfront and monthly mean air temperature (top panels) and monthly total precipitation (bottom panels). On the x-axis (Ending months), the first letter to the left of each panel (A) refers to August of the previous growth year, and the last letter to each panel's right (S) refers to September of the concurrent growth year. Dark bars represent significant correlations ($p < 0.05$) for 1- month (A), 2- month (B), and 6- months (C) with mean air temperature (primary correlation) and total precipitation (secondary/partial-correlation). The 2- and 6-months aggregated values reflect the last month of the aggregation. Monthly climate parameters, gridded at the $4k^2$ spatial resolution, were obtained from PRISM (PRISM Climate Group, 2014) and correlation coefficients are for the 1895-2021 period.

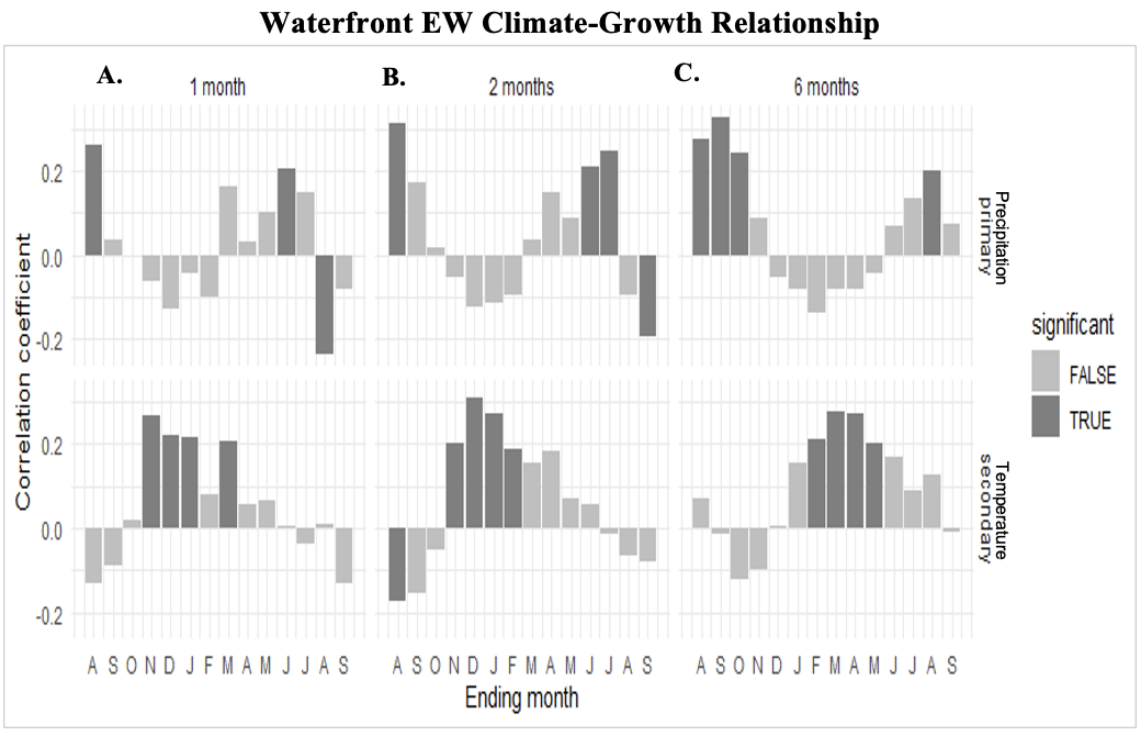

Figure A.8. Monthly and seasonalized correlation function coefficients between the Douglas-fir (*Pseudotsuga menziesii*) earlywood (EW) chronology at the waterfront and monthly total precipitation (top panels) and monthly mean air temperature (bottom panels). On the x-axis (Ending months), the first letter to the left of each panel (A) refers to August of the previous growth year, and the last letter to each panel's right (S) refers to September of the concurrent growth year. Dark bars represent significant correlations ($p < 0.05$) for 1- month (A), 2- month (B), and 6- months (C) with total precipitation (primary correlation) and mean air temperature (secondary/partial-correlation). The 2- and 6-months aggregated values reflect the last month of the aggregation. Monthly climate parameters, gridded at the $4k^2$ spatial resolution, were obtained from PRISM (PRISM Climate Group, 2014) and correlation coefficients are for the 1895-2021 period.

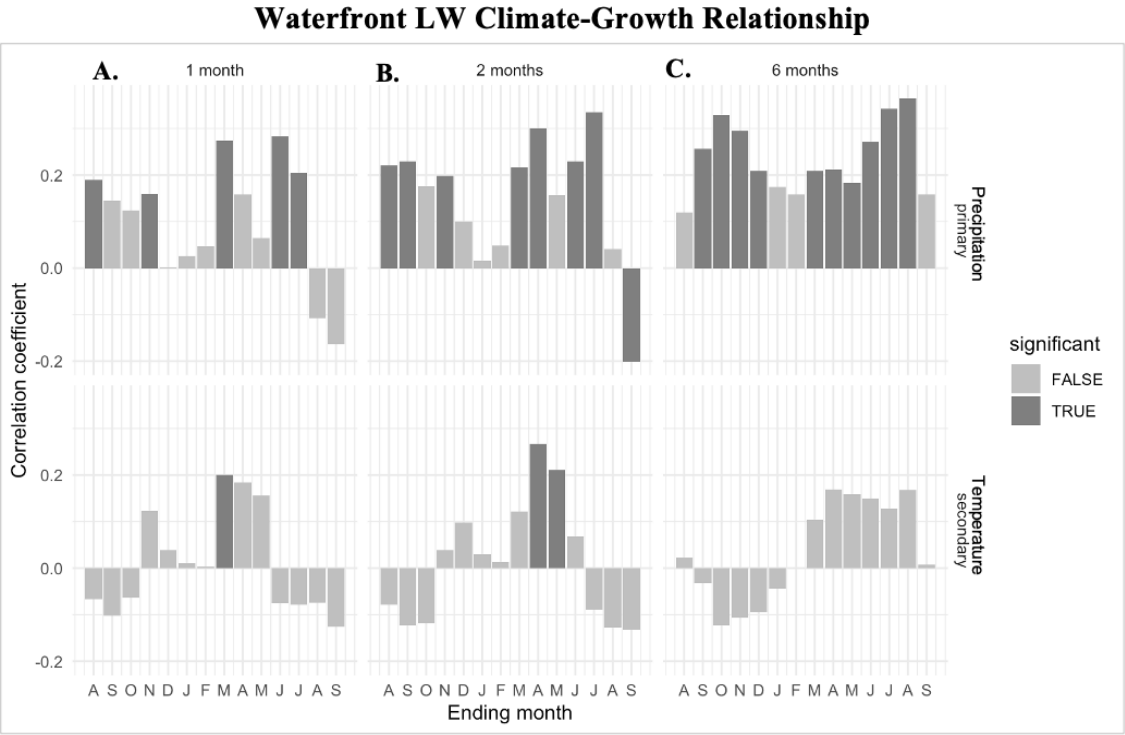

Figure A.9. Monthly and seasonalized correlation function coefficients between the Douglas-fir (*Pseudotsuga menziesii*) latewood (LW) chronology at the waterfront and monthly total precipitation (top panels) and monthly mean air temperature (bottom panels). On the x-axis (Ending months), the first letter to the left of each panel (A) refers to August of the previous growth year, and the last letter to each panel's right (S) refers to September of the concurrent growth year. Dark bars represent significant correlations ($p < 0.05$) for 1- month (A), 2- month (B), and 6- months (C) with total precipitation (primary correlation) and mean air temperature (secondary/partial-correlation). The 2- and 6-months aggregated values reflect the last month of the aggregation. Monthly climate parameters, gridded at the $4k^2$ spatial resolution, were obtained from PRISM (PRISM Climate Group, 2014) and correlation coefficients are for the 1895-2021 period.

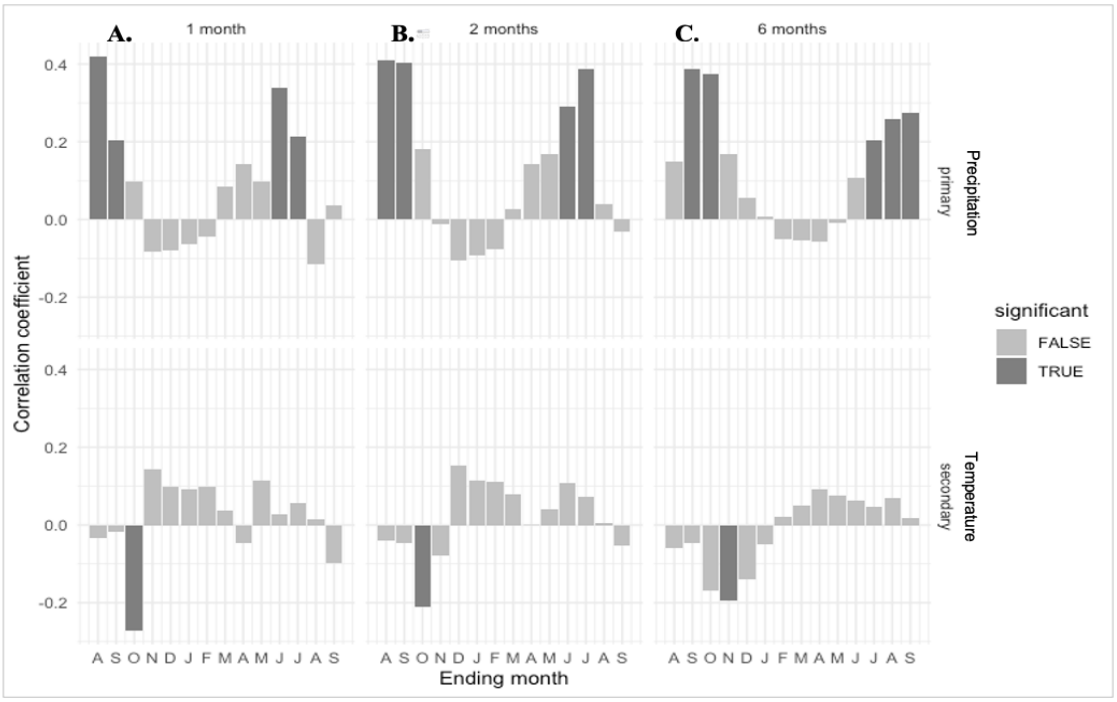

Figure A.10. Monthly and seasonalized correlation function coefficients between the Douglas-fir (*Pseudotsuga menziesii*) total ring width control residual chronology and monthly total precipitation (top panels) and monthly mean air temperature (bottom panels). On the x-axis (Ending months), the first letter to the left of each panel (A) refers to August of the previous growth year, and the last letter to each panel's right (S) refers to September of the concurrent growth year. Dark bars represent significant correlations ($p < 0.05$) for 1- month (A), 2- month (B), and 6- months (C) with total precipitation (primary correlation) and mean air temperature (secondary/partial-correlation). The 2- and 6-months aggregated values reflect the last month of the aggregation. Monthly climate parameters, gridded at the $4k^2$ spatial resolution, were obtained from PRISM (PRISM Climate Group, 2014) and correlation coefficients are for the 1895-2021 period.

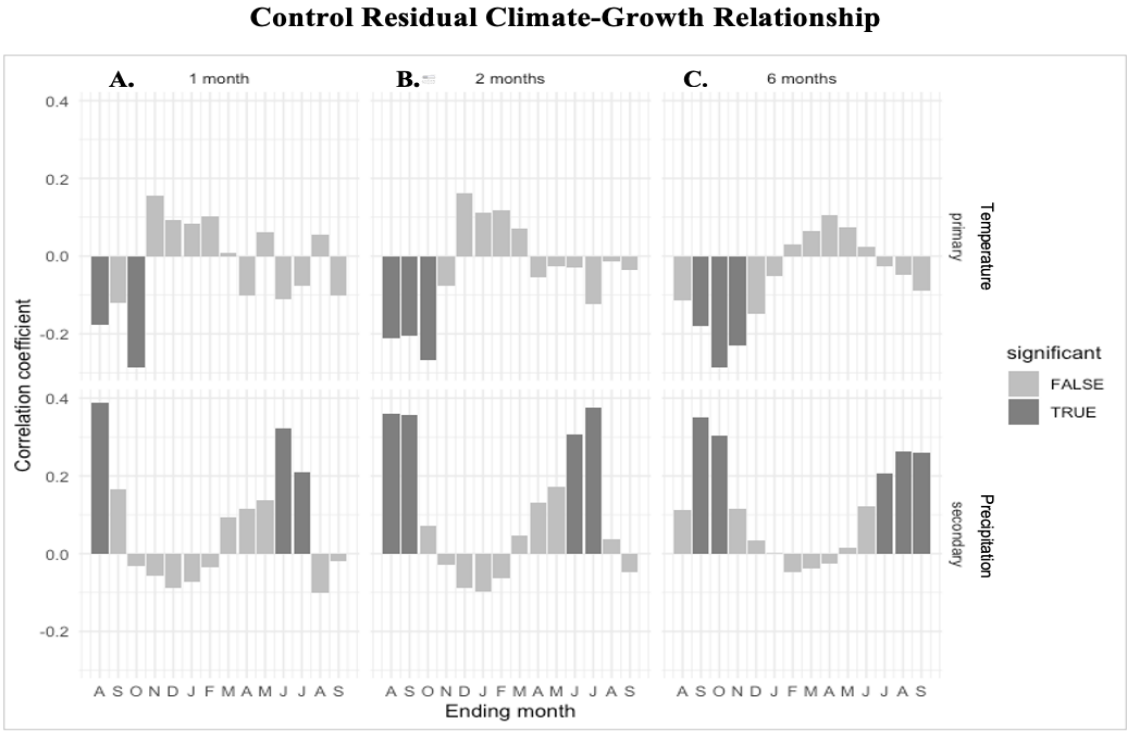

Figure A.11. Monthly and seasonalized correlation function coefficients between the Douglas-fir (*Pseudotsuga menziesii*) total ring width control residual chronology and monthly mean air temperature (top panels) and monthly total precipitation (bottom panels). On the x-axis (Ending months), the first letter to the left of each panel (A) refers to August of the previous growth year, and the last letter to each panel's right (S) refers to September of the concurrent growth year. Dark bars represent significant correlations ($p < 0.05$) for 1- month (A), 2- month (B), and 6- months (C) with mean air temperature (primary correlation) and total precipitation (secondary/partial-correlation). The 2- and 6-months aggregated values reflect the last month of the aggregation. Monthly climate parameters, gridded at the $4k^2$ spatial resolution, were obtained from PRISM (PRISM Climate Group, 2014) and correlation coefficients are for the 1895-2021 period.

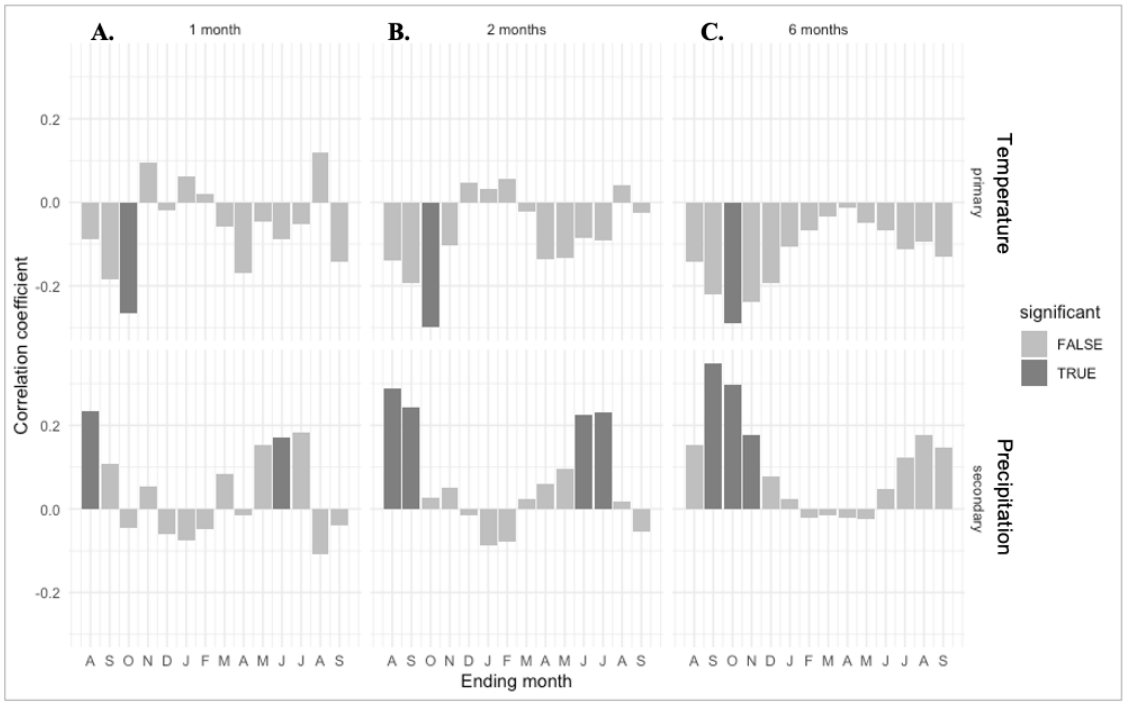

Figure A.12. Monthly and seasonalized correlation function coefficients between the Douglas-fir (*Pseudotsuga menziesii*) total ring width control chronology and monthly mean air temperature (top panels) and monthly total precipitation (bottom panels). On the x-axis (Ending months), the first letter to the left of each panel (A) refers to August of the previous growth year, and the last letter to each panel's right (S) refers to September of the concurrent growth year. Dark bars represent significant correlations ($p < 0.05$) for 1-month (A), 2- month (B), and 6- months (C) with mean air temperature (primary correlation) and total precipitation (secondary/partial-correlation). The 2- and 6-months aggregated values reflect the last month of the aggregation. Monthly climate parameters, gridded at the $4k^2$ spatial resolution, were obtained from PRISM (PRISM Climate Group, 2014) and correlation coefficients are for the 1895-2021 period.

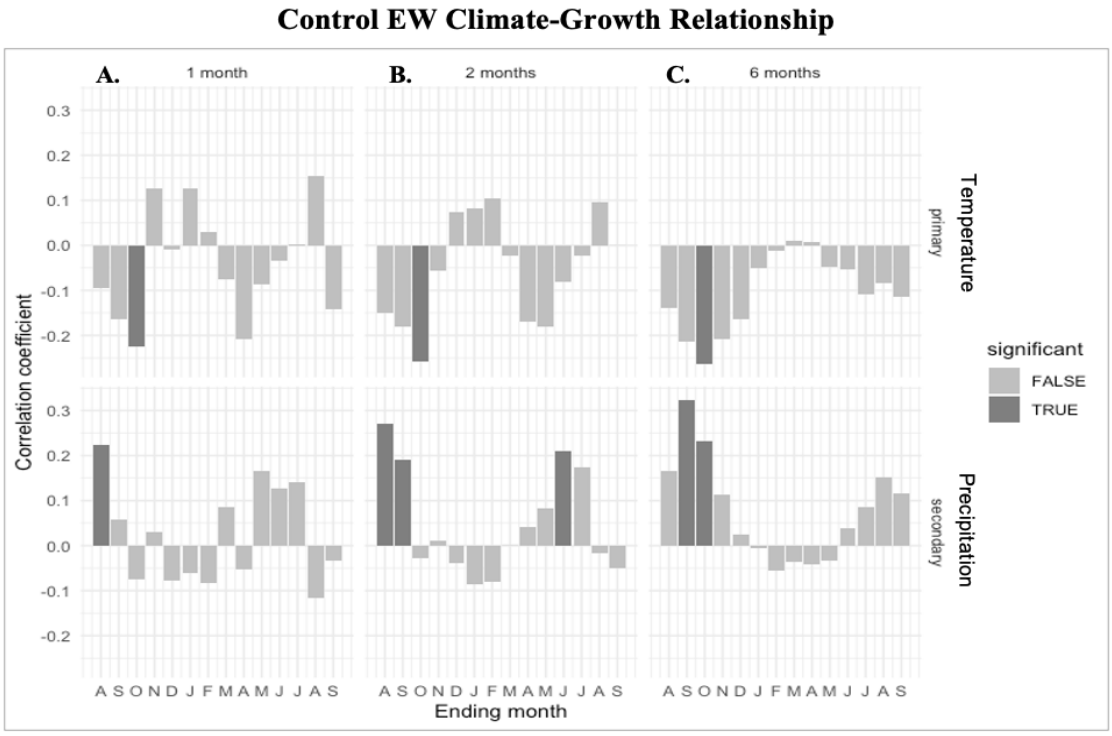

Figure A.13. Monthly and seasonalized correlation function coefficients between the Douglas-fir (*Pseudotsuga menziesii*) earlywood (EW) control chronology and monthly mean air temperature (top panels) and monthly total precipitation (bottom panels). On the x-axis (Ending months), the first letter to the left of each panel (A) refers to August of the previous growth year, and the last letter to each panel's right (S) refers to September of the concurrent growth year. Dark bars represent significant correlations ($p < 0.05$) for 1-month (A), 2- month (B), and 6- months (C) with mean air temperature (primary correlation) and total precipitation (secondary/partial-correlation). The 2- and 6-months aggregated values reflect the last month of the aggregation. Monthly climate parameters, gridded at the $4k^2$ spatial resolution, were obtained from PRISM (PRISM Climate Group, 2014) and correlation coefficients are for the 1895-2021 period.

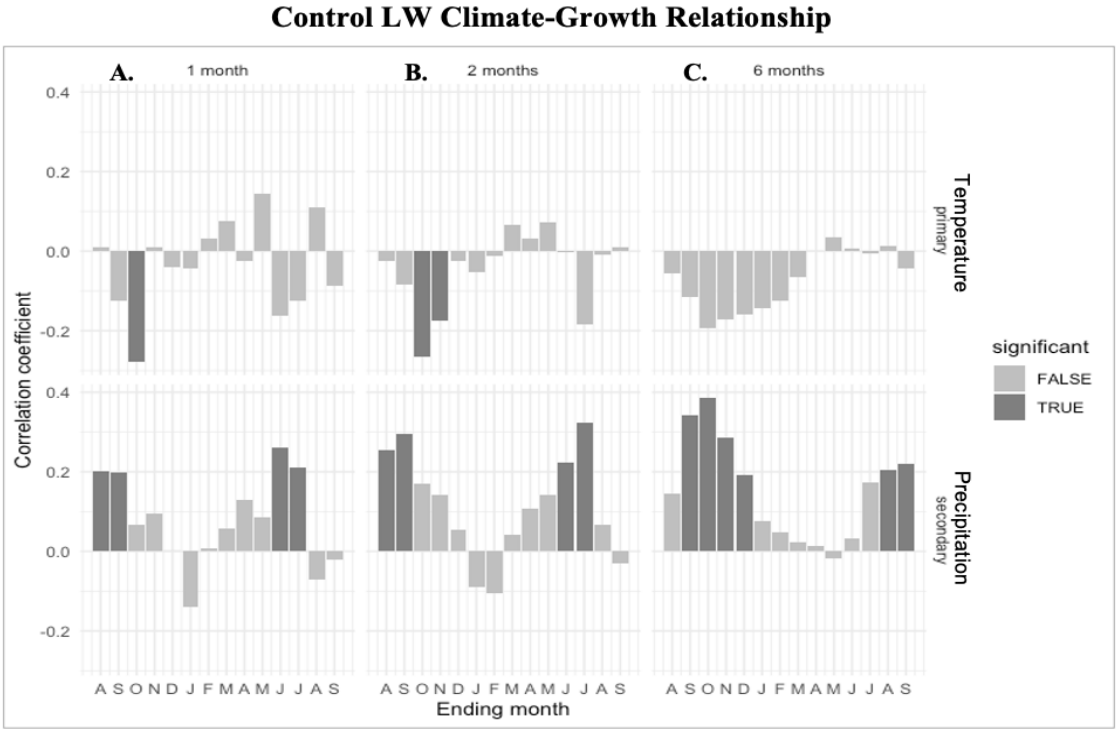

Figure A.14. Monthly and seasonalized correlation function coefficients between the Douglas-fir (*Pseudotsuga menziesii)* latewood (LW) control chronology and monthly mean air temperature (top panels) and monthly total precipitation (bottom panels). On the x-axis (Ending months), the first letter to the left of each panel (A) refers to August of the previous growth year, and the last letter to each panel's right (S) refers to September of the concurrent growth year. Dark bars represent significant correlations ($p < 0.05$) for 1-month (A), 2- month (B), and 6- months (C) with mean air temperature (primary correlation) and total precipitation (secondary/partial-correlation). The 2- and 6-months aggregated values reflect the last month of the aggregation. Monthly climate parameters, gridded at the $4k^2$ spatial resolution, were obtained from PRISM (PRISM Climate Group, 2014) and correlation coefficients are for the 1895-2021 period.

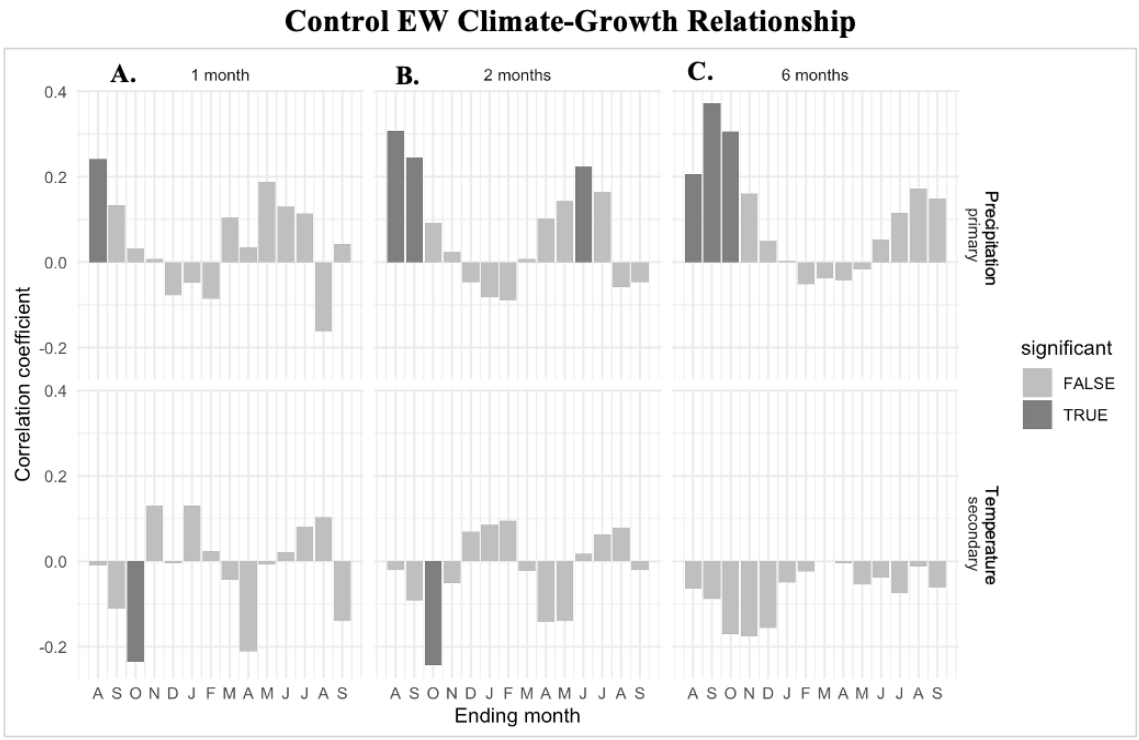

Figure A.15. Monthly and seasonalized correlation function coefficients between the Douglas-fir (*Pseudotsuga menziesii*) earlywood (EW) control chronology and monthly total precipitation (top panels) and monthly mean air temperature (bottom panels). On the x-axis (Ending months), the first letter to the left of each panel (A) refers to August of the previous growth year, and the last letter to each panel's right (S) refers to September of the concurrent growth year. Dark bars represent significant correlations ($p < 0.05$) for 1-month (A), 2- month (B), and 6- months (C) with total precipitation (primary correlation) and mean air temperature (secondary/partial-correlation). The 2- and 6-months aggregated values reflect the last month of the aggregation. Monthly climate parameters, gridded at the $4k^2$ spatial resolution, were obtained from PRISM (PRISM Climate Group, 2014) and correlation coefficients are for the 1895-2021 period.

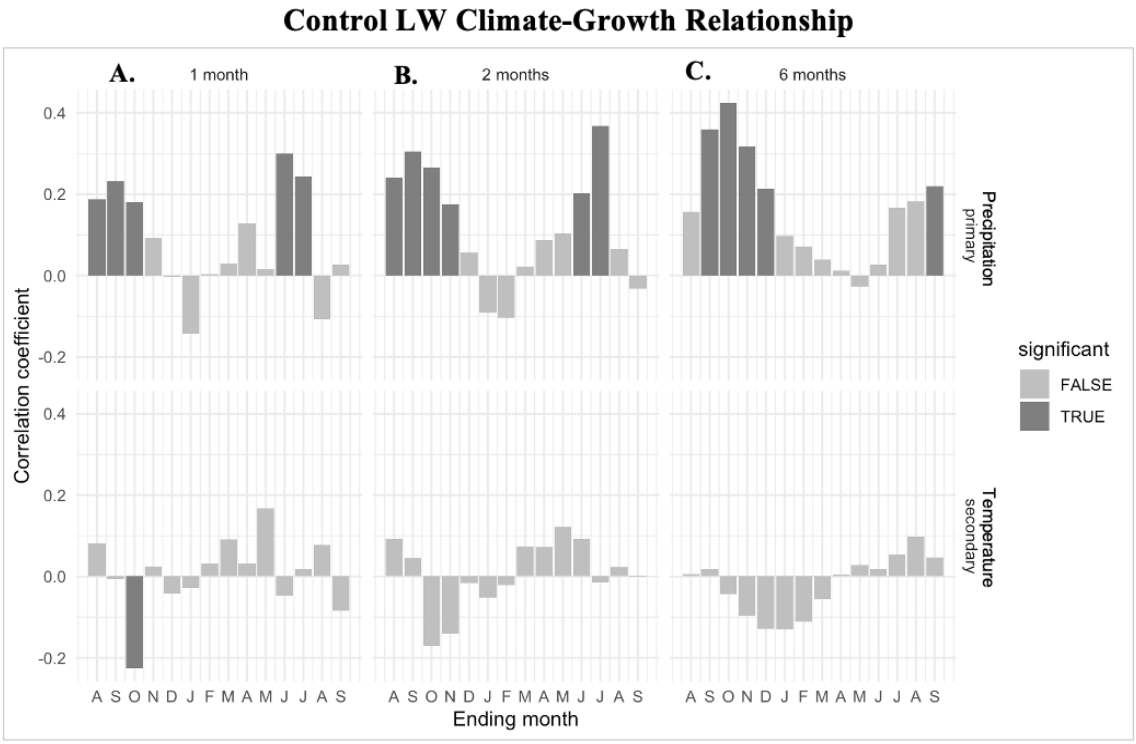

Figure A.16. Monthly and seasonalized correlation function coefficients between the Douglas-fir (*Pseudotsuga menziesii)* latewood (LW) control chronology and monthly total precipitation (top panels) and monthly mean air temperature (bottom panels). On the x-axis (Ending months), the first letter to the left of each panel (A) refers to August of the previous growth year, and the last letter to each panel's right (S) refers to September of the concurrent growth year. Dark bars represent significant correlations ($p < 0.05$) for 1-month (A), 2- month (B), and 6- months (C) with total precipitation (primary correlation) and mean air temperature (secondary/partial-correlation). The 2- and 6-months aggregated values reflect the last month of the aggregation. Monthly climate parameters, gridded at the $4k^2$ spatial resolution, were obtained from PRISM (PRISM Climate Group, 2014) and correlation coefficients are for the 1895-2021 period.

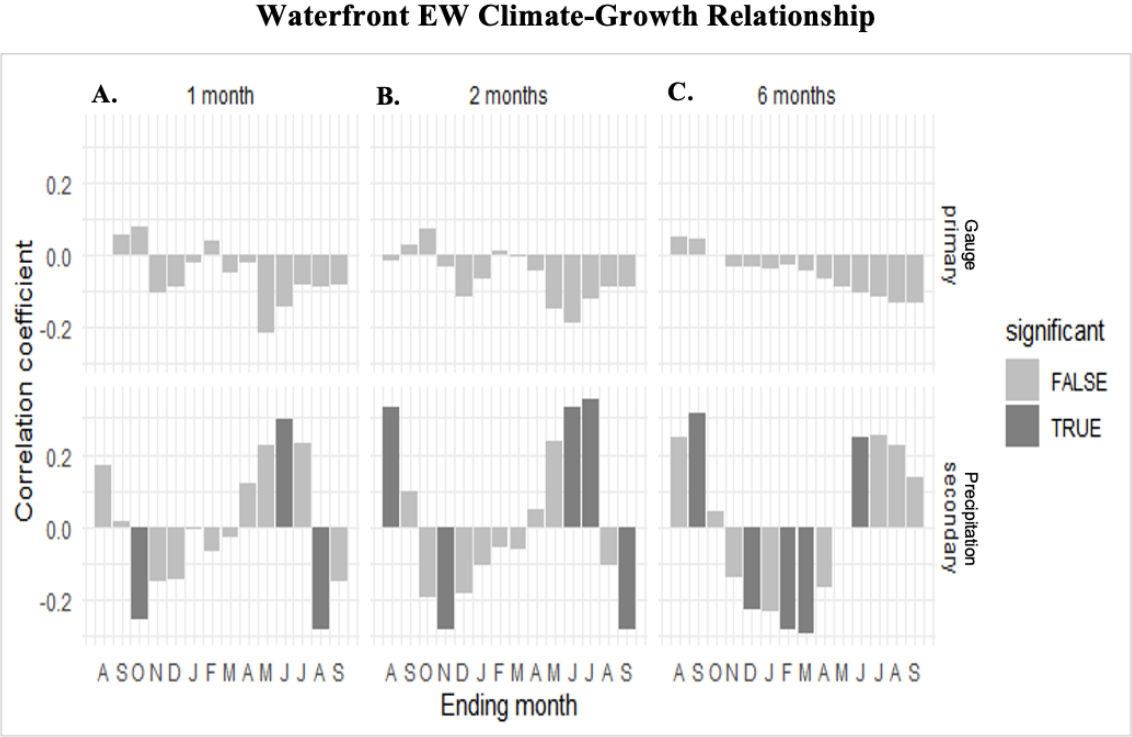

Figure A.17. Monthly and seasonalized correlation function coefficients between the Douglas-fir (*Pseudotsuga menziesii*) earlywood (EW) waterfront chronology and monthly gauge height (top panels) and monthly total precipitation (bottom panels). On the x-axis (Ending months), the first letter to the left of each panel (A) refers to August of the previous growth year, and the last letter to each panel's right (S) refers to September of the concurrent growth year. Dark bars represent significant correlations ($p < 0.05$) for 1- month (A), 2- month (B), and 6- months (C) with gauge height (primary correlation) and total precipitation (secondary/partial-correlation). The 2- and 6-months aggregated values reflect the last month of the aggregation. Monthly total precipitation, gridded at the $4k^2$ spatial resolution, was obtained from PRISM (PRISM Climate Group, 2014), and monthly average gauge height of the McKenzie River at the outlet of Clear Lake was extracted from USGS (USGS, 2021). Correlation coefficients are for the 1959-2021 period.

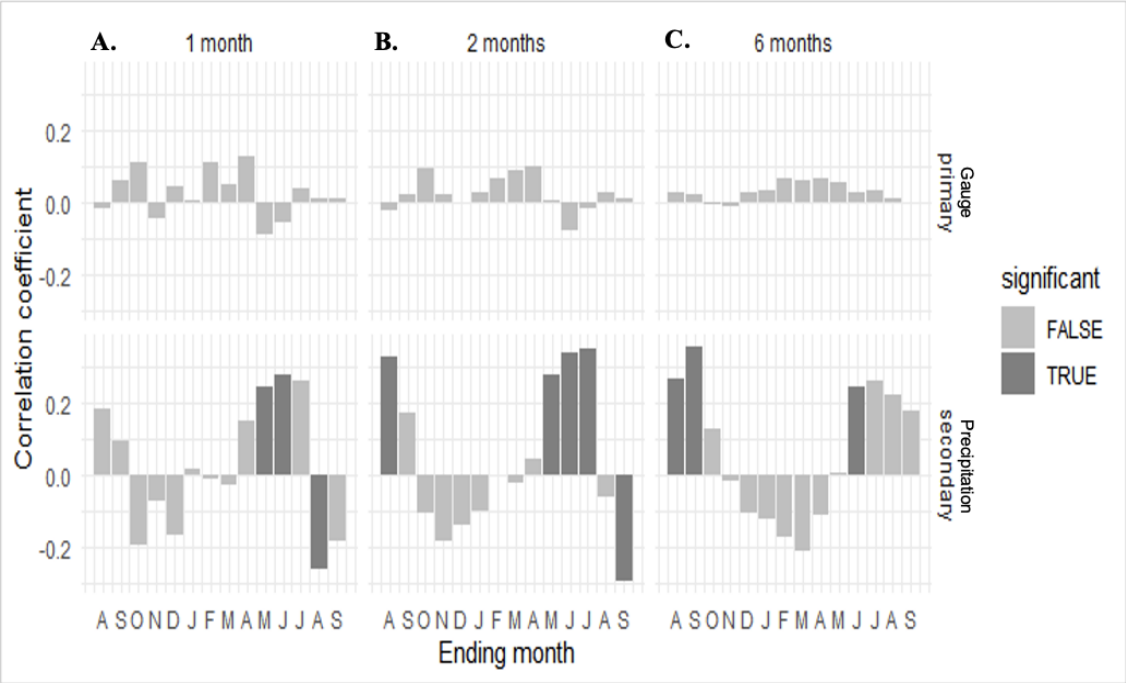

Figure A.18. Monthly and seasonalized correlation function coefficients between the Douglas-fir (*Pseudotsuga menziesii*) total ring width waterfront chronology and monthly gauge height (top panels) and monthly total precipitation (bottom panels). On the x-axis (Ending months), the first letter to the left of each panel (A) refers to August of the previous growth year, and the last letter to each panel's right (S) refers to September of the concurrent growth year. Dark bars represent significant correlations ($p < 0.05$) for 1-month (A), 2- month (B), and 6- months (C) with gauge height (primary correlation) and total precipitation (secondary/partial-correlation). The 2- and 6-months aggregated values reflect the last month of the aggregation. Monthly total precipitation, gridded at the $4k^2$ spatial resolution, was obtained from PRISM (PRISM Climate Group, 2014), and monthly average gauge height of the McKenzie River at the outlet of Clear Lake was extracted from USGS (USGS, 2021). Correlation coefficients are for the 1959-2021 period.

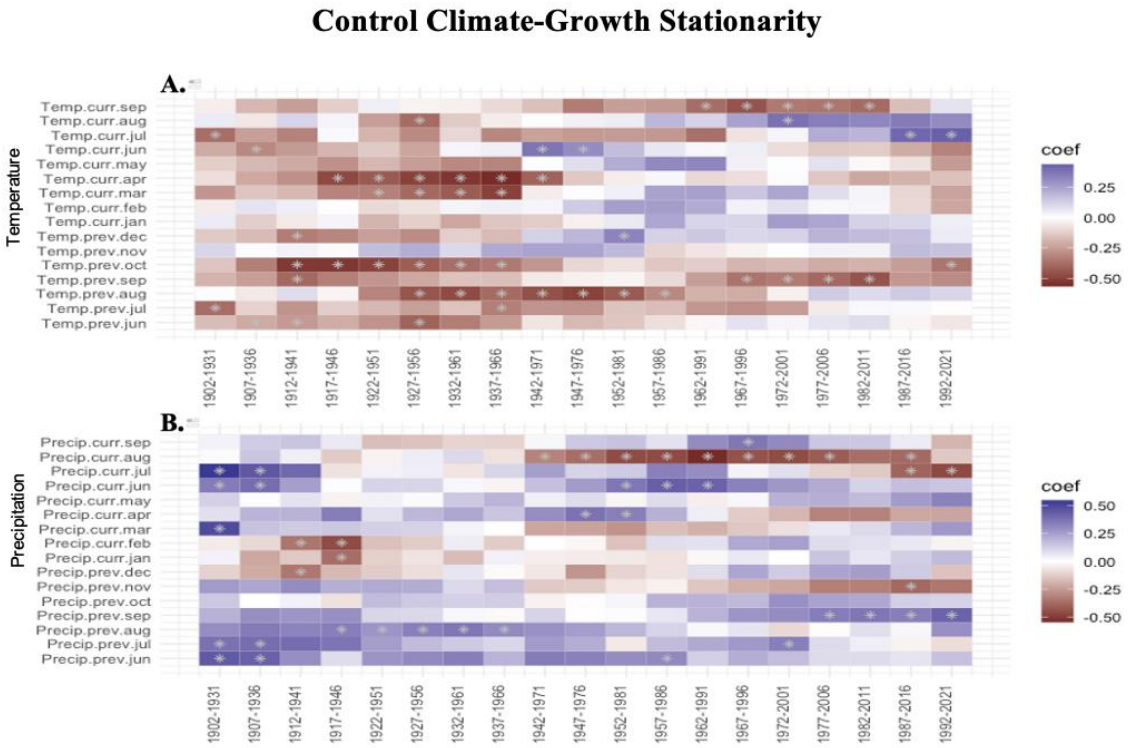

Figure A.19. Climate-growth relationships performed repeatedly for a consecutive 30-year time window with a 5-year overlap by pairing the total ring width control chronology with monthly mean air temperature (A) and monthly total precipitation (B). The x-axis displays the analysis period from 1895 to 2021. The y-axis presents calendar months, beginning in previous year September and ending in current growth year June. The colors displayed in the legend illustrate the direction of the relationship, with blue being a positive relationship and red signifying a negative relationship. Significant ($p < 0.05$) correlations are marked with an asterisk. Monthly climate parameters, gridded at the $4k^2$ spatial resolution, were obtained from PRISM (PRISM Climate Group, 2014).

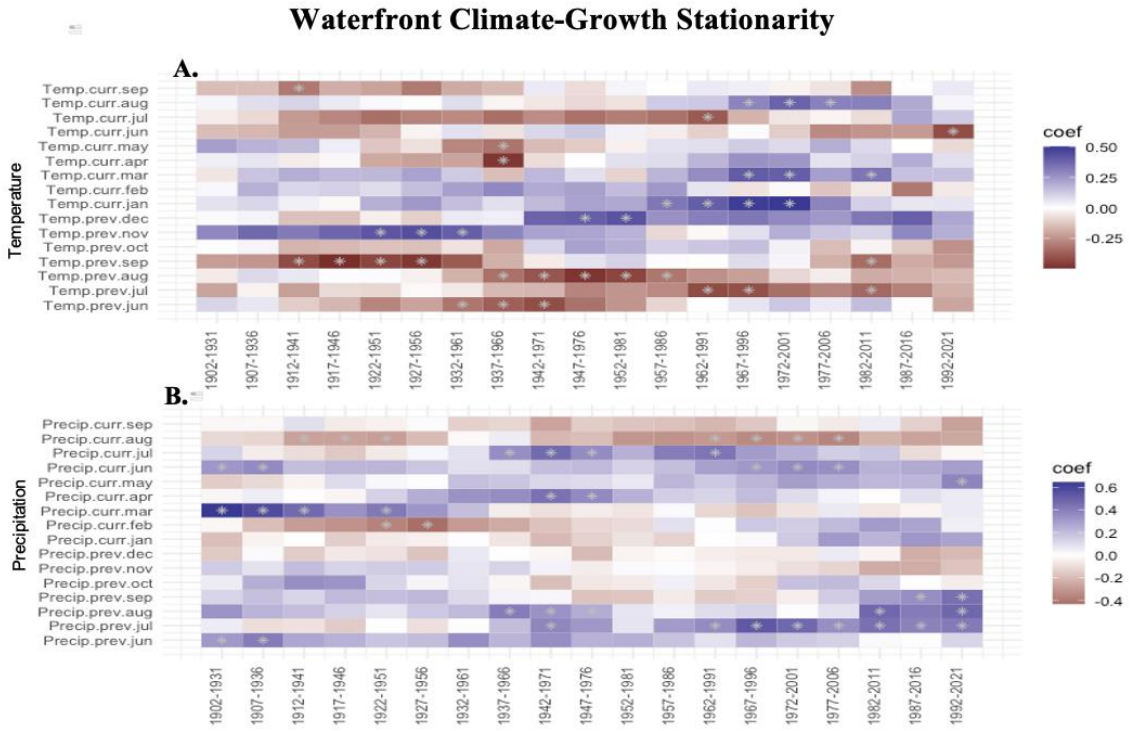

Figure A.20. Climate-growth relationships performed repeatedly for a consecutive 30-year time window with a 5-year overlap by pairing the total ring width waterfront chronology with monthly mean air temperature (A) and monthly total precipitation (B). The x-axis displays the analysis period from 1895 to 2021. The y-axis presents calendar months, beginning in previous year September and ending in current growth year June. The colors displayed in the legend illustrate the direction of the relationship, with blue being a positive relationship and red signifying a negative relationship. Significant ($p < 0.05$) correlations are marked with an asterisk. Monthly climate parameters, gridded at the $4k^2$ spatial resolution, were obtained from PRISM (PRISM Climate Group, 2014).

Table A.2. Summary of significant 2-month (bimonthly) and 6-month (seasonalized) climate-growth relationships with each of the six chronologies paired with monthly total precipitation, mean air temperature, and gage height. Monthly climate data, gridded at $4k^2$ spatial resolution, were obtained from PRISM (PRISM Climate Group, 2014) for a period of 1895-2021 and monthly average gauge height was extracted from USGS (USGS, 2021) for a period of 1959-2021. Significant positive relationships are displayed in the color blue and significant negative relationships are displayed in the color red.

Climate Variable	CLW				CLL			
Total Ring Width								
	2-month		**6-month**		**2-month**		**6-month**	
	Previous	**Current**	**Previous**	**Current**	**Previous**	**Current**	**Previous**	**Current**
Precip	Jul-Sep Mar-Apr	May-Jul Aug-Sep	Mar-Sep Feb-Apr	May-Aug	Jul-Sep	May-Jul	Mar-Nov Mar-Apr	May-Aug
Temp	Jul-Sep Nov-Jan	Jun-Jul	May-Oct Oct-Apr	--	Sep-Oct	--	May-Oct	--
Gage	--	--	--	--	--	--	--	--
Earlywood								
	2-month		**6-month**		**2-month**		**6-month**	
	Previous	**Current**	**Previous**	**Current**	**Previous**	**Current**	**Previous**	**Current**
Precip	Jul-Aug	May-Jul Aug-Sep	Mar-Oct Mar-Apr	Apr-Aug	Jul-Sep	May-Jun	Mar-Aug	--
Temp	Aug-Sep Oct-Feb	--	Mar-Oct Sep- Apr	Apr-May	Sep-Oct	--	Mar-Oct	--
Gage	--	--	--	--	--	--	--	--
Latewood								
	2-month		**6-month**		**2-month**		**6-month**	
	Previous	**Current**	**Previous**	**Current**	**Previous**	**Current**	**Previous**	**Current**
Precip	Jul-Sep Oct-Nov Feb-Apr	May-Jul Aug-Sep	Apr-Dec Oct-Apr	Apr-Aug	Jul-Nov	May-Jul	Apr-Dec	Apr-Sep
Temp	Aug-Oct	Jun-Jul	Mar-Oct	--	--	--	--	--
Gage	Feb-Mar	Apr-	Nov-Apr	May-	--	--	--	--

May Aug

Table A.3. Multiple regression summary statistic results from the first set of analyses (predicting tree-growth at the waterfront site) using the total ring width chronologies with the best model denoted with an asterisk.

# of Backward Lagged Years	R^2	Adj.R^2	AIC	BIC
4	0.2348	0.2235	-1017.3952	-990.4904
5 *	0.2491	0.2380	-1023.9105	-997.0057
6 *	0.2520	0.2409	-1025.2221	-998.3173
7	0.2468	0.2357	-1022.8743	-995.9695
8	0.2391	0.2278	-1019.3256	-992.4208
9	0.2439	0.2327	-1021.5231	-994.6183
10	0.2354	0.2241	-1017.6538	-990.7490
11	0.2329	0.2216	-1016.5491	-989.6443
12	0.2329	0.2216	-1016.5327	-989.6279
13	0.2329	0.2216	-1016.5613	-989.6565
14	0.2347	0.2234	-1017.3429	-990.4381
15	0.2332	0.2219	-1016.6994	-989.7946
16	0.2343	0.2230	-1017.1781	-990.2733
17	0.2341	0.2228	-1017.0753	-990.1705
18	0.2339	0.2226	-1017.0053	-990.1005
19	0.2348	0.2235	-1017.3952	-990.4904
20	0.2359	0.2247	-1017.9178	-991.0130
21	0.2328	0.2215	-1016.4959	-989.5911
22	0.2357	0.2245	-1017.8238	-990.9190
23	0.2339	0.2226	-1016.9746	-990.0698
24	0.2380	0.2268	-1018.8591	-991.9543
25	0.2329	0.2216	-1016.5384	-989.6336
26	0.2359	0.2246	-1017.8886	-990.9838
27	0.2430	0.2318	-1021.1008	-994.1960
28	0.2381	0.2269	-1018.8886	-991.9838
29	0.2326	0.2213	-1016.4257	-989.5209
30	0.2337	0.2224	-1016.8846	-989.9798
31	0.2326	0.2213	-1016.4428	-989.5209

32	0.2339	0.2226	-1016.9736	-990.0688
33	0.2328	0.2215	-1016.5164	-989.6116
34	0.2363	0.2251	-1018.0983	-991.1935
35	0.2330	0.2216	-1016.5667	-989.6619
36	0.2329	0.2216	-1016.5279	-989.6230
37	0.2383	0.2271	-1018.9781	-992.0733
38	0.2343	0.2231	-1017.1936	-990.2888
39	0.2327	0.2214	-1016.4429	-989.5381
40	0.2360	0.2248	-1017.9561	-991.0513

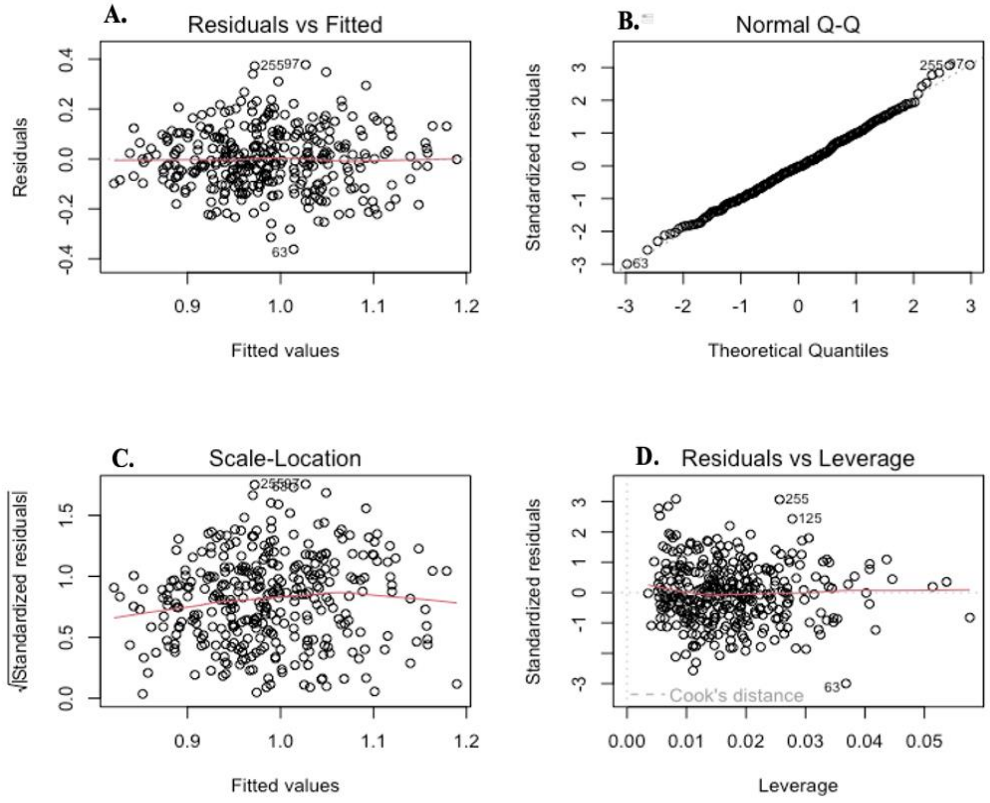

Figure A.21. Visual diagnostic check of residuals of reduced and final model of the first set of regression analyses for the total ring width model *t-5*. In the top left corner is a plot displaying non-linearity (A) with residuals on the y-axis and the fitted values (estimated responses) on the x-axis. In the top right is a Q-Q plot illustrating normality (B) with the standardized residuals plotted on the y-axis and theoretical quantiles on the x-axis. In the bottom left is a plot showing equal variance (C) with the square root of the absolute value of standardized residuals on the y-axis and the fitted values (estimated responses) on the x-axis. The bottom right corner displays a plot illustrating that there are no influential

outliers via a Cook's Distance test (D) with the standardized residual of each point on the y-axis and the leverage of each point on the x-axis.

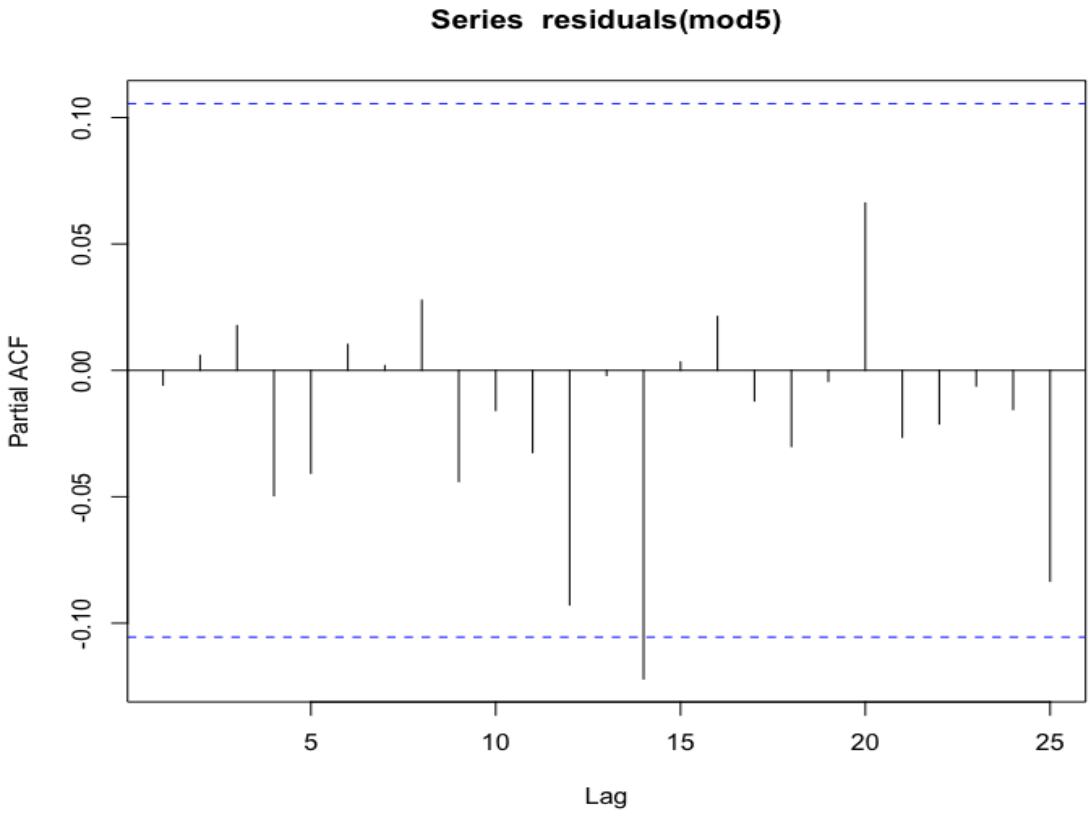

Figure A.22. Partial Autocorrelation Function (PACF) of the residuals from the top best model *t-5* from the first set of regression analyses using the total ring width chronologies to predict growth in the waterfront trees. The x-axis represents lagged values ranging from 0-25 and the y-axis displays correlation coefficient values. The direction of each line represents the direction of the relationship, with significant relationships extending beyond the dashed blue 95% confidence interval line. Although lag 14 displays a significant relationship, a Durbin-Watson test ruled out leftover significant autocorrelation in the model's residuals.

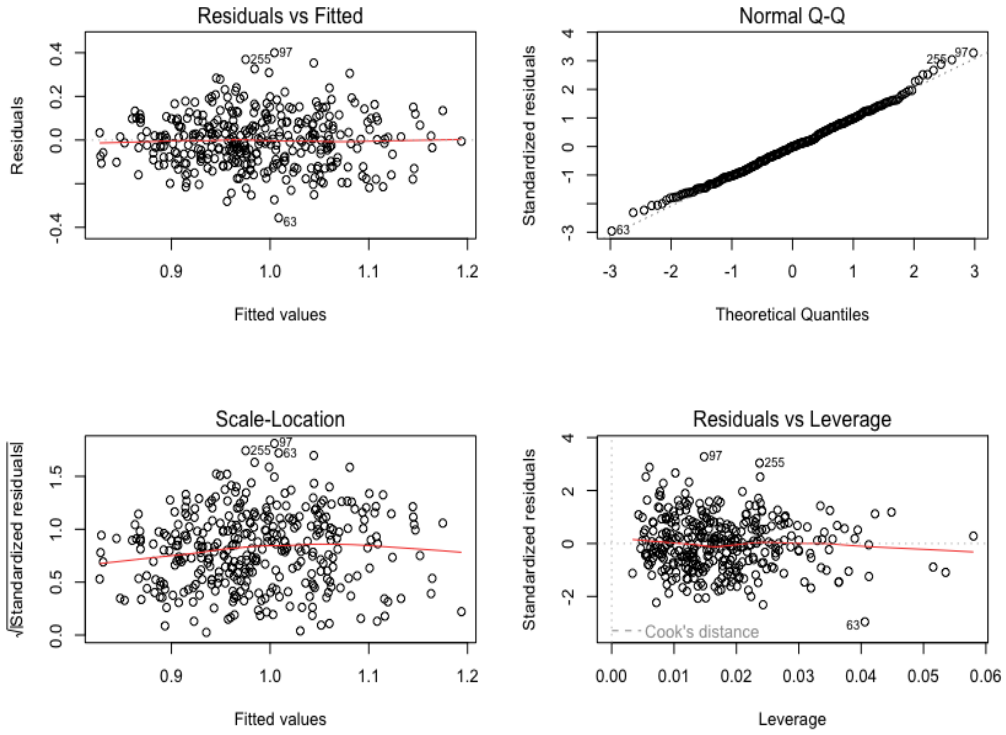

Figure A.23. Visual diagnostic check of residuals of reduced and final model of the first set of regression analyses for the total ring width model *t-6*. In the top left corner is a plot displaying non-linearity (A) with residuals on the y-axis and the fitted values (estimated responses) on the x-axis. In the top right is a Q-Q plot illustrating normality (B) with the standardized residuals plotted on the y-axis and theoretical quantiles on the x-axis. In the bottom left is a plot showing equal variance (C) with the square root of the absolute value of standardized residuals on the y-axis and the fitted values (estimated responses) on the x-axis. The bottom right corner displays a plot illustrating that there are no influential outliers via a Cook's Distance test (D) with the standardized residual of each point on the y-axis and the leverage of each point on the x-axis.

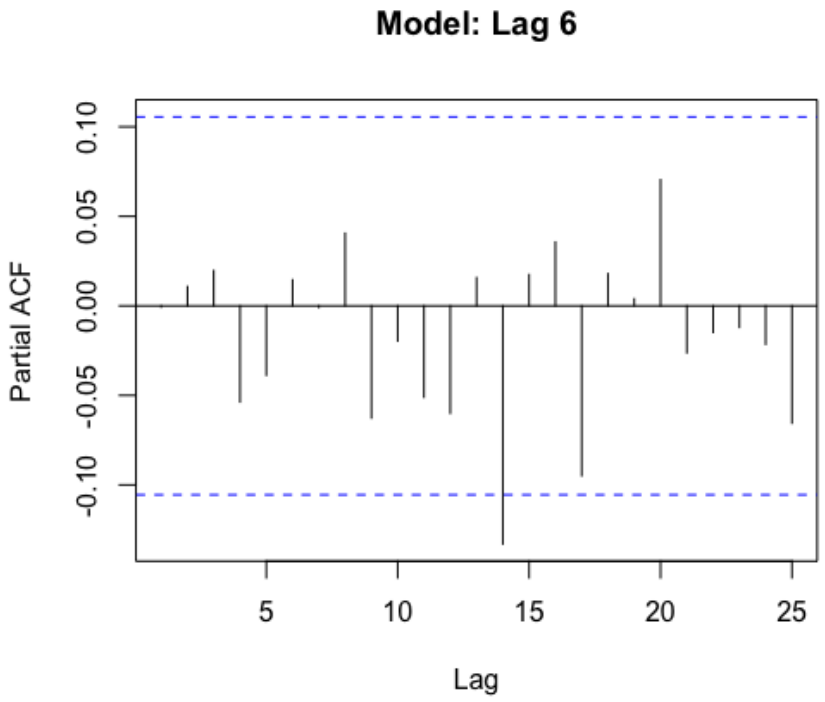

Figure A.24. Partial Autocorrelation Function (PACF) of the residuals from the top best model *t-6* from the first set of regression analyses using the total ring width chronologies to predict growth in the waterfront trees. The x-axis represents lagged values ranging from 0-25 and the y-axis displays correlation coefficient values. The direction of each line represents the direction of the relationship, with significant relationships extending beyond the dashed blue 95% confidence interval line. Although lag 14 displays a significant relationship, a Durbin-Watson test ruled out leftover significant autocorrelation in the model's residuals.

Table A.4. Multiple regression summary statistic results from the first set of analyses (predicting tree-growth at the waterfront site) using earlywood chronologies with the best model denoted with an asterisk.

# of Backward Lagged Years	R^2	Adj.R^2	AIC	BIC
4	0.2198	0.2106	-466.8651	-443.8038
5 *	0.2310	0.2220	-471.8762	-448.8150
6 *	0.2353	0.2263	-473.7895	-450.7282

7	0.2289	0.2198	-470.9176	-447.8563
8	0.2243	0.2152	-468.8876	-445.8264
9	0.2281	0.2190	-470.5614	-447.5002
10	0.2188	0.2096	-466.4540	-443.3927
11	0.2195	0.2080	-464.7458	-437.8410
12	0.2183	0.2091	-466.2089	-443.1476
13	0.2184	0.2092	-466.2494	-443.1881
14	0.2203	0.2111	-467.1125	-444.0512
15	0.2184	0.2092	-466.2523	-443.1911
16	0.2198	0.2106	-466.8651	-443.8038
17	0.2202	0.2110	-467.0661	-444.0049
18	0.2220	0.2129	-467.8727	-444.8114
19	0.2184	0.2092	-466.2541	-443.1928
20	0.2210	0.2118	-467.3995	-444.3382
21	0.2184	0.2092	-466.2440	-443.1827
22	0.2202	0.2087	-465.0522	-438.1474
23	0.2184	0.2092	-466.2823	-443.2210
24	0.2212	0.2120	-467.4965	-444.4352
25	0.2186	0.2094	-466.3598	-443.2985
26	0.2227	0.2136	-468.1830	-445.1218
27	0.2256	0.2165	-469.4729	-446.4116
28	0.2222	0.2131	-467.9523	-444.8910
29	0.2184	0.2092	-466.2632	-443.2020
30	0.2210	0.2118	-467.3994	-444.3381
31	0.2188	0.2096	-466.4279	-443.3667
32	0.2185	0.2093	-466.3226	-443.2613
33	0.2185	0.2093	-466.2908	-443.2295
34	0.2214	0.2123	-467.6031	-444.5418
35	0.2183	0.2091	-466.2079	-443.1467
36	0.2204	0.2112	-467.1427	-444.0815
37	0.2203	0.2112	-467.1145	-444.0532
38	0.2222	0.2130	-467.9247	-444.8635
39	0.2183	0.2091	-466.2067	-443.1455
40	0.2203	0.2112	-467.1260	-444.0647

Table A.5. Multiple regression summary statistic results from the first set of analyses (predicting tree-growth at the waterfront site) using the latewood chronologies with the best model denoted with an asterisk.

# of Backward Lagged Years	R^2	Adj.R^2	AIC	BIC
4	0.1458	0.1381	-779.7832	-760.7275
5	0.1404	0.1326	-777.6786	-758.6229
6	0.1483	0.1405	-780.7293	-761.6736
7	0.1387	0.1309	-777.0059	-757.9502
8	0.1446	0.1368	-779.3068	-760.2511
9	0.1383	0.1305	-776.8511	-757.7954
10	0.1373	0.1295	-776.4693	-757.4136
11	0.1409	0.1331	-777.8532	-758.7974
12	0.1375	0.1297	-776.5496	-757.4939
13	0.1422	0.1344	-778.3449	-759.2892
14	0.1433	0.1355	-778.8034	-759.7477
15 *	0.1570	0.1493	-784.1689	-765.1132
16	0.1458	0.1381	-779.7832	-760.7275
17	0.1383	0.1305	-776.8480	-757.7923
18	0.1375	0.1297	-776.5538	-757.4981
19	0.1379	0.1301	-776.6923	-757.6366
20	0.1373	0.1295	-776.4704	-757.4147
21	0.1412	0.1334	-777.9783	-758.9226
22	0.1403	0.1325	-777.6416	-758.5859
23	0.1443	0.1365	-779.1828	-760.1271
24	0.1374	0.1295	-776.4821	-757.4264
25	0.1379	0.1301	-776.6892	-757.6335
26	0.1397	0.1319	-777.3894	-758.3337
27	0.1403	0.1325	-777.6413	-758.5856
28	0.1374	0.1295	-776.4902	-757.4345
29	0.1390	0.1312	-777.1363	-758.0806
30	0.1374	0.1295	-776.4865	-757.4307
31	0.1467	0.1390	-780.1237	-761.0680
32	0.1401	0.1323	-777.5405	-758.4847
33	0.1375	0.1296	-776.5227	-757.4670
34	0.1385	0.1306	-776.9100	-757.8543
35	0.1374	0.1295	-776.4838	-757.4281
36	0.1421	0.1343	-778.3405	-759.2848

37	0.1411	0.1332	-777.9158	-758.8601
38	0.1435	0.1357	-778.8687	-759.8130
39	0.1410	0.1332	-777.8895	-758.8337
40	0.1470	0.1393	-780.2535	-761.1978

Table A.6. Multiple regression summary statistic results from the second set of analyses (predicting tree-growth at the waterfront site) using the total ring width chronologies with the best model denoted with an asterisk.

# of Backward Lagged Years	R^2	Adj.R^2	AIC	BIC
4	0.3968	0.3899	-506.5007	-483.2343
5	0.3897	0.3828	-502.3495	-479.0831
6	0.3839	0.3769	-498.9539	-475.6875
7	0.3834	0.3764	-498.6441	-475.3777
8	0.3845	0.3775	-499.2690	-476.0026
9	0.3833	0.3763	-498.5787	-475.3123
10	0.3827	0.3757	-498.2391	-474.9727
11	0.3837	0.3767	-498.8435	-475.5771
12	0.3893	0.3823	-502.0834	-478.8170
13	0.3849	0.3779	-499.5098	-476.2433
14	0.3826	0.3756	-498.2119	-474.9454
15	0.3847	0.3777	-499.4251	-476.1587
16	0.3829	0.3759	-498.3809	-475.1145
17	0.3971	0.3902	-506.6651	-483.3987
18	0.3943	0.3874	-505.0326	-481.7662
19 *	0.4030	0.3962	-510.1860	-486.9196
20	0.3915	0.3845	-503.3588	-480.0924
21	0.3859	0.3789	-500.1084	-476.8420
22	0.3827	0.3757	-498.2400	-474.9736
23	0.3830	0.3760	-498.4511	-475.1846
24	0.3827	0.3757	-498.2707	-475.0043
25	0.3831	0.3760	-498.4601	-475.1937
26	0.3846	0.3776	-499.3708	-476.1044

27	0.3835	0.3765	-498.7079	-475.4415
28	0.3834	0.3764	-498.6567	-475.3903
29	0.3835	0.3765	-498.7100	-475.4436
30	0.3848	0.3778	-499.4464	-476.1800
31	0.3905	0.3836	-502.7911	-479.5247
32	0.3851	0.3781	-499.6222	-476.3558
33	0.3851	0.3781	-499.6312	-476.3648
34	0.3828	0.3757	-498.2851	-475.0186
35	0.3830	0.3760	-498.4170	-475.1506
36	0.3836	0.3766	-498.7833	-475.5169
37	0.3832	0.3762	-498.5456	-475.2792
38	0.3832	0.3762	-498.5449	-475.2785
39	0.3881	0.3811	-501.3660	-478.0996
40	0.3838	0.3768	-498.8660	-475.5996

Table A.7. Multiple regression summary statistic results from the second set of analyses (predicting tree-growth at the waterfront site) using the earlywood chronologies with the best model denoted with an asterisk.

# of Backward Lagged Years	**R^2**	**Adj.R^2**	**AIC**	**BIC**
4	0.3934	0.3865	-502.9523	-479.6859
5	0.3876	0.3824	-501.5921	-482.2035
6	0.3838	0.3786	-499.3983	-480.0096
7	0.3842	0.3790	-499.6302	-480.2415
8	0.3841	0.3789	-499.5658	-480.1771
9	0.3837	0.3785	-499.3333	-479.9446
10	0.3837	0.3785	-499.3373	-479.9487
11	0.3899	0.3845	-481.7986	-462.5520
12	0.3884	0.3815	-500.0499	-476.7835
13	0.3852	0.3782	-498.1875	-474.9211
14	0.3845	0.3775	-497.7589	-474.4925
15	0.3845	0.3775	-497.7677	-474.5012
16	0.3844	0.3775	-497.7465	-474.4800
17 *	0.3965	0.3897	-504.8157	-481.5492
18 *	0.3942	0.3891	-505.4623	-486.0736

19	0.4010	0.3957	-488.1759	-468.9293
20	0.3899	0.3847	-502.9034	-483.5147
21	0.3837	0.3803	-501.3325	-485.8216
22	0.3884	0.3830	-480.9523	-461.7057
23	0.3838	0.3785	-499.3466	-479.9579
24	0.3843	0.3791	-499.6856	-480.2969
25	0.3839	0.3787	-499.4290	-480.0403
26	0.3859	0.3789	-498.5854	-475.3190
27	0.3843	0.3791	-499.6831	-480.2945
28	0.3837	0.3785	-499.3337	-479.9450
29	0.3884	0.3848	-482.9520	-467.5547
30	0.3866	0.3814	-500.9773	-481.5887
31	0.3859	0.3806	-500.5646	-481.1759
32	0.3906	0.3854	-503.3379	-483.9493
33	0.3881	0.3829	-501.8957	-482.5070
34	0.3848	0.3796	-499.9562	-480.5676
35	0.3844	0.3791	-499.6929	-480.3042
36	0.3842	0.3790	-499.6088	-480.2201
37	0.3843	0.3790	-499.6412	-480.2526
38	0.3864	0.3811	-500.8579	-481.4692
39	0.3864	0.3812	-500.8624	-481.4738
40	0.3850	0.3797	-500.0499	-480.6612

Table A.8. Multiple regression summary statistic results from the second set of analyses (predicting tree-growth at the waterfront site) using the latewood chronologies with the best model denoted with an asterisk.

# of Backward Lagged Years	**R^2**	**Adj.R^2**	**AIC**	**BIC**
4 *	0.2125	0.2056	-832.6756	-813.4290
5	0.2039	0.1969	-828.9010	-809.6544
6	0.1912	0.1842	-823.4244	-804.1778
7	0.1911	0.1841	-823.3830	-804.1364
8	0.1917	0.1846	-823.6167	-804.3701
9	0.1912	0.1841	-823.3920	-804.1454

10	0.1853	0.1781	-820.8699	-801.6233
11	0.1860	0.1789	-821.1759	-801.9293
12	0.2019	0.1950	-828.0437	-808.7970
13	0.1884	0.1813	-822.2052	-802.9586
14	0.1939	0.1868	-824.5603	-805.3136
15	0.1949	0.1878	-824.9903	-805.7437
16	0.1854	0.1783	-820.9375	-801.6909
17	0.1898	0.1827	-822.7909	-803.5442
18	0.1918	0.1847	-823.6439	-804.3973
19	0.2004	0.1934	-827.3860	-808.1394
20	0.1888	0.1817	-822.3898	-803.1432
21	0.1852	0.1805	-822.8419	-807.4446
22	0.1862	0.1791	-821.2602	-802.0136
23	0.1853	0.1782	-820.8794	-801.6328
24	0.1854	0.1782	-820.9076	-801.6610
25	0.1854	0.1783	-820.9160	-801.6694
26	0.1866	0.1795	-821.4489	-802.2023
27	0.1859	0.1787	-821.1193	-801.8727
28	0.1891	0.1820	-822.5053	-803.2586
29	0.1852	0.1781	-820.8534	-801.6068
30	0.1854	0.1783	-820.9243	-801.6777
31	0.1891	0.1820	-822.5132	-803.2666
32	0.1892	0.1821	-822.5389	-803.2923
33	0.1899	0.1828	-822.8448	-803.5981
34	0.1853	0.1781	-820.8642	-801.6175
35	0.1852	0.1781	-820.8436	-801.5969
36	0.1896	0.1825	-822.7259	-803.4793
37	0.1862	0.1791	-821.2548	-802.0082
38	0.1852	0.1781	-820.8421	-801.5955
39	0.1915	0.1844	-823.5364	-804.2898
40	0.1858	0.1787	-821.0964	-801.8498